Modeling Chemistry and Flow in Catalytic Fixed-Bed Reactors with Detailed Geometry

Vom Promotionsausschuss der
Technischen Universität Hamburg-Harburg
zur Erlangung des akademischen Grades
Doktor-Ingenieurin (Dr.-Ing.)

genehmigte Dissertation

von
Ying Dong

aus
Hangzhou, China

2018

1. Gutachter: Prof. Dr. rer. nat. Raimund Horn
2. Gutachter: Prof. Dr.-Ing. habil. Dr. h. c. Stefan Heinrich
Tag der mündlichen Prüfung: 4. Mai 2018

Abstract

Industrial catalytic fixed-bed reactors are made of steel, operate at high temperatures and pressures and contain hazardous chemicals. What happens inside remains hidden. Due to the limited information elucidated from the conventional measurement techniques aiming to resolve the gradients of species and temperature along the reactor (typically only in and out information are available), engineers have to rely on time consuming and costly trial and error method in reactor design and optimization as well as reactor model development. In order to design and develop reactors with higher accuracy, to trouble-shoot and optimize reactor in a cost-effective manner, a reliable, predictive and informative reactor model is desired. Three-dimensional computational fluid dynamics (CFD) models with detailedly resolved bed geometry are promising modeling approach for achieving this goal.

In this work, CFD models were developed and applied to simulate three catalytic fixed-bed reactors with different types of packing configuration and reactions. Based on the packing geometry, different approaches were taken to create the simulation domains. A unit cell containing 1/4 of a single Pt wire was drawn to simulate the catalytically assisted combustion of methane on a Pt gauze. The reconstruction of X-ray microtomographic scans was used as input to generate the modeling domain to simulate CO oxidation on a Pt coated α-Al_2O_3 foam monolith. Computer generated random packing by discrete element method (DEM) was applied to simulate and optimize a pilot-scale fixed-bed reactor for n-butane oxidation to maleic anhydride under industrial relevant operational conditions.

A spatially resolved profile measurement technique was applied in this work. This sampling technique provides high resolution concentration and temperature profiles inside the reactor, providing the possibility to critically validate the simulation results, and to calibrate parameters required in the model with high confidence.

This work demonstrates that detailed reactor modeling and profile measurements are useful tools for achieving in-depth understanding of the interactions between flow, heat and mass transfer and catalytic reactions in fixed-bed reactors. Furthermore, with the comprehensive knowledge gained from both methods, a knowledge-based reactor optimization approach can be put forward.

Kurzfassung

Industrielle, katalytische Festbettreaktoren werden unter hohen Reaktordrücken und -temperaturen betrieben und prozessieren zum Teil gefährliche Chemikalien. Typischerweise sind diese Reaktoren aus Stahl gefertigt, wodurch die Vorgänge in ihrem Inneren unsichtbar sind. Durch konventionelle Methoden zur Beprobung von Festbettreaktoren ist man bei der Beobachtung der Reaktionsvorgange auf wenige Messstellen entlang des Katalysatorbettes limitiert (typisch: Reaktoreingang und Reaktorausgang). Reaktormodelle werden anhand solcher Daten validiert, was begründet, dass Chemieingenieure bei der Reaktorauslegung und Reaktoroptimierung auf zeitintensive und teure Trial-and-Error-Methoden angewiesen sind. Um die Reaktorauslegung genauer und kosrengünstiger durchführen zu können, sind zuverlässige Reaktorsimulationen notwendig. Ein vielversprechender Ansatz zur Erreichung dieses Ziels ist die Verwendung von dreidimensionalen, computergestützten Fluiddynamik-Modellen (CFD-Modelle) gekoppelt mit geeigneten Reaktionskinetiken.

In der vorliegenden Arbeit wurden CFD-Modelle entwickelt und angewand um drei unterschiedliche Festbettreaktoren zu simulieren. Es wurden drei verschiedene Festbettgeometrien und drei Reaktionen untersucht. In Abhängigkeit von der Packungsgeometrie wurden unterschiedliche Ansätze zur Erzeugung der Reaktormodelle eingesetzt.

Für die Methanoxidation an einem Platinnetzkatalysator wurde eine Einheitszelle gewählt, die ein Viertel eines Platindrahtes enthält. Zur Simulation der Kohlenstoffmonoxid Oxidation an einem platinbeschichteten α-Al_2O_3-Schaummonolithen wurde der Monolith röntgenmikrotomographisch charackterisiert und die exakte Schaumgeometrie rekonstruiert. Für die Simulation und Optimierung eines Pilotreaktors für die katalytische Oxidation von n-Butan zu Maleinsäureanhydrid wurde eine Katalysatorpackung unter Zuhilfenahme der sogenannten Diskrete-Elemente-Methode (DEM), durch zufällige Schüttung der Katalysatorkörper, erzeugt.

Die Simulationen wurde in allen Fällen durch die Messung von örtlich aufgelösten Reaktorprofilen kritisch validiert. Die Untersuchungen fanden unter indutriell relevanten Bedingungen statt. Die experientellen Daten erlauben außerdem die Kalibrierung wichtiger Modellparameter mit sehr hoher Genauigkeit und Zuverlässigkeit. Die vorliegende Arbeit zeigt, dass die durchgeführten detailierten Simulationen in Kombination mit der experimentellen Messung von Reaktorkonzentrations und Reaktortemperaturprofilen, ein außerordentlich nützliches Werkzeug für ein tieferes Verständnis des Zusammenspiels von Fluiddynamik, Wärme- und Stofftransport und der katalytischen Reaktion in Festbettreaktoren darstellt. Das so erreichte tiefere Verständnis des Reaktionsprozesses, stellt einen Schritt in die Richtung einer wissensbasierten Reaktorauslegung bzw. -optimierung dar.

Acknowledgements

I would like to take this chance and express my gratitude to all the people who have helped me in my PhD period. I cannot image to arrive at this point without all your support.

I thank my advisor Prof. Dr. Raimund Horn for guiding me through the four years PhD adventure. Thank you for always having trust in me and encouraging me to be persistent. Every time I am confused with the theory, lost in details, your patience and instructive ideas helped me out. I would remember all the hours we spend deriving equations, trouble-shooting the pitfall in the simulations, polishing our manuscripts especially my 'missing article'. Thank you also for sharing many pieces of your life stories which provide me the right momentum when things gets difficult.

I thank Prof. Dr. Dr. h. c. Frerich Keil for recommending me for this PhD position and all the motivations and supports during years of study and research. Your everlasting enthusiasm for research and unselfishness in knowledge transfer is always a source of inspiration to me. Thank you for selecting book chapters and reviews for me so that I can get myself into the topic more efficiently. Also, thank you for proofreading my thesis and publications.

I thank Prof. Dr.-Ing. habil. Dr. h. c. Stefan Heinrich for referring my thesis. During my master study in TUHH, I had the pleasure to attend your lectures on particle technology. This knowledge is important to this work especially for the DEM simulation part.

I thank Prof. Dr.-Ing. Michael Schlüter for bringing me into the world of CFD. I learned a lot from your lectures on multiphase flow and CFD modeling. These two lectures provide me the foundation of my research.

Many thanks to Dr. Oliver Korup, the hero behind the stage without who many of the simulations I did would lose their meaning. Thank you for the inspiring suggestions in work, valuable advice in life and generous share of knowledge and experience.

I want to thank all the colleagues in the Institute of Chemical Reaction Engineering, TUHH: (best and only office mate) Viktor Berg, Stephan Bendt, Dr. Ludwig Scharfenberg, Andres Aquino, Bahne Sosna, Jan Pottbacker, Klaus Mandel, Christina Laarmann, Hermine Oppelaar, Dr. Achim Bartsch. It is a nice experience working with you all and lovely life memory for all the brilliant ideas during our 'coffee-break'. Especially, I would like to say thank you to Stephan Bendt for proofreading my PhD thesis and continuous encouragement during this four years of work.

A major part of my PhD project is in collaboration with BasCat in Berlin and I would like to thank all the people there who have contribute to this work. Special thank goes to Dr. Frank Rosowski for initiating the topics, sharing of valuable industrial expertise and all kinds of supports during our four years research collaborations. Many thanks to Dr. Michael Geske for numerous efforts in building up, testing the profile reactor, measuring and analysing profiles as well as the scientific input in our paper and presentations. I want to thank Dr. Benjamin Frank and Christian Schulz for the

kinetic model and interesting discussions.

It is my pleasure and luck to advisor the master works of Bahne Sosna, Nils Ellenfeld, Julian Gerdts who did excellent jobs and contributed major experimental input to this thesis. Also, Nina Heitz and Jannis Reich with whom I enriched my simulation experience.

Special thank goes to Dr. Heiner Schwarz who shared his experimental data on gauze reactor with me so that I can verify my simulation. I learned a lot from this simulation experience.

Thanks to all the friends, particularly to MiaoTian, simply for your company and caring nature.

Last but not least, I want to say thank you to my parents, and to my dear husband Jin for your understanding and support.

Contents

1 Introduction

The fixed-bed reactor is historically one of the oldest reactor configurations for performing fluid (gas or liquid) solid reactions in synthetic chemical and petroleum production industries [1]. As its name implies, a fixed-bed reactor is arranged so that the solid particles, which are mostly the catalyst, are held in position while the fluids flow around them [2]. Due to its fairly simple construction, stability, and controllability, this reactor type retains its favoured position in industrial practice over other more advanced and sophisticated reactors.

Substantial progress has been made in chemical engineering to understand the phenomenological and mechanistic aspects happening inside fixed-bed reactors [3–8]. Based on this knowledge, mathematical models of varying complexity have been derived and routinely practised with respect to reactor design, scale-up and process intensification [2, 9–11]. The performance of an industrial reactor for specific catalytic reactions is a complex function of the chemistry and transport processes [12]. Without a comprehensive knowledge of what happens inside the reactor, engineers have to rely on design by analogy, trial and error approach which is clearly not efficient. Therefore, numerical simulations preferably based on accessible parameters routing from physical properties are desired to, for example, find optimal operating parameters for reactors [13–15]. The main driving force for continuous modeling efforts in chemical engineering is not only to better design and control the reactor with improved model accuracy, but also to gain more fundamental and in-depth understanding of the interacting transport and reaction phenomena inside the fixed-bed reactor.

In order to simulate chemically reacting flows inside a fixed-bed reactor in detail, three-dimensional Computational Fluid Dynamics (CFD) models are developed in this work. The first step in a typical CFD simulation is to create the bed geometry. For a regular and periodic type of packing, one can draw the geometry with known geometrical parameters. Often, one draws only a representative unit-cell type of geometry due to the periodic nature of such a packing. One example of such a type of fixed-bed reactor is one packed with metal gauze catalysts. Reactions on catalytic gauzes are among the oldest processes in the chemical industry, for example, the Ostwald process and Andrussow process [16–18]. Because the catalytic reactions on the gauzes are so fast, those processes are often run under external transport limitations, and thus the reactor performance is dictated by mass and heat transport. Such a gauze reactor for catalytically assisted methane combustion over platinum is studied in this work and presented in Chapter 4.

When a packing structure does not have regular and repetitive geometry units, creating a calculation domain simply by drawing is not possible. For small beds, one can reconstruct the packing from non-invasive imaging method such as Magnetic Resonance Imaging (MRI) [19, 20] and X-ray computed microtomographic (μ-CT) scans [21, 22]. One good packing configuration for conducting μ-CT scans is the open-cell foam. It has randomized and reticulated pore structure which is difficult to draw

but can be well captured by the μ-CT [23]. Catalytically foams have been proposed as alternative porous catalyst carriers for strong exothermic/endothermic reactions [23]. In this work, CFD simulations based on reconstructed structure from μ-CT scans of CO oxidation on an open-cell foam monolith catalyst is explored and presented in Chapter 5.

Despite the vast research efforts in foam packing for heterogeneous catalysis, industrial application of this type of packing is rare [23]. Even nowadays, the most employed configuration of a fixed-bed reactor is still the well-known random packing of (catalyst) pellets. The dominating approach to model fixed-bed reactor with such random packing is the 'pseudo-homogeneous' and 'heterogeneous' models. In these models, the geometry of the packing is not resolved but regarded as an effective porous medium [24]. Since the particles are not resolved in those models, packing induced complex flow patterns cannot be described in detail. Furthermore, the model accuracy is questionable for fixed-bed reactors with small ratios of reactor diameter D to pellet diameter d (D/d ratio) due to pronounced confining wall effects [25]. This type of fixed-bed reactor is of particular interests to this work since many of the industrial important exothermic and endothermic reactions are conducted in this configurations [26, 27].

A recent advance in the field of modeling fixed-beds with random packing is the introduction of discrete-particle resolved three-dimensional CFD simulations by the pioneering work of Dixon et al. [28–32]. In this modeling approach, shapes and locations of each particle are modeled and the interstitial velocity field as well as other physical quantities are resolved. Thus, this approach reflects a more physical profound basis compared to the aforementioned conventional porous medium approach [33–38]. Many recent publications have also demonstrated encouraging results that this tool can indeed be applied to better understand the local phenomena [39], to develop correlations replacing experiments [38, 40], to design and control fixed-bed reactors [30], to study catalyst deactivation [41], to design catalyst shape [42, 43], as well as to find optimal operation conditions [44, 45] to various reactions especially for reforming reactions and exothermic oxidation of small hydrocarbons.

Even though it is rather a straightforward procedure to load pellets into a technical reactor in real life, creating such a random packing geometry in a simulation is by no means an easy task. To apply μ-CT on a technical-scale reactor is currently not feasible and is too costly to be routinely practised [46]. Hence, methods have been proposed to generate random packings by computer, among them are the Discrete Element Method (DEM) [26, 47–52] and the Monte Carlo method [36, 53–56]. Once a stable packing is generated by either method, one can extract the information of the location and orientation of each pellet and use as an input for CFD simulations. Obviously, due to the random nature, one obtains rather a numerical representation of the real packing than an exact copy. As a prerequisite, the computer generated random packing has to match the experimental packing in terms of bed density and porosity within statistical bounds [57]. In this work, the discrete element method is applied. It is widely applied in particle simulations with decent success [26, 58–61]. In order to gain confidence using computer generated random packing from DEM simulations especially for fixed-bed reactors with small D/d ratios, validation studies have been carried out and presented in Chapter 6.

The following step after generating a packing is meshing. An accurate, robust and cost-effective meshing strategy has been a popular research topic in this field for the past few years and is still to this day. Meshing techniques for the contact points (lines/areas) between the computer generated packings of both spherical and non-spherical particles have been advanced from the global shrinking or expansion

[62] to local modifications by bridging the particles with cylinders [49] or flattening the particle surface to make gaps [26]. The choice of a meshing strategy is often linked to the experience one has with a certain CFD program. Systematic analysis and guidance of the applied meshing strategy to the performance of flow, pressure drop, void fraction, heat transfer, and reaction simulations are reported by Dixon et al. [63] using ANSYS Fluent, Eppinger et al. [26] and Wehinger et al. [64] using STAR-CCM+, Boccardo et al. [65] using OpenFoam and Rebughini et al. [66] using catalyticFOAM [67]. In this work, the work flow proposed by Eppinger et al. [26] for STAR-CCM+ users is adopted. To validate the DEM-CFD approach coupled with the applied meshing strategy, heat transfer studies in a fixed-bed reactor with low D/d ratio ($4 \leq D/d \leq 7$) for both spherical and Raschig ring packings in moderate flow conditions and high temperature ranges were conducted. This study is demonstrated in Chapter 7.

To further improve the confidence of such simulations and achieve widespread use, even as primary design tool for chemical industrial practice [57], joint efforts from academia research and industry are needed [51]. N-butane oxidation to maleic anhydride (MA) was chosen in this work as the studied reaction. It is one of the most important industrial catalytic oxidation reactions with a high annual worldwide MA production (2.8 million metric tons in 2015) [68]. Currently, one of the dominant reactor configurations is the multi-tubular fixed-bed reactor cooled by circulating molten salt, packed with shaped pellets of vanadyl pyrophosphate (VPP) catalyst [69, 70]. Due to the explosion limitation, the butane inlet composition is typically below 2 % [71]. Since the unconverted n-butane is not recycled at the end of the bed, this process runs at high conversion levels typically at 80-85 % n-butane conversion [72]. The overall yield of MA reported is 57-65 % [72], which is unsatisfactory. The high production rate and growing demand of MA motivate chemists to find higher performance catalysts [73–75], engineers to improve operational conditions [76] or designing new reactor configurations [77, 78]. In view of the large scale of the process even small improvements (1 %) translate into significant revenue [72, 79]. CFD simulation and profile measurement of a pilot-scale profile reactor designed and developed for studying n-butane oxidation under industrial-relevant conditions have been carried out in this work. Since no lumped transport parameters are used in the CFD model, expensive experimentation input can be minimized by careful choice of representative experiments. Details of CFD modeling and measurements of a catalytic n-butane oxidation reactor are presented in Chapter 8.

Ideally and rigorously speaking, intra-particle diffusion limitations should be incorporated in the aforementioned CFD simulations for n-butane oxidation by solving mass balance (diffusion and reaction) inside each catalyst pellet [80]. However, the computational costs required to simulate a pilot-scale reactor including this aspect is too high to be realizable at the moment [81]. Hence, the trade-off has been made to simplify the reactor model while the main focus is paid to the effect of catalyst pore structure on n-butane oxidation to maleic anhydride in a fixed-bed reactor. Such numerical study is presented in Chapter 9.

This work is motivated by the scientific intuition for fundamental understanding of the fixed-bed reactor and, at the same time, is application driven. The aim of this work is to develop reliable, accurate and affordable models to perform simulations which facilitate in-depth understanding of the interactions between flow, heat and mass transport as well as chemistry. Furthermore, those simulations should be developed into a better tool to help interpret experimental data, to assist reactor design and, to predict safe operation conditions and, most importantly, to put forward model-based or knowledge-based optimization of the underlying processes in fixed-bed reactors.

This work does not only emphasize on model development, but also highlights the importance of reliable experimental validation. Conventional reactors with a few side sampling ports cannot achieve similar level of data density as the simulation delivers and, as a result, no critical comparison can be made. On the other hand, one cannot avoid the iterative process in the model improvement by comparing experimental data for fine tuning some model parameters. Consequently, the quantity and quality of the input experimental data can directly influence the model accuracy [57]. The spatially resolved profile reactor offers a solution to this problem as it can realize high resolution sampling of gas phase composition, gas temperature as well as solid temperature by means of the center sampling capillary [82–85]. Hence, these profiling techniques have been applied and presented thoroughly in the thesis together with the modeling efforts. High resolution spatial measurements of species and temperature profiles inside the reactor combined with particle resolved CFD modeling of chemistry and flow is a promising approach to understand the physical and chemical processes inside a catalytic fixed-bed reactor and provide a methodology for knowledge based optimization of important industrial processes.

Summary of Results and Future Perspective

2

As soon as a new approach like spatially resolved CFD modeling of catalytic fixed-bed reactors, rapidly and enthusiastically progress, the same level of doubts and criticism arise [1, 57]. Is it reliable? What are the benefits and, naturally, what are the limitations? This work tries to answer these questions and to put forward this approach to be a preferred design tool in industry. Three fixed-bed packing configurations: a single catalytic gauze, a foam monolith coated with catalytic material as well as random packing of catalyst pellets have been modeled in detail in this work. To demonstrate the validity and benefits of the applied numerical approach, high resolution profile measurements have been carried out. Critical judgement of the model performance has been made by comparing the simulated species and temperature profiles to the measured ones.

Catalytically assisted methane combustion over a single platinum gauze in a fixed-bed reactor is studied in this work. Three dimensional numerical reactor simulations including flow, mass transport, heat transport and microkinetic models for both surface and gas phase chemistry were carried out. Due to symmetry, only 1/4 of the gauze surface was considered in the calculation domain. Simulated species profiles show good agreement with the measurements previously carried out by Dr. Heiner Schwarz [86] in which work the steep spatial gradients in the vicinity of the gauze are resolved at submillimeter scale. Furthermore, this reactor combines a capillary sampling technique with a novel fiber-optic Laser-Induced Fluorescence (LIF) Spectroscopy method for detection and quantification of gas phase OH· radicals serving as indicator species for gas phase reactions. Full methane conversion was observed experimentally. The contribution of gas phase reactions to the methane conversion was analyzed by comparing simulation results with and without taking gas phase reactions into calculation to the measured ones. Results show that surface reactions alone account for about two-thirds of the experimental CH_4 conversion. This study provides insight into the interaction of chemistry and transport processes upstream, at and downstream of the catalytic gauze. The gradients upstream of the gauze are caused by diffusion while the gradients downstream of the gauze are a combined effect of diffusion and gas phase chemistry. Furthermore, this study highlights the interaction of surface and gas phase reactions by exchange of heat and radicals released from the catalyst surface.

Pore-scale resolved three dimensional CFD simulations based on reconstructed structure from μ-CT scans of an open-cell foam monolith catalyst have been carried out in this work. CO oxidation on a Pt coated α-Al_2O_3 foam monolith is chosen due to the well-know reaction kinetics [87]. CFD model takes into consideration laminar flow, chemistry by means of microkinetics, conjugated heat transfer as well as surface radiation. Meanwhile, high resolution profiles of gas species concentration and solid temperature in the center line of the reactor were measured by means of capillary sampling techniques together with a light-collecting optical pyrometer fibre (master

thesis of Julian Gerdts [88]). To compute the surface reaction rates, a parameter of A_{cat}/A_{geo} has to be introduced to account for the Pt coating. This parameter were screened in the simulations and best fit to the measurement is found with a value of 0.03. Furthermore, the measured solid temperature profile can only be approximated by the simulation with enforced heat loss through the reactor wall together with radiation heat loss on the foam surfaces. Based on those results, the adiabatic conditions were not achieved in the measurement. This study demonstrates that the μ-CT based CFD modeling is a promising modeling approach to reveal how complex the interplay between flow, heat generation and heat transport is and how subtle differences in geometry and flow velocity lead to pronounced non-uniformity in reaction rate and catalyst temperature. Also, this work illustrates a critical comparison between CFD simulation results and sub-millimeter resolved species and temperature profiles can help to identify model deficiencies and experimental artifacts.

The biggest part of this work focuses on the application and validation of the particle resolved CFD modeling of fixed-bed reactors at small D/d ratios packed with computer generated random packing by DEM simulations. DEM generated random packings have been validated by comparing simulated radial porosity profiles to experimental data and correlations from literature for spherical packings and in-house measurements (master thesis of Nils Ellenfeld [89]) for Raschig ring packings. High porosity values are found in the vicinity of the container wall for both packings due to the wall ordering effects and the stochastic nature of random packings. This method is found to be physically sound and reliable for reproducing the experimental packings within stochastic bounds.

After validating the DEM generated random packings, heat transfer studies in a fixed-bed reactor with low D/d ratio ($4 \leq D/d \leq 7$) for both spherical and Raschig ring packings in moderate flow conditions and high temperature ranges were conducted. An improved experimental technique for providing continuous high resolution radial temperature profiles has been proposed (master thesis of Bahne Sosna [90]) compared to conventional measurement methods (few discrete data points) in the literature. DEM-CFD approach has been validated to predict accurately radial temperature profiles for both packing types at different packing heights and different flow rates. The DEM-CFD approach has been found to work particularly well in cases when the packing can be accurately modeled while systematic errors result if the packing is not accurately simulated. Both simulation and experiment reveal high local inhomogeneity of fixed-bed reactors with small D/d ratio especially for ring type packings which are often used industrially. These packing induced local phenomena cannot be captured by rotationally symmetric pseudo-homogeneous models employing effective transport parameters and as a result, three-dimensional CFD simulations are more accurate.

Simulations and measurements of concentration and temperature profiles for n-butane oxidation to maleic anhydride were carried out under industrially relevant temperature-, flow- and pressure conditions in a pilot-scale fixed-bed reactor equipped with five heating zones. The results demonstrate that particle resolved CFD modeling of chemistry and flow is a promising approach for knowledge-based optimization of important catalytic process in industry. Simulations and measurements of concentration and temperature profiles for n-butane oxidation to maleic anhydride under industrially relevant temperature-, flow- and pressure conditions in a pilot-scale fixed-bed reactor, equipped with five heating zones, were carried out. Catalytic chemistry was included by a kinetic model of intrinsic reaction rates determined in separate measurements on crushed and sieved catalyst. Transport resistances and packing deviations were lumped in reaction rate multipliers determined by fitting the model to profiles meas-

ured at a uniform reactor wall temperature of 370 °C.

Simulated temperature-, flow velocity- and butane concentration fields reveal strong inhomogeneities inside the catalyst bed. A hot-spot develops at 370 °C wall temperature. Inside this hot-spot temperature differences of 40 K and more exist on one and the same pellet with negative impact on maleic anhydride selectivity and catalyst lifetime. An optimized wall temperature profile was derived by combining knowledge from the experimental profiles at uniform wall temperature and the particle resolved CFD results. A gradual increasing temperature with the heating zones set to $T_{wall,1} = 360$ °C, $T_{wall,2} = 365$ °C, $T_{wall,3} = 370$ °C, $T_{wall,4} = 375$ °C and $T_{wall,5} = 380$ °C was predicted by the model to eliminate the hot-spot and increase integral maleic anhydride selectivity at constant n-butane conversion. This prediction was confirmed by experiment. At 80 % n-butane conversion the maleic anhydride selectivity could be improved from 72 % to almost 75 %. Facing the scale of the process, this improvement translates into significant n-butane savings, reduced CO_x emissions and increased revenue.

Another attempt to improve n-butane oxidation to maleic anhydride is to take a look at the effect of catalyst pore structure on the reactor performance by numerical simulations. Coupling diffusion and reaction inside each catalyst pellet to the CFD simulation of technical scale reactor is computationally expensive. Hence, a fixed-bed reactor was simulated with a two-dimensional heterogeneous model taking into consideration the radial bed porosity variation. Since vanadyl pyrophosphate catalysts applied for this process in industrial fixed-bed reactors are bulk catalysts made by pressing the active powder into a pellet [91], the micro- and macro pore model of Wakao and Smith [92] was applied to model the diffusion-reaction inside the catalyst pellet. Simulation results have demonstrated that the reactor performance is sensitive to the chosen pore structure parameters especially the macro-pore porosity and mean micro-pore diameter. A bi-modal catalyst pellet with bigger macro-pores and smaller micro-pores is favored to achieve higher yields of maleic anhydride. This simulation highlights the potential of improving this process by pore structure optimization.

At the time of this writing, several future aspects can be recommended by the author taking n-butane oxidation as an example. Firstly, one can further explore and screen the space for reactor operation parameters based on the provided CFD models. A potential project is to study systematically the orientation and shape of the catalyst pellets to the reactor performance. One may improve the product yield by rational structuring of the packing. Another idea is to investigate stage-wise dosing of reactants. This can be easily probed in simulations and maybe realizable experimentally with the side sampling ports in the profile reactor used in this work. In the long run, it would be a good idea to 'map' the local flow, temperature and concentration field around each catalyst pellet to the chemistry nature of the catalyst to further investigate the local selectivity. For this purpose, coupling spatially-resolved catalyst characterization (e.g. Raman) to the profile reactor would be desired.

With continuous efforts in model improvement, numerical algorithm development together with the advance in computational resources [32, 93, 94], it can be anticipated that this modeling approach will become routine for both academy and industry in the near future. Furthermore, by combining this method with molecular modeling and *ab initio* calculations, the arrival at the frontier of *a priori* design of reactors [7] will no longer be a fantasy.

"We must remember that the most elegant and high-powered mathematical analysis based on a model which does not match reality is worthless for the engineer who must make design predictions."

Octave Levenspiel [4]

3 Theoretical Background and Methodology

Nowadays, reactor simulation plays a key role in scale-up and process optimizations as it offers a more cost-effective approach compared to experimentation [57]. This chapter presents the fundamentals and state-of-the-art simulation methods of the applied models within the scope of this thesis.

Modeling a fixed-bed reactor is indeed a multi-scale task: from the molecular scale of the intrinsic kinetics to particle scale of diffusion-reaction inside the pore structures and finally to the reactor scale with fluid flow, heat and mass transport [7, 9, 95]. Depending on the purpose of the simulation and the system of interest, engineers have to make wise decision on which level of details the model should cover.

From the reactor model scale standpoint, the simplest and still widely used or even favoured model is the plug-flow model in which an radially uniform and constant velocity field is assumed. For modeling wall-cooled or wall-heated reactors, an artificial wall heat transfer coefficient has been introduced into this conventional approach to describe the experimental observed temperature 'jump' in the near-wall region [96]. The driving force for continuous efforts to extend the basic plug-flow model with more detailed hydrodynamic effects is the accuracy needed for temperature field predictions, especially in the radial directions [97]. This model is generally agreed to be insufficient for reactors with small D/d ratios especially for exothermic and endothermic reactions. However, a huge library of semi-empirical correlations and practical know-how made this type of model preferred design tool in industry. Often, up to 20 % error estimation is added to the model predictions [96, 98].

More advanced models are the 'pseudo-' family models which take the radial bed porosity variations into consideration and employ improved correlations for heat and mass transfer [99, 100]. The accuracy of the predictions and model performance of this model type rely on the chosen effective transport parameters for describing dispersion [101, 102] and heat transfer which are usually presented in form of empirical correlations [24, 103–106]. Those empirical correlations are often derived for certain packing shapes, D/d ratios and operational conditions and thus are limited in applicability [107]. Especially for fixed-beds with small D/d ratio (below 10), the non-uniformities of the packing structure and wall effect challenge the circumferential symmetrical averaged properties used in 'pseudo-homogeneous' and 'heterogeneous' models [54, 108] which are historically developed for beds with high D/d ratios. Those local effects call for the need of continuous model refinement [109, 110] or more advanced modeling approach. To further develop this modeling approach, more systematic experiments with respect to a diversity of packings and wide range of operational conditions are necessary [111]. Even more efforts should be paid to analyse the transport models under reaction conditions [24, 112].

The alternative way to overcome the uncertainty in the effective parameters is to resolve the bed structure in detail and compute the three-dimensional interstitial ve-

locity field inside a fixed-bed reactor by solving the Navier-Stokes equations. Hence, particle-resolved three-dimensional computational fluid dynamics (CFD) simulations have been extensively developed for the past twenty years [28]. Many efforts have been made to put forward the application of this approach as discussed in Chapter 1 [50, 113]. The computer generated random packing of spherical and non-spherical particles is realized either by Discrete Element Methods (DEM) [26, 49, 51] or Monte-Carlo methods [114]. Meshing strategies are intensively researched, especially the contact point treatment for preventing cell skewness and enhancing convergence. Dixon et al. [63] have systematically evaluated the different contact point treatments: global shrink, overlapping, local flattening (cap) and bridging with respect to the void fraction, pressure drop and heat transfer. Rebughini et al. [66] further investigated the bridging approach and proposed a meshing protocol for properly describing the surface reactivity in fixed-bed reactors packed randomly with spheres. Simulations are extended from detailed flow [26] and heat transport [29, 115, 116] to include surface reactions described by microkinetics [117–119] as well as diffusion and reactions inside the catalyst particles [39, 120, 121]. Many works have proven the spatially resolved CFD simulation a great tool for chemical engineers to better understand the local phenomena, design and develop fixed-bed reactors especially for the ones with small D/d ratios [30]. Figure 3.1 illustrates the hierarchy of the aforementioned models in terms of the model complexity with respect to the computational efforts required. Clearly, the more sophisticated the model is, the more computational effort it needs [123]. Based on the experience of the author with commercial codes, a plug-flow model with macrokinetics converges within a few minutes while the two-dimensional heterogeneous model takes a couple of hours to converge. For these two types of models, a normal office computer would be sufficient. For the CFD approach, a computer cluster is generally required. The computational time can span between days to months depending on the number of mesh and kinetic model as well as the number of CPUs.

3.1 Heterogeneous model

The main difference between the pseudo-homogeneous and heterogeneous model is that the heterogeneous model considers explicitly the presence of the catalyst phase. Therefore, two sets of conservation equations are applied for the interstitial fluid and the catalyst phase, respectively [124]. Concentration and temperature profiles inside the catalyst pellets are coupled to the bulk fluid phase via the boundary conditions applied on the pellet surface. Therefore, the heterogeneous model can be a useful tool for studying the catalyst scale parameters with respect to the reactor performance. A schematic drawing of the model is shown in Figure 3.2. The details of this model are explained in the following sections, examples of the model performance are shown in Chapter 9.

3.1.1 Particle model

To solve the reaction-diffusion equation inside the catalyst pellet, two models are available. The simpler one is the ‘pseudo-continuum model’ in which the catalyst pellet is treated as a continuum described by global parameters: the void fraction ε and the tortuosity τ. The effective diffusivity is used to describe the transport within the pores [2]. This model is not very realistic for studies aiming to improve the pore structures of the catalyst. For a more detailed modeling, pore structure models and diffusion models are needed. Often used pore structure models in literature are the micro- and macro pore model of Wakao and Smith [92], the random pore model of

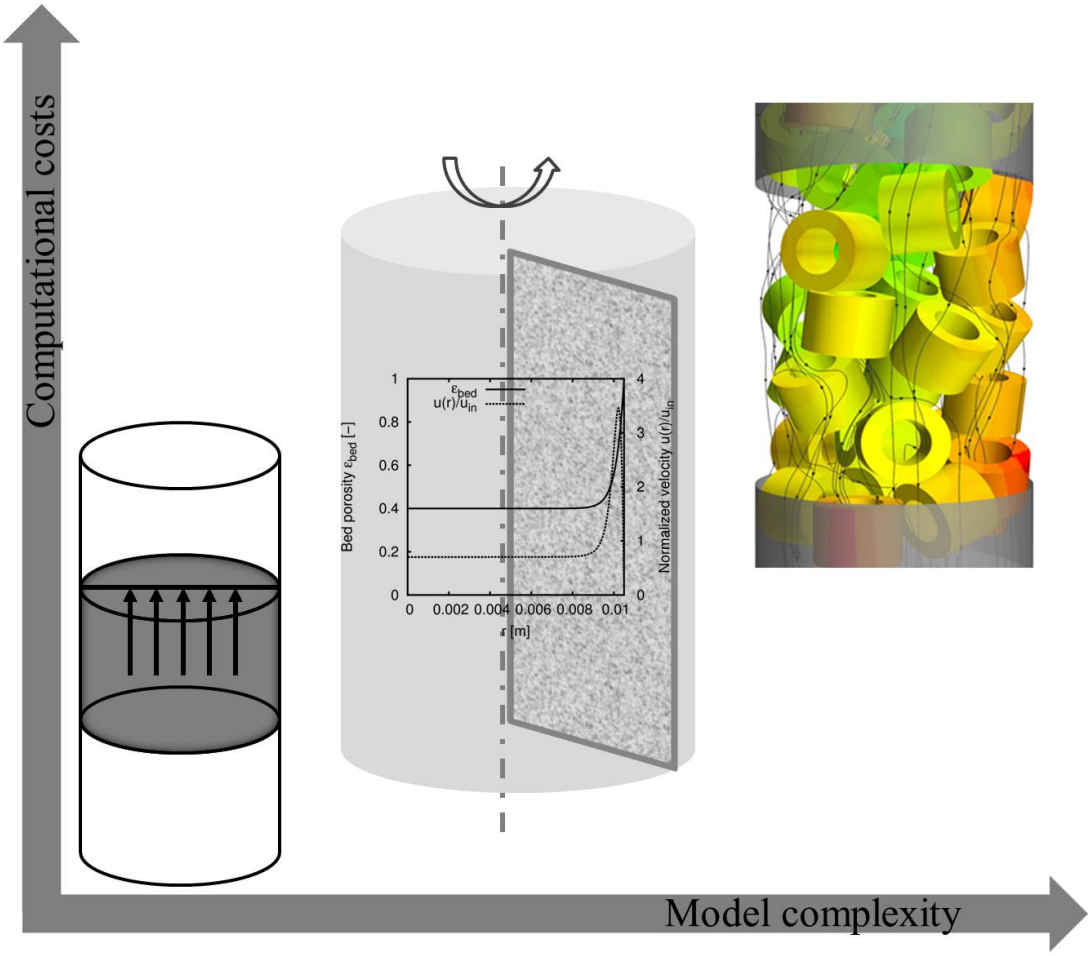

Figure 3.1: Illustration of the model complexity with respect to computational efforts for three types of fixed-bed models. From left to right: plug-flow model, 2-D axis-symmetric pseudo-homogeneous model with radial porosity profiles, 3-D particle-resolved CFD model [122].

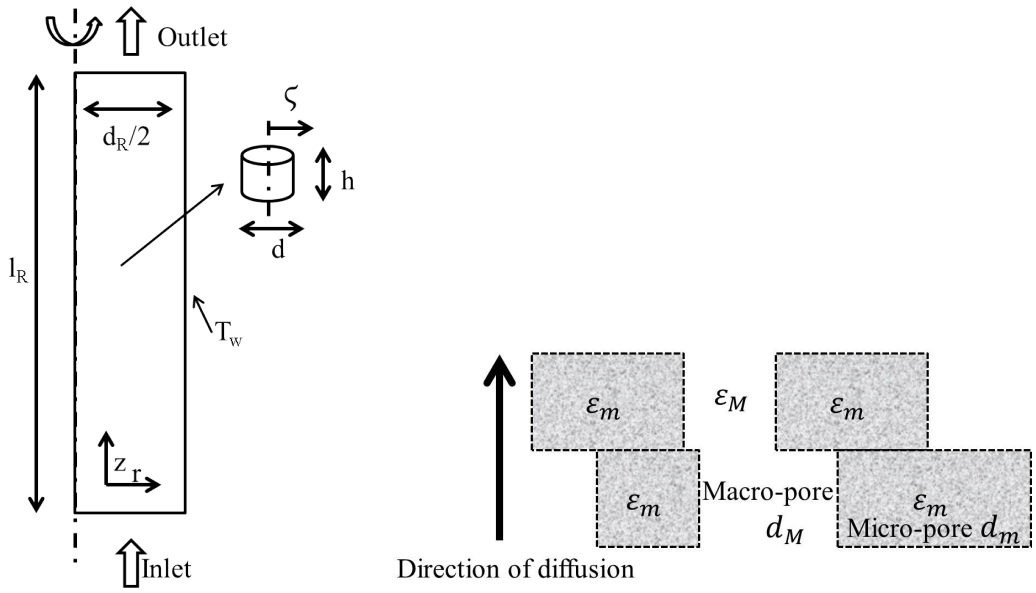

Figure 3.2: Schematic illustration of a two-dimensional heterogeneous model (left), micro- and macro pore model of Wakao and Smith (right) [92].

Johnson and Stewart [125], and the grain model of Szekeley and Evans [126]. More recently, a more detailed and realistic three-dimensional pore network model has been proposed by Rieckmann and Keil [127]. The diffusion fluxes are usually modeled using the dusty gas model, Maxwell-Stefan model, Wilke or Wilke-Bosanquet models [128]. One may refer to the works of Solsvik and Jakobsen [129] for a detailed summary of different diffusion models. For catalyst pellets containing a bi-modal pore size distribution, the micro- and macro pore model of Wakao and Smith [92] with the Wilke fomular can be a good option for practical reaction engineering calculations [130].

VPP catalyst pellets for n-butane oxidation to maleic anhydride typically have a bimodal pore structure, i.e. the micro-porous structure from the chemical synthesis of the active powder and the macro-porous region between the powders formed by the pelleting process. Therefore, the micro- and macro pore model of Wakao and Smith [92, 131] was applied for modeling VPP catalyst pellets in this work (Chapter 9). In this model the pore structure of the catalyst pellets is described by four parameters: mean macro-pore diameter d_M, mean micro-pore diameter d_m, macro-pore porosity ε_M, and micro-pore porosity ε_m as illustrated in Figure 3.2. The specific surface area (surface per catalyst weight) S_g and pellet density ρ_{pellet} are directly related to the pore structure and can be evaluated as follows [130]:

$$S_g = \frac{4V_M}{d_M} + \frac{4V_m}{d_m} \tag{3.1}$$

$$\rho_{pellet} = \rho_{solid}(1 - \varepsilon_{total}), \quad \varepsilon_{total} = \varepsilon_M + \varepsilon_m \tag{3.2}$$

Combining Eq. 3.1 and 3.2, one obtains:

$$S_g = \frac{4}{\rho_{pellet}}(\frac{\varepsilon_M}{d_M} + \frac{\varepsilon_m}{d_m}) \tag{3.3}$$

Both Knudsen diffusion and molecular diffusion are considered in this model [92, 131]

and the effective diffusivity of each species is expressed as:

$$D_{eff} = D_M \cdot \varepsilon_M^2 + \frac{\varepsilon_m^2 \cdot (1 + 3\varepsilon_M)}{1 - \varepsilon_M} D_m \tag{3.4}$$

$$\frac{1}{D_M} = \frac{1}{D_{AB}} + \frac{1}{D_{K,M}} \tag{3.5}$$

$$\frac{1}{D_m} = \frac{1}{D_{AB}} + \frac{1}{D_{K,m}} \tag{3.6}$$

where M and m stands for the macro-pore and micro-pore, respectively. The Knudsen diffusivity is calculated by:

$$D_{K,i} = \frac{d_{M,m}}{3} \sqrt{\frac{8RT}{\pi M_i}} \tag{3.7}$$

The molecular diffusivity is simplified to the binary diffusivity of each component in nitrogen since air is used as an oxidizer. It is calculated by the Fuller equation as follows [99]:

$$\frac{D_{AB}}{cm^2/s} = \frac{0.00143 \left(\frac{T}{K}\right)^{1.75} \left[\left(\frac{M_1}{g/mol}\right)^{-1} + \left(\frac{M_2}{g/mol}\right)^{-1}\right]^{0.5}}{\frac{p}{bar}\sqrt{2}\left[\left(\sum \delta v_1\right)^{1/3} + \left(\sum \delta v_2\right)^{1/3}\right]^2} \tag{3.8}$$

where δv is the so-called diffusion volume listed in Table 3.1.

Table 3.1: Diffusion volumes for the Fuller equation used in this work [99].

Molecule	$(\sum \delta v)$
C_4H_{10}	86.7
$C_4H_2O_3$	86.55
O_2	16.3
CO_2	26.7
CO	18.0
H_2O	13.1
N_2	18.5
$C_3H_4O_2$	69.16
$C_2H_4O_2$	53.26
Air	19.7

For the pore structure study presented in Chapter 9, the VPP catalyst pellet is assumed to be a full cylinder and the corresponding conservation equations are:
Mass balance:

$$\frac{4}{d^2} D_{eff,i} \left[\frac{\partial^2 c_i}{\partial \zeta^2} + \frac{1}{\zeta}\frac{\partial c_i}{\partial \zeta}\right] = \rho_{pellet} S_g \sum_{j=1}^{3} \nu_{ij} r_{j,s}, \tag{3.9}$$

Heat balance:

$$\frac{4}{d^2} \lambda_{pellet} \left[\frac{\partial^2 T}{\partial \zeta^2} + \frac{1}{\zeta}\frac{\partial T}{\partial \zeta}\right] = \rho_{pellet} S_g \sum_{j=1}^{3} -\Delta H_j r_{j,s}, \tag{3.10}$$

where $D_{eff,i}$ is the effective diffusivity of each species, λ_{pellet} is the effective thermal conductivity of the pellet and ζ is the dimensionless radial cylindrical coordinate of the pellet. In this study, the conservation equations were only solved along the radial coordinate of the pellet, i.e. concentration and temperature gradient along the height of the pellet were neglected. This is because in the heterogeneous model, the detailed particle geometry is not resolved in the calculation domain and thus only one effective coordinate can be taken for solving pellet equations. Furthermore, the concentration and temperature gradient between the outer surface of the pellet and the bulk gas were neglected. Solsvik and Jakobsen have found in their studies [129, 132] that the viscous flow and pressure drop inside the pellet are very small and can be neglected. Hence, no convective term and no momentum balance are applied in the pellet equations. Eq. 3.9 and Eq. 3.10 can be solved using the following boundary conditions:

$$\zeta = 0: \quad \frac{\partial c_i}{\partial \zeta} = 0, \quad \frac{\partial T}{\partial \zeta} = 0 \tag{3.11}$$

$$\zeta = 1: \quad c_i = c_{i,bulk}, \quad T = T_{bulk} \tag{3.12}$$

3.1.2 Reactor model

A two dimensional axis-symmetric reactor model including mass and heat transfer, as well as momentum balance taking into consideration of radial porosity profile of the bed packing, is perhaps the most sophisticated model in the 'pseudo-' model family [2]. The most advanced improvement in this approach is to model the flow with the extended Brinkman equation [133] including radial porosity profiles and effective viscosity [134]. Mass and heat transport parameters are then correlated with the radially varying functions of axial flow component and new correlations were developed especially for heat transfer (effective thermal conductivities in axial and radial direction, wall heat transfer coefficient) [135]. Neglecting the interfacial gradients (film diffusion), the governing equations solved for the reactor at steady state are [136]:
Mass balance:

$$\nabla \cdot (-D_i \nabla c_i + \mathbf{u} c_i) = -(1 - \varepsilon_{bed}) a_v D_{eff,i} \frac{2}{d} \frac{\partial c_i}{\partial \zeta}(\zeta = 1) \tag{3.13}$$

whereas the dispersion coefficient matrix is expressed as:

$$D_i = \begin{bmatrix} D_{r,i} & 0 \\ 0 & D_{ax,i} \end{bmatrix} \tag{3.14}$$

Heat balance:

$$\rho_f C p_f \mathbf{u} \cdot \nabla T - \nabla \cdot (\lambda_{eff} \nabla T) = -(1 - \varepsilon_{bed}) a_v \lambda_{pellet} \frac{2}{d} \frac{\partial T}{\partial \zeta}(\zeta = 1) \tag{3.15}$$

whereas the effective thermal conductivity matrix is expressed as:

$$\lambda_{eff} = \begin{bmatrix} \lambda_r & 0 \\ 0 & \lambda_{ax} \end{bmatrix} \tag{3.16}$$

Momentum balance:

$$\frac{\mu_{eff}}{K_E} \mathbf{u} = \nabla \cdot \left[-p\mathbf{I} + \frac{\mu_{eff}}{\varepsilon_{bed}} (\nabla \mathbf{u} + (\nabla \mathbf{u})^T) \right] \tag{3.17}$$

Continuity equation:

$$\nabla \cdot (\rho_f \mathbf{u}) = 0 \tag{3.18}$$

Eq. 3.17 is the extended-Brinkman equation which is recommended for the use of calculating velocity fields in fixed-bed reactors instead of using the conventional plug-flow assumption [137]. The reactor wall effects on the flow in fixed-bed reactors, especially with small reactor diameter to particle diameter ratio (D/d), is included in the Brinkman equation by introducing the radial function of the bed porosity $\varepsilon_{bed}(r)$. The radial porosity function used in this work is as follows [24]:

$$\varepsilon_{bed}(r) = \varepsilon_0 \left(1 + a \cdot exp\left[-b\frac{R-r}{d_p}\right]\right) \tag{3.19}$$

$$a = \frac{0.65}{\varepsilon_0} - 1; \quad b = 6.0 \tag{3.20}$$

The porosity of a cylindrical packing in an infinite bed ε_0 according to Zou et al. [138] equals to 0.32. The inertia resistance in the bed is described by the Ergun hydraulic permeability K_E as [136]:

$$\frac{1}{K_E} = \frac{1}{K_D} + \frac{C_E \rho_f |\mathbf{u}|}{K_D^{1/2}\mu}; \quad C_E = \frac{1.75}{\sqrt{150}\varepsilon_{bed}^2} \tag{3.21}$$

The set of effective heat and mass transport parameters were calculated following the work of Winterberg and Tsotsas et al. [24, 97]:

$$D_{r,i} = 1 - \sqrt{1-\varepsilon_{bed}(r)} D_{AB} + K_1 Pe_m \frac{u(r=0)}{u} f(R-r) D_{AB} \tag{3.22}$$

$$D_{ax,i} = 1 - \sqrt{1-\varepsilon_{bed}(r)} D_{AB} + \frac{u d_p}{2} \tag{3.23}$$

$$\lambda_r = \lambda_{bed} + K_1 Pe_h \frac{u(r=0)}{u} \lambda_f f(R-r) \tag{3.24}$$

$$\lambda_{ax} = \lambda_{bed} + \frac{Pe_h \lambda_f}{2} \tag{3.25}$$

$$f(R-r) = \begin{cases} \left(\dfrac{(R-r)}{(K_2 d_p)}\right)^n & \text{if } 0 < R-r < K_2 d_p \\ 1 & \text{if } R-r > K_2 d_p \end{cases} \tag{3.26}$$

$$K_1 = 1/6.25 \tag{3.27}$$

$$K_2 = 0.40 + 0.6 exp\left(\frac{-Re}{230}\right) \tag{3.28}$$

$$n = 2 \tag{3.29}$$

The effective thermal conductivity of the fixed-bed without gas flow λ_{bed} is calculated according to the model of Tsotsas and Schlünder [24, 139]. The conservation equations were solved with the boundary conditions listed in Table 3.2.

Table 3.2: Boundary conditions applied to the two-dimensional heterogeneous reactor model

$z = 0, \forall r:$	$c_i = c_{i,0}$	$T = T_0$	$\lvert\vec{u}\rvert = u_0$
$z = l_R, \forall r:$	$\frac{\partial c_i}{\partial z} = 0$	$\frac{\partial T}{\partial z} = 0$	$p = 1$ [atm]
$r = 0, \forall z:$	$\frac{\partial c_i}{\partial r} = 0$	$\frac{\partial T}{\partial r} = 0$	$\frac{\partial u}{\partial r} = 0$
$r = R, \forall z:$	$\frac{\partial c_i}{\partial r} = 0$	$T = T_w$	$u = 0$

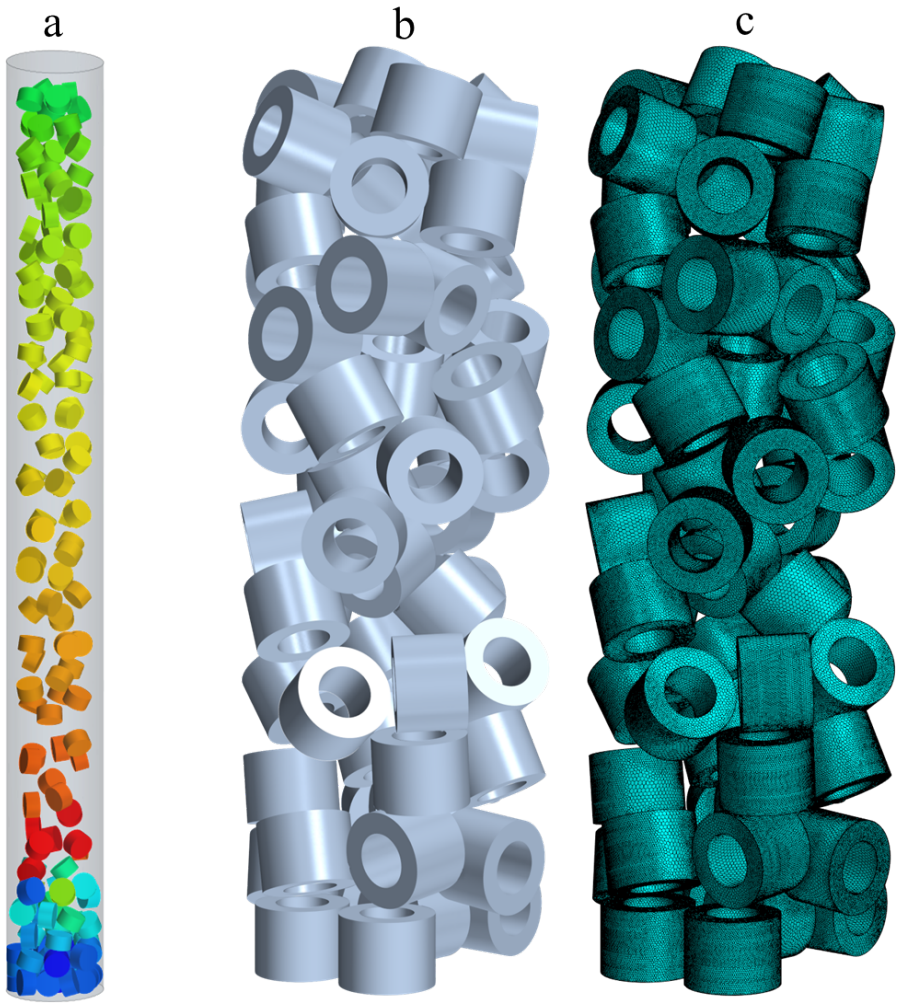

Figure 3.3: Illustration of the general workflow of the particle-resolved CFD approach: a) generating packing from DEM simulations; b) creating bed geometry based on the input from DEM simulations when all the particles are settled; c) meshing the calculation domains.

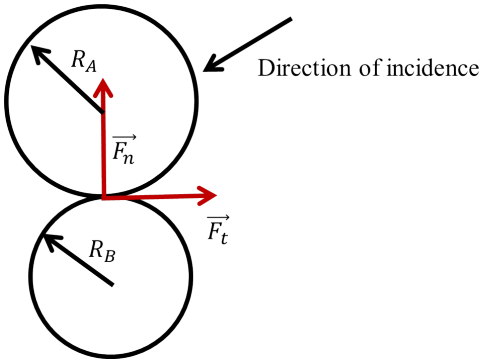

Figure 3.4: Illustration of the normal force component $\vec{F}_n$ and the tangential force component $\vec{F}_t$ acting on DEM particles upon contacting [140].

3.2 Particle-resolved CFD approach

The general work flow of the particle-resolved CFD approach used in this work can be summarized into the following steps. Firstly, a random packing is generated using the discrete element method and the position of each particle center are extracted. For non-spherical particles, the particle orientation information is also extracted. Secondly, a calculation domain is created based on the particle position data from the first step. Thirdly, the calculation domains including the particles and the voids in between are volume meshed. Lastly, physical models are set and boundary conditions as well as the initial conditions are specified. Figure 3.3 illustrates the general work flow for a typical CFD simulation taking the steatite rings as packing example. All steps can be realized in the commercial package STAR-CCM+ [140]. This methodology is first proposed by Eppinger et al. [26] and further applied and developed extensively by Wehinger et al. [64, 81, 117, 118, 141].

3.2.1 Packing generation: Discrete Element Method

Discrete Element Method (DEM) is an explicit numerical method to simulate the motion behavior of many-body solid system by including interparticle contact forces into the equations of motion [47, 140]. Originally proposed by Cundall and Stack [48] for geophysics, DEM has been widely applied to simulate fixed-bed packing as well as fluidized bed [142]. STAR-CCM+ uses a soft contact model which means the rigid particles are allowed to overlap upon contacts [140]. These contact forces between particles are simulated with a variant of the spring-dashpot model in which the spring accounts for the elastic part of repulsive force while the dashpot accounts for energy dissipation during collision [140]. One of the contact force model used in this work is the Hertz-Mindlin model [143, 144]. Taking spherical particles as an example as shown in Figure 3.4, the contact forces between them are:

$$\vec{F}_{contact} = \vec{F}_n + \vec{F}_t \tag{3.30}$$

where $\vec{F}_n$ is the normal force component and $\vec{F}_t$ is the tangential force component. The normal force is calculated as [140]

$$\vec{F}_n = -K_n d_n - N_n v_n \tag{3.31}$$

where K_n is the normal spring stiffness, d_n is the overlap in the normal direction, N_n is normal damping, v_n is the normal velocity component of the relative sphere surface

velocity at the contact point. K_n and N_n are calculated as follows:

$$K_n = \frac{4}{3} E_{eq} \sqrt{d_n R_{eq}} \tag{3.32}$$

$$N_n = \sqrt{(5 K_n M_{eq})} N_{n,damp} \tag{3.33}$$

where the equivalent radius R_{eq} is a function of the radii of the spheres A and B, R_A and R_B:

$$R_{eq} = \frac{1}{\frac{1}{R_A} + \frac{1}{R_B}} \tag{3.34}$$

The equivalent particle mass is defined as a function of the mass of the spheres A and B, M_A and M_B:

$$M_{eq} = \frac{1}{\frac{1}{M_A} + \frac{1}{M_B}} \tag{3.35}$$

The equivalent Young's modulus is a function of the Young's modulus of the spheres A and B, E_A and E_B:

$$E_{eq} = \frac{1}{\frac{1-\nu_A^2}{E_A} + \frac{1-\nu_B^2}{E_B}} \tag{3.36}$$

where ν_A and ν_B are the Poisson's ratios of sphere A and B. The tangential force is defined as [140]:

$$\vec{F_t} = \begin{cases} -K_t d_t - N_t v_t & \text{if } |K_t d_t| < |K_n d_n| C_{fs} \\ \frac{|K_n d_n| C_{fs} d_t}{|d_t|} & \text{otherwise} \end{cases} \tag{3.37}$$

where C_{fs} is a static friction coefficient, d_t is overlap in the tangential directions at the contact point, v_t is the tangential velocity component of the relative sphere surface velocity at the contact point, K_t is the tangential spring stiffness, and N_t is the tangential damping.

$$K_t = 8 G_{eq} \sqrt{d_n R_{eq}} \tag{3.38}$$

$$N_t = \sqrt{(5 K_t M_{eq})} N_{t,damp} \tag{3.39}$$

The equivalent shear modulus is calculated as:

$$G_{eq} = \frac{1}{\frac{2(2-\nu_A)(1+\nu_A)}{E_A} + \frac{2(2-\nu_B)(1+\nu_B)}{E_B}} \tag{3.40}$$

The normal and tangential damping coefficients are calculated as:

$$N_{n,damp} = \frac{-ln(C_{n,rest})}{\sqrt{\pi^2 + ln(C_{n,rest})^2}} \tag{3.41}$$

$$N_{t,damp} = \frac{-ln(C_{t,rest})}{\sqrt{\pi^2 + ln(C_{t,rest})^2}} \tag{3.42}$$

where $C_{n,rest}$ and $C_{t,rest}$ are the normal and tangential coefficients of restitution [140].

For particle-wall collisions, the wall radius and mass are assumed to be infinite and thus the equivalent radius and mass are reduced to $R_{eq} = R_{particle}$ and $M_{eq} = M_{particle}$, respectively [140].

For cylinder or ring type packings, the linear spring contact model is used which is the only available model for cylindrical particles in STAR-CCM+ [140]. In this model the normal and tangential spring constants are defined as:

$$K_n = \frac{4}{3}\sqrt{\lambda_{max}} E_{eq} R_{eq} \tag{3.43}$$

$$K_t = 8\sqrt{\lambda_{max}} G_{eq} R_{eq} \tag{3.44}$$

$$\lambda_{max} = \frac{\delta_{max}}{R_{eq}} \tag{3.45}$$

where δ_{max} is the maximum overlap. The normal and tangential damping coefficients are calculated as:

$$N_n = 2N_{n,damp}\sqrt{K_N M_{eq}} \tag{3.46}$$

$$N_t = 2N_{t,damp}\sqrt{K_t M_{eq}} \tag{3.47}$$

3.2.2 Meshing

Mesh to a CFD simulation should be appreciated as the skeleton to a human body. Without a valid mesh, a numerical simulation cannot run or converge. Not only that, mesh determines the accuracy and reliability of a CFD simulation. To the best of our knowledge, choices of the type and size of a mesh are often made as trade-off between accuracy and computational efforts. Hence, a mesh convergence study is always required in a CFD simulation to find the maximum possible mesh size based on which the simulation results do not vary any more.

In this work, the meshing strategy developed by Eppinger et al. [26] is followed. This meshing strategy is designed specifically for modeling particle-resolved fixed-bed reactor using STAR-CCM+ [140]. Figure 3.5 shows the details of the applied mesh. A dense polyhedral volume mesh is used for the main calculation domain including both fluid and solid regions. This type of mesh is recommended for solving conjugate heat transfer problems over tetrahedral mesh due to its flexibility to have a higher number of neighboring cells and a better gradient approximation [140]. As described in the work of Eppinger et al. [26], a base size of one particle diameter is suggested for spherical packings. All the mesh properties are set as percentage of this base size. This strategy simplifies the procedure for mesh independence studies so that one has only to vary the base size. Two prism mesh layers are set for resolving boundary flows. The prism layer mesh has the benefit of capturing the flow and temperature field in the near-wall region with a lesser amount of cells [26]. For simulating the heat transfer between fluid and solid regions, conformal mesh in the fluid-solid interface is required.

'Local flattening' methods [26, 44] are used in order to deal with the contact point problem for both spheres and rings. This method locally modifies the surface element when the defined minimal distance between two surfaces is reached. In this way, meshes with very high skewness are avoided which is beneficial for simulation convergence. This method creates artificially gaps in-between the contacting particles. Since the gaps are filled with fluid cells, certain errors for example in the bed void fraction and pressure drops in the models are introduced. However, this effect is kept minimal with a fine structured mesh [26]. Extrusions in both the inlet and outlet boundaries are taken to avoid the influence of the boundary conditions and to help

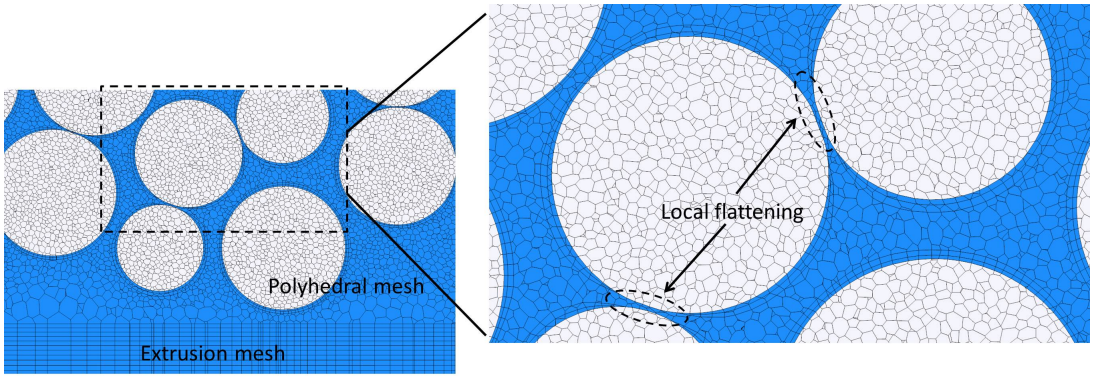

Figure 3.5: Illustration of different mesh types applied in this work taking a spherical packing as example.

with the convergence. As rule of thumb, five particle layers for the inlet extrusion and more than ten particle layers for the outlet extrusions are suggested [26] .

3.2.3 Fundamental equations

The set of governing equations for modeling a laminar reacting flow through a heterogeneous catalytic reactor include the Navier-Stokes equations (conservation of mass and momentum) and conservation equations of participating species and energy. Since all the simulations presented in this work were carried out in steady state, the time-independent version of all the governing equations are introduced in this section. The equations are formulated in Cartesian coordinates and Einstein convention is adopted [25].
Conservation of mass:

$$\frac{\partial\left(\rho u_i\right)}{\partial x_i} = 0 \tag{3.48}$$

where ρ is the density, u_i is the Cartesian components i of the velocity vector and x_i is the Cartesian coordinates i ($i = 1, 2, 3$). This equation is often called the continuity equation [145].
Conservation of momentum:

$$\frac{\partial}{\partial x_j}\left(\rho u_i u_j\right) + \frac{\partial p}{\partial x_i} + \frac{\partial \tau_{ij}}{\partial x_j} = 0 \tag{3.49}$$

τ_{ij} is the stress tensor and is calculated as:

$$\tau_{ij} = -\mu\left(\frac{\partial u_i}{\partial x_j} + \frac{\partial u_j}{\partial x_i}\right) + \left(\frac{2}{3}\mu - \kappa\right)\delta_{ij}\frac{\partial u_k}{\partial x_k} \tag{3.50}$$

where μ is the dynamic viscosity of the mixture, κ is the bulk viscosity which is set to zero at low speed of the flow, and δ_{ij} is the Kronecker delta which is one when $i = j$, else zero [146].
Conservation of species i:

$$\frac{\partial\left(\rho u_j Y_i\right)}{\partial x_j} + \frac{\partial j_{i,j}}{\partial x_j} - R_i^{hom} = 0, \quad i = 1, ..., N_g \tag{3.51}$$

where Y_i is the mass fraction of species i in the mixture, N_g is the number of gas phase species and R_i^{hom} is the net rate of production of species i due to homogeneous

chemical reactions [147] and are calculated as [148]:

$$R_i^{hom} = M_i \sum_{k=1}^{K_g} \nu_{ik} A_k T^{\beta_k} exp\left(-\frac{E_{a,k}}{RT}\right) \prod_{j=1}^{N_g} c_j^{\nu\prime_{jk}} \tag{3.52}$$

where K_g is the number of elementary gas phase reactions, ν_{ik} is the stoichiometric coefficient of species i in reaction k (positive as product and negative as reactant), $\nu\prime_{jk}$ is the stoichiometric coefficient of species j in reaction k when it is reactant, A is the pre-exponential factor, β is the temperature coefficient, E_a is the activation energy and c_j is the concentration of species j [148].
The diffusion mass flux $\vec{j_i}$ is calculated as:

$$\vec{j_i} = -\rho D_{i,m} \frac{Y_i}{X_i} \nabla X_i \tag{3.53}$$

In Equation 3.53, X_i is the mole fraction of species i, $D_{i,m}$ is the diffusion coefficient of species i in the mixture. $D_{i,m}$ can be calculated as mass average of the binary diffusion coefficient as

$$D_{i,m} = \frac{1 - Y_i}{\sum_{j \neq i}^{N_g} \frac{X_j}{D_{i,j}}} \tag{3.54}$$

Binary diffusion coefficient $D_{i,j}$ can be calculated from the Chapman-Enskog equation as [140]:

$$D_{i,j} = \frac{2.66 \cdot 10^{-7} \cdot T^{3/2}}{p \cdot M_{i,j}^{1/2} \cdot \sigma_{i,j}^2 \cdot \Omega(T^*)} \tag{3.55}$$

where $M_{i,j} = 2M_iM_j/(M_i + M_j)$. $\sigma_{i,j}$ can be calculated by applying the Lorentz-Berthelot mixing rule to the Lennard-Jones characteristic length of each component as:

$$\sigma_{i,j} = \frac{\sigma_i + \sigma_j}{2} \tag{3.56}$$

the collision integral $\Omega(T^*)$ is a function of reduced temperature T^* which is defined as [140]:

$$T^* = \frac{k_B T}{\varepsilon_{i,j}} \tag{3.57}$$

with k_B being the Boltzmann constant. $\varepsilon_{i,j}$ can be calculated by applying the Lorentz-Berthelot mixing rule to the Lennard-Jones energy of each component to be:

$$\varepsilon_{i,j} = \sqrt{\varepsilon_i \cdot \varepsilon_j} \tag{3.58}$$

Function parameters for $\Omega(T^*)$ are not listed here but are well documented in literature [149].
Conservation of energy:

$$\frac{\partial (\rho u_j h)}{\partial x_j} - \frac{\partial}{\partial x_j}\left(\lambda \frac{\partial T}{\partial x_j}\right) + \frac{\partial}{\partial x_j} \sum_{i}^{N_g} h_i j_{i,j} - u_j \frac{\partial p}{\partial x_j} - \sum_{i}^{N_g} h_i R_i^{hom} = 0 \tag{3.59}$$

where h is the enthalpy of the mixture and is calculated as mass average of the enthalpy of each species h_i via

$$h = \sum_{i}^{N_g} Y_i h_i \tag{3.60}$$

The enthalpy of each species h_i is a function of the temperature and is calculated as:

$$h_i = h_i(T_{ref}) + \int_{T_{ref}}^{T} c_{p,i} \cdot dT \tag{3.61}$$

The specific heat capacity at constant pressure of each species $c_{p,i}$ is computed from the NASA polynomial functions with the thermodynamic data accompanied with the reaction micro kinetics. The thermal conductivity of the mixture λ is a function of the local composition and temperature and can be calculated via the kinetic theory [149].

It is common practice to model the heat transport in solid catalyst pellet as well, e.g. for conjugated heat transfer. The energy conservation for solid phase can be formulated as:

$$\frac{\partial}{\partial x_j}\left(\lambda \frac{\partial T}{\partial x_j}\right) = s_h \tag{3.62}$$

where λ is the thermal conductivity of the solid material and s_h in unit of $\mathrm{W/m^3}$ is the heat source due to chemical reactions or radiative heating of the solid [150].
The system of governing equations is closed with the ideal gas law:

$$p = \frac{\rho R T}{\sum_i^{N_g} X_i M_i} \tag{3.63}$$

where M_i is the molar mass of species i.

3.2.4 Modeling reaction

On the catalytic surface, heterogeneous catalytic surface reactions take place, which are coupled with the gas phase stream via a boundary flux. At steady state, the consumed or produced species have to diffuse to and away from the catalytic surface as follows [146]:

$$\vec{n}\left(\vec{j_i}\right) = R_i^{het} \tag{3.64}$$

where $\vec{n}$ is the outward-pointing unit vector normal to the surface, $\vec{j_i}$ is the diffusive mass flux. R_i^{het} is the heterogeneous surface reaction rate which is given per unit geometric surface area and can be computed as:

$$R_i^{het} = \eta \frac{A_{cat}}{A_{geo}} M_i \dot{s}_i \tag{3.65}$$

where A_{cat}/A_{geo} is the ratio of catalytically active area to geometric area, $\dot{s}_i$ is the molar net production rate of species i in unit of $\mathrm{mol \cdot\ m^{-2} s^{-1}}$. Consequently, the product of A_{cat}/A_{geo} and $\dot{s}_i$ has now the unit referred to the actual catalytically active surface area. η is defined as the effectiveness factor which includes the effect of internal mass transfer resistance if the porous structure of the catalyst pellets are considered [147].

In general, two categories of kinetic models are available to describe rate of reactions R_i^{het}. One is the macrokinetics which simplifies the complex reaction networks into few representing (apparent) reaction steps with semi-empirical reaction rate expressions [151]. The parameters, e.g. rate constant and (apparent) activation energy are typically obtained from a set of kinetic measurement experiments in a differential reactor [152]. This type of kinetic model is easy to use and shows decent performance. However, one has to be careful not to extrapolate the operational conditions

(p, T and so on) beyond the kinetic measuring boundary [153]. When applying these kinetic models which are usually derived with respect to the total mass or volume of catalyst, one shall convert the unit into mol$\cdot$ m^{-2}s^{-1} using the catalyst density, specific surface area, and volumetric unit. In Chapter 8, coupling of macrokinetics of n-butane oxidation to CFD model will be discussed in detail with examples for kinetic expressions.

The other type of kinetic model is the microkinetics [154] which is a comprehensive and mechanistic description of sequences of elementary steps occurring on a catalyst [155]. It includes adsorption and desorption of the participating species as well as reaction intermediates and surface reactions on the active sites on the catalyst surface [156, 157]. The rate parameters are obtained from first-principles calculations and from spectroscopic experiments. This type of models can provide detailed insights into the reaction mechanism and (in theory) could be extrapolated to a wide range of conditions [158]. The availability of such a microkinetic model is somewhat limited to model catalysts which are typically single crystals [159]. The state-of-the-art concept to model surface reactions using micro-kinetics in CFD is the mean field approximation. This concept assumes randomly and uniform distributed adsorbates on the catalyst surface which are described by the surface temperature and surface coverage of each surface species θ_i [150]. Under this condition, $\dot{s}_i$ in Eq. 3.65 is calculated as:

$$\dot{s}_i = \sum_{k=1}^{K_s} \nu_{ik} k_{fk} \prod_{j=1}^{N_g+N_s} c_j^{\nu\prime_{jk}} \tag{3.66}$$

where K_s is the number of elementary surface reactions including adsorption and desorption, c_i is the species concentration which is in unit of mol/m^2 for surface species and in unit of mol/m^3 for the gas phase species, N_s is the total number of adsorbed species, k_{fk} is the forward reaction coefficient of reaction k which is computed as:

$$k_{fk} = A_k T^{\beta_k} exp\left(-\frac{E_{ak}}{RT}\right) \prod_{i=1}^{N_s} \theta_i^{\mu_{ik}} exp\left(\frac{\varepsilon_{ik}\theta_i}{RT}\right) \tag{3.67}$$

with the surface coverage θ_i defined as:

$$\theta_i = c_i \sigma_i \Gamma^{-1} \tag{3.68}$$

Here, σ_i is the coordinate number which describes the number of surface sites covered by species i and Γ is the surface site density in unit of mol/m^2. At steady state, the following condition is fulfilled for all surface species [150]:

$$\frac{\partial \theta_i}{\partial t} = \frac{\dot{s}_i \sigma_i}{\Gamma} = 0 \tag{3.69}$$

The two extra coverage parameters, μ_{ik} and ε_{ik}, in Eq. 3.67 describe the variation of the binding states of adsorption as a function of the surface converges [146].

For adsorption steps, the sticking coefficient is often given instead of the rate constant in the microkinetics from literature. If the rate constant of adsorption steps are required for the simulation program, one can convert them from sticking coefficients as follows:

$$A_k = \left(\frac{S_i}{1 - S_i/2}\right) \frac{1}{\Gamma^\tau} \sqrt{\frac{RT}{2\pi M_i}} \tag{3.70}$$

where S_i is the initial sticking coefficient, τ is the sum of all stoichiometric coefficients of the surface reactants.

3.2.5 Turbulence model

Turbulent flow is characterized as spatial and temporal highly unsteady (chaotic), fluctuating, diffusive, and dissipative in nature [145]. Rotational flow structures, so called turbulence eddies which spread a wide range of length scales, are present in a fluid in a turbulent state [160]. Interactions between eddies at different length scales promote effective contact between fluid particles and enhance the momentum, heat and mass transfer rates [12]. Those effects are often desired in industrial fixed-bed reactors despite the compromise of high pressure drop. Turbulence is indeed a science in its own right [161] and the discussion here is restricted to the key aspects in engineering modeling approach.

Flow regimes inside a fixed-bed reactor can be categorized according to the particle related Reynolds number which is defined as:

$$Re_p = \frac{u_{in} \cdot \rho_{in} \cdot d_p}{\eta} \tag{3.71}$$

When Re_p is higher than 300, the flow is treated as fully turbulent [25, 33, 162]. The most accurate way to simulate turbulent flow is the so-called Direct Numerical Simulation (DNS) which solves the Navier-Stokes equations without averaging and approximation of the variables describing the system [145]. Thus, a history record of all the flow motions down to the smallest scale is calculated [12]. So far, this method is too expensive to achieve wide application for flow inside complex geometries and, as a result, is limited as a research tool for fundamental flow studies [145]. A more popular approach in engineering to model turbulence is the Reynolds-averaged Navier-Stokes (RANS) turbulence model. Since this approach does not resolve small-scale phenomena, it requires less computational efforts. In RANS equations, variables like velocity component, pressure, energy, and species concentration are decomposed into their mean values $\bar{\phi}(x_i)$ and their fluctuating components $\phi'(x_i, t)$ [140, 145]:

$$\phi(x_i, t) = \bar{\phi}(x_i) + \phi'(x_i, t) \tag{3.72}$$

The continuity and momentum equations can be then written with respect to the mean terms [145]:

$$\frac{\partial \left(\rho \bar{u}_i\right)}{\partial x_i} = 0 \tag{3.73}$$

$$\frac{\partial}{\partial x_j}\left(\rho \bar{u}_i \bar{u}_j + \rho \overline{u_i' u_j'}\right) + \frac{\partial \bar{p}}{\partial x_i} - \frac{\partial \bar{\tau}_{ij}}{\partial x_j} = 0 \tag{3.74}$$

An additional term in form of $\rho \overline{u_i' u_j'}$ appears compared to the original form in Eq. 3.49. This term is called the Reynolds stress which is a tensor quantity [145]. In order to solve the set of equations, a turbulence model to approximate the Reynolds stress tensor in terms of the mean flow quantities is required [140]. One way to do so is to use the eddy viscosity hypothesis which is based on an analogy between molecular and turbulent motions [12]. It introduces a turbulent eddy viscosity μ_t and describes the Reynold stresses as [145]:

$$-\rho \overline{u_i' u_j'} = \mu_t \left(\frac{\partial \bar{u}_i}{\partial x_j} + \frac{\partial \bar{u}_j}{\partial x_i}\right) - \frac{2}{3}\rho \delta_{ij} k \tag{3.75}$$

where k is the turbulent kinetic energy:

$$k = \frac{1}{2}\overline{u_i' u_j'} \tag{3.76}$$

The turbulent viscosity can be related to the characteristic velocity u_t and length scales of turbulence l_t. Thus, various turbulence models, especially two-equation models, are developed to estimate these two aforementioned parameters [12, 163–165]. The most popular one is the '$k-\varepsilon$' model. In this model turbulent viscosity is related to the turbulent kinetic energy k and turbulent energy dissipation rate ε:

$$\mu_t = \frac{C_\mu \rho k^2}{\varepsilon} \tag{3.77}$$

where C_μ is an empirical coefficient [12]. Two equations are formulated for k and ε [12]:

$$\frac{\partial\left(\rho \bar{u}_i k\right)}{\partial x_i} = \frac{\partial}{\partial x_i}\left(\frac{\mu_t}{\sigma_k}\frac{\partial k}{\partial x_i}\right) + G - \rho\varepsilon \tag{3.78}$$

$$\frac{\partial\left(\rho \bar{u}_i \varepsilon\right)}{\partial x_i} = \frac{\partial}{\partial x_i}\left(\frac{\mu_t}{\sigma_\varepsilon}\frac{\partial \varepsilon}{\partial x_i}\right) + \frac{\varepsilon}{k}\left(C_1 G - C_2 \rho\varepsilon\right) \tag{3.79}$$

$$G = \frac{1}{2}\mu_t \left[\nabla \bar{u} + (\nabla \bar{u})^T\right]^2 \tag{3.80}$$

where σ_k is a turbulence Prandtl number and its value is approximately unity [145]. The five empirical parameters $C_\mu, C_1, C_2, \sigma_k, \sigma_\varepsilon$ in Equations 3.77, 3.78 and 3.80 are obtained from experiments of simple flows and the values are:

$$C_\mu = 0.09, \quad C_1 = 1.44, \quad C_2 = 1.92, \quad \sigma_k = 1.0, \quad \sigma_\varepsilon = 1.3 \tag{3.81}$$

The above mentioned transport equations together with the parameters in Eq. 3.81 Complete the so-called 'standard $k-\varepsilon$' model [166]. It is known that this model is valid only for fully turbulence flows and it over-predicts turbulence generation in regions where the mean flow is highly accelerated [12]. Several attempts have been proposed to modify this model for specific applications, for example, by introducing damping functions to some of the coefficients for low-Reynolds number flow conditions [140].

The influence of walls to the turbulent flow is a non-trivial task which brings difficulty to simulate wall-bounded flows [12]. To supplement the wall boundary conditions and to avoid an unaffordable dense mesh near the wall, 'wall functions' are introduced which are based on experimental findings. Between no-slip conditions at the wall and free stream flow away from the wall, three layers can be subdivided for the near-wall region: a viscous sub-layer, a buffer layer and a fully turbulent layer. In the viscous sub-layer, molecular viscosity dominants and the flow resembles a laminar one. In the buffer layer, molecular viscosity and turbulence play an equally important role. In the fully turbulent layer, the turbulence dominants.

The majority of the simulations in this work are carried out at laminar flow conditions. In case the system is turbulent or in the transition flow regime, the 'Realizable $k-\varepsilon$' model with all wall treatment is applied. For the viscous sub-layer and the fully turbulent layer, velocity and other turbulence quantities can be calculated as linear function and logarithmic function of the dimensionless distance from the wall, respectively. For the buffer layer, blended wall functions are used [140]. This turbulence model is an improvement over the 'standard $k-\varepsilon$' model due to the addition of a new transport equation for the turbulent dissipation rate ε and treating C_μ as a function of mean flow and turbulence properties [140, 167]. The turbulence models, as discussed above, are semi-empirical in nature since they rely on adjustable parameters from experimental fittings. However, they are so far the most efficient models for industrial fixed-bed reactor simulations [12].

4 Catalytical Methane Combustion on a Platinum Gauze

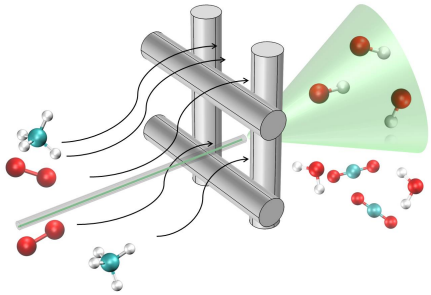

Noble metal gauze catalysts are used in chemical industry for rapid exothermic reactions. Examples are the ammonia oxidation to nitric oxide (Ostwald process) [17, 168, 169] and the ammoxidation of methane to hydrogen cyanide (Andrussow process) [170] both on Pt/Rh gauzes. Despite their apparent simplicity as adiabatic furnaces, gauze reactors are highly complex. In particular, the intricate interplay between physical transport processes of mass, heat, and momentum with reactions at the gauze surface and possibly reactions in the gas phase make both experimental and numerical investigation a highly challenging task. A particular handicap with regard to gaining mechanistic insight is the high reaction rate of these processes. Catalytic oxidations on noble metal gauzes typically proceed at milli- to microsecond timescales, which translates into submillimeter gradients in a flow reactor. The intrinsic kinetics of these reactions is virtually not accessible by experiments, due to pronounced mass and heat transport limitations [171].

Due to the corrosive nature and toxicity of compounds like NH_3, HCN or NO, catalytic methane combustion was studied as test reaction.

$$CH_4 + 2O_2 \rightarrow CO_2 + 2H_2O \quad \Delta H_r(298K) = -802\,\mathrm{kJmol^{-1}} \tag{4.1}$$

Concentration profiles for the main species (CH_4, O_2, CO_2, H_2O) as well as for minor species (H_2, CO, C_2H_6, C_2H_4, C_2H_2) are measured by means of a capillary sampling technique. Fiber based Laser Induced Fluorescence spectroscopy is used to measure quantitative concentration profiles of OH· radicals being an indicator species for gas phase oxidation reactions. Details of the experiments are given in [86, 172]. Insight into extent and nature of the interaction between surface and gas phase chemistry, as well as chemistry and transport is obtained by conducting three-dimensional CFD simulations of flow coupled with heat and mass transport, as well as detailed heterogeneous and homogeneous reaction kinetics.

This chapter is adopted from publication: H. Schwarz, Y. Dong and R. Horn, Catalytic Methane Combustion on a Pt Gauze: Laser-Induced Fluorescence Spectroscopy, Species Profiles, and Simulations, Chemical Engineering & Technology 39 (11) (2016) 2011-2019.

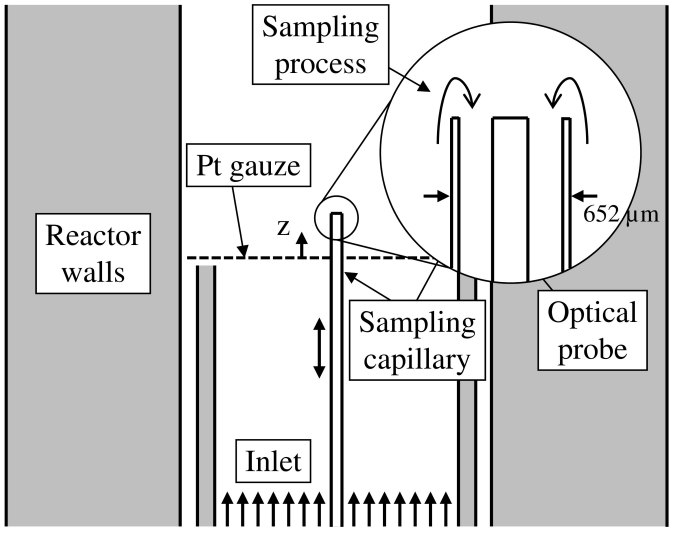

Figure 4.1: Schematic drawing of the experimental setup. The magnification shows the fiber-optic probe for LIF measurements positioned inside the sampling capillary [86].

4.1 Experimental details

The reactor assembly is schematically depicted in Figure 4.1. The platinum gauze consists of 3600 meshes/cm^2 with a wire diameter of 40 μm and is mounted inside the reactor as shown. The fused-silica flow reactor is heated by an electrical furnace and operated at a slightly elevated pressure of 1.5 bar. The sampling capillary can be traversed along the center of the reactor, allowing reactant mixture samples to be extracted continuously. Placing the capillary by using a stepper motor permits positioning with micrometer accuracy. The magnification in Figure 4.1 illustrates the sampling process and shows how the fiber-optic probe for LIF detection is accommodated inside the sampling capillary. The sampling rates are adjusted such that they are considerably smaller than the total flow rate, assuring that the main flow remains unaffected by the sampling. Rapid sample extraction and radical removal by collisional wall quenching [4] inhibit reaction progress inside the sampling capillary and hence ensure unbiased ex situ sample analysis. The composition analysis was done using a calibrated mass spectrometer (Pfeiffer Vacuum) and Ar as internal standard. Due to condensation, water was removed from the sampling stream and was calculated from the oxygen balance.

In the experiment, the Pt gauze was prepared and activated in a similar manner as described by de Smet et al. [173]. It was first reduced in a flow of 10 vol % H_2 in Ar while heating the reactor up to 700 °C. Then, the catalyst was activated using a C_2H_6/O_2/Ar 3:2:5 mixture. The actual experiments were conducted with a CH_4/O_2 mixture diluted in 80 vol% Ar. The flow rates were 120 mL$_N$min^{-1} CH_4, 480 mL$_N$min^{-1} O_2 and 2400 mL$_N$min^{-1} Ar, corresponding to an equivalence ratio of ϕ=0.5. The furnace temperature was held at 700 °C.

The experiments were previously carried out by Dr. Heiner Schwarz and more details of the measurement are presented in his dissertation [86].

4.2 Simulation details

A representative geometry of the experimental gauze reactor was used as the computational domain as shown in Figure 4.2 following the work of de Smet et al. [173] and Quiceno et al. [148]. Due to symmetry, only 1/4 of the gauze surface was calculated and periodic boundary conditions were applied for all other surfaces except for the inlet, outlet and gauze surface. The standard velocity inlet and pressure outlet boundary conditions were used. Inlet temperature and inlet mass fractions of the species were specified to match the experiments. The length of the calculation domain extended from 2 mm upstream to 2 mm downstream the gauze.

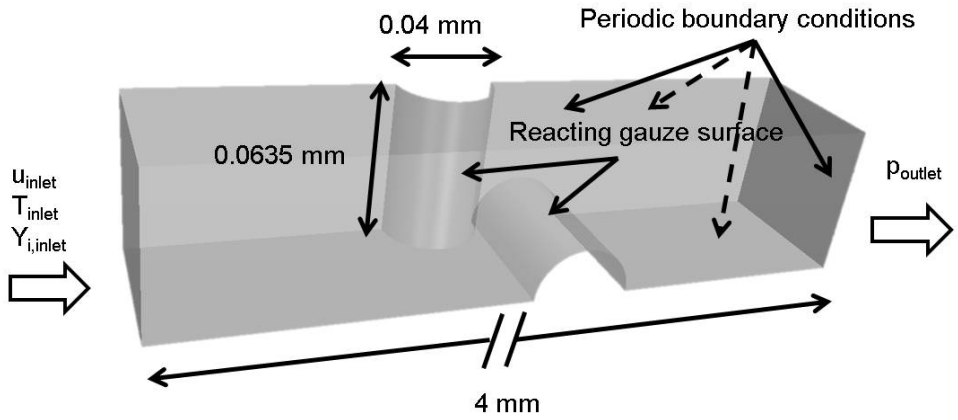

Figure 4.2: Illustration of the computation domain of the catalytic gauze reactor and boundary conditions applied.

All simulations assumed steady state and laminar flow and were conducted by the commercial CFD code STAR-CCM+ 10.04 [140]. To limit the computational efforts and reach convergence, the gauze temperature was assumed to be isothermal. The GRI 3.0 mechanism [174] was used to describe the gas phase chemistry and a mechanism from Deutschmann et al. [175] was used for describing the methane oxidation on Pt surfaces. Both mechanisms were imported into STAR-CCM+ 10.04 [140] as CHEMKIN files and the build-in stiff solver DARS was used for handling the microkinetics. For improving efficiency, the operator splitting algorithm was used, which decouples the transport equations and the chemical reactions [176].

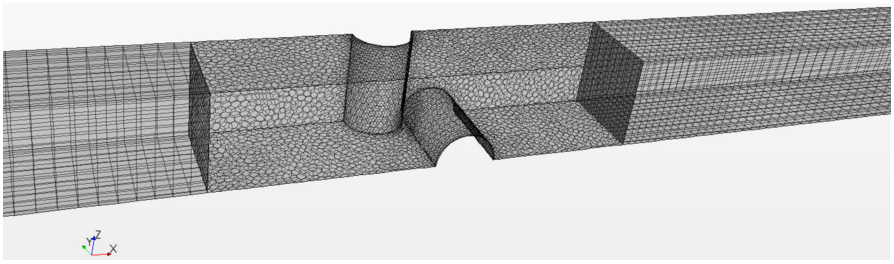

Figure 4.3: Meshed computation domain of the catalytic gauze reactor.

Due to the complex system and the stiffness caused by the homogeneous and

heterogeneous reactions, different meshing strategies were applied in the computational domain. A dense polyhedral mesh was used in the volume around the gauze while directed mesh were used elsewhere as shown in Figure 4.3. A mesh conformity of 100 % at the interfaces between the two kinds of meshing and the cell quality was verified. All the mesh parameters were set as percentage of the base size. Table 4.1 lists some characteristic number of the mesh. The dense polyhedral mesh in the region near the gauze is the most demanding part considering the small size of the gauze compared to the whole computational domain. A fine mesh is used in this region due to the steep gradients around the gauze. Mesh independence study was verified for base size of $3 \cdot 10^{-5}$ m and $2 \cdot 10^{-5}$ m. Both sizes gave identical results as shown in Figure 4.4; therefore, all simulations were carried out with a base size of $3 \cdot 10^{-5}$ m.

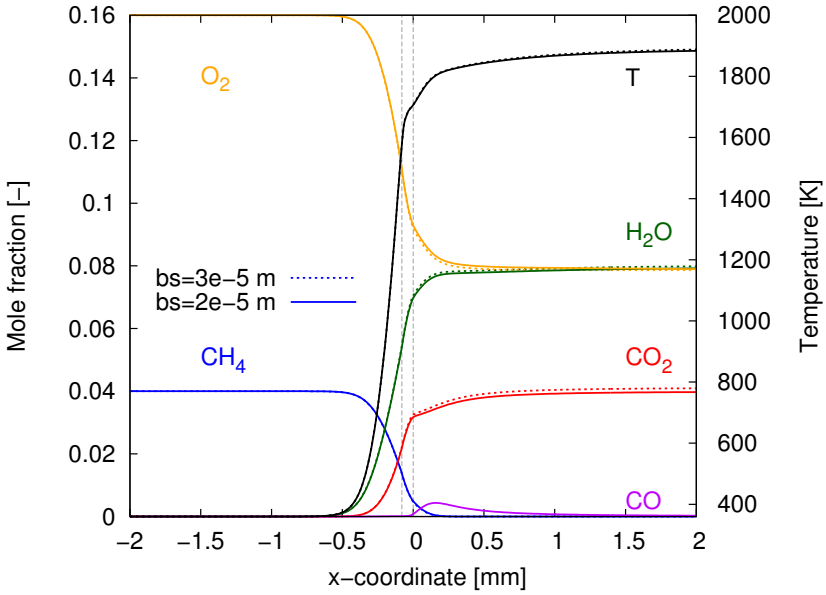

Figure 4.4: Mesh independence study. Mesh convergence is achieved at base size of $3 \cdot 10^{-5}$.

Table 4.1: Mesh parameters for simulating the gauze reactor.

Base size [m]	Total number of cells [-]	Number of polyhedral cells [-]
$3 \cdot 10^{-5}$	84617	29217
$2 \cdot 10^{-5}$	184029	71829

4.3 Results and discussion

Experimental and simulated species profiles along the centerline of the reactor are shown in Figure 4.5. A gauze temperature of 1500 K and an inlet temperature of 360 K were used in the simulation. The top plot in Figure 4.5 shows mole fractions of the reactants and the major products with respect to the left axis and the simulated temperature profile with respect to the right axis. The bottom plot in Figure 4.5 shows the mole fraction profiles of the minor species on the left axis and the OH·

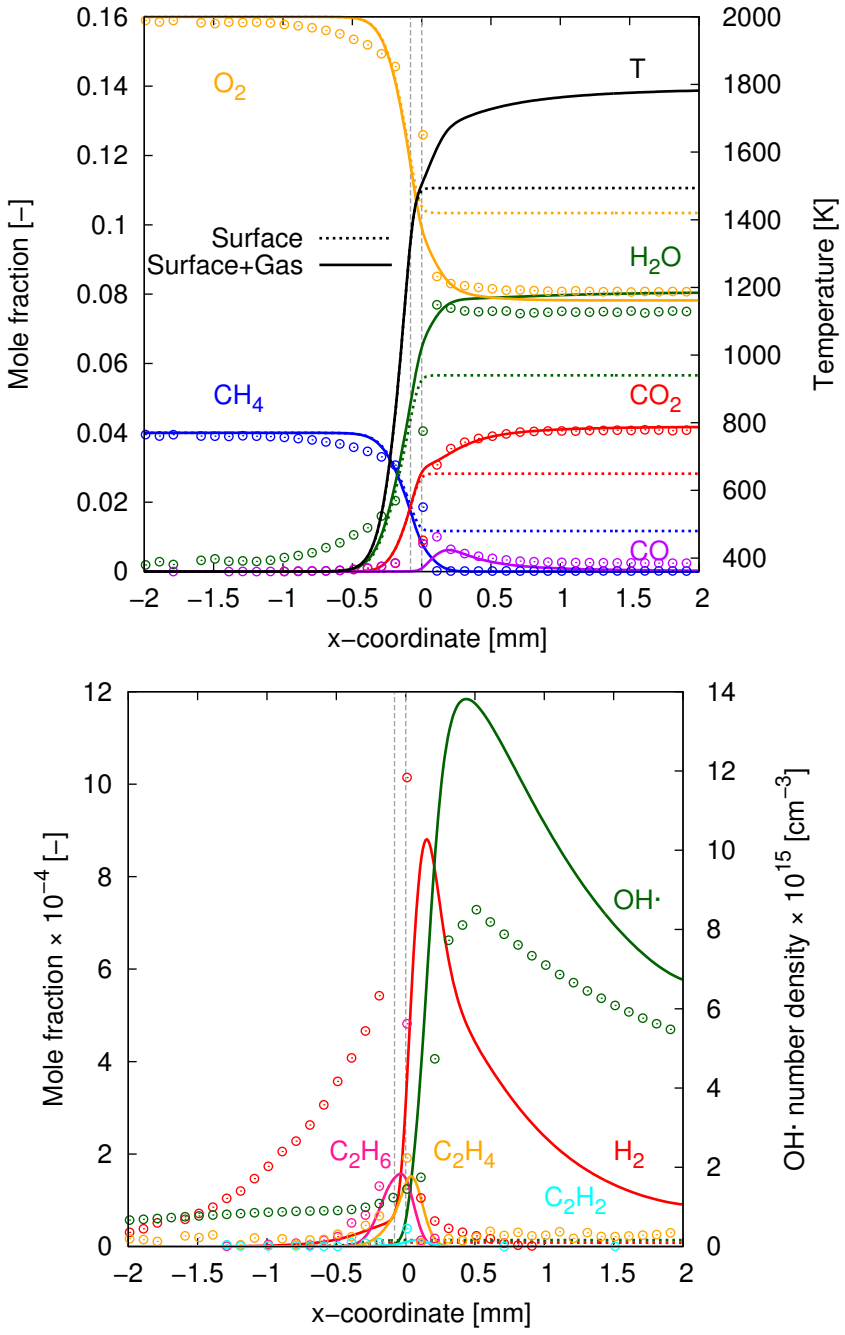

Figure 4.5: Simulated profiles (lines) and measured profiles (dots) of the main species and temperature (top) and the minor species and OH· (bottom) for $\phi = 0.5$, diluted in 80 % at 1.5 bar and a total flow rate of 3000 mL_N/min. Simulations results are given when surface reactions are considered alone (Surface) and combined with gas phase reactions (Surface + Gas). The gauze temperature was set to 1500 K and the inlet temperature to 360 K. The dotted grey lines indicate the location of the gauze.

number density profile on the right axis. The experimental OH· profile was calculated by deconvolution of the raw data with the instrumental function [86].

From the experimental data, it is evident that the reaction is anchored at the gauze located in between the gray dashed lines. CH_4 is totally consumed and the major products are CO_2 and H_2O. About 1 % CO and 0.1 % H_2 are formed in close proximity to the gauze. Due to diffusion, the experimental H_2 profile begins already 2 mm upstream the gauze. The fact that the experimental H_2 profile does not extend downstream the gauze indicates that H_2 is consumed by gas phase reactions there, which are not operative at the low temperatures upstream the gauze. Traces of C_2H_6, C_2H_4 and C_2H_2 are also observed in the vicinity of the gauze. These C_2 products are another indicator of gas phase methane dimerization at very high temperatures [177].

Figure 4.5 also show the simulated centerline profiles. For the main species, good agreement between measured and simulated profiles is reached only if both surface and gas phase chemistry are included in the model. If the gas phase reactions are omitted from the model, the gradients upstream the gauze do not change but strong deviations occur downstream the gauze (solid vs. dotted line). This indicates that the gradients upstream the gauze are a consequence of diffusion, with little or no gas phase reactions taking place at the low temperatures there. The fact that the simulated gradients upstream the gauze slightly sharper than the measured gradients is due to the finite resolution of the sampling process. The gradients downstream of the gauze are the result of both diffusion and gas phase reactions. At a gauze temperature of 1500 K, surface reactions alone account for about two-thirds of the experimental CH_4 conversion (dotted line). If gas phase reactions are not included in the model, the experimentally observed full CH_4 conversion cannot be reproduced. With both surface and gas phase reactions in the model, good agreement between experiment and simulations is reached for the main species. The occurrence of gas phase reactions is also confirmed by the predictions of C_2 species, which are included in the gas phase microkinetic model [174] but not in the surface microkinetic model [175]. The predicted temperature downstream the gauze is higher than the value of 1650 K determined experimentally from the Boltzmann plot [86]. This is mainly due to the periodic boundary conditions used to constrict the model domain which precludes radial heat transport towards the colder reactor tube wall.

As shown in Figure 4.5, agreement between measured and simulated profiles is less good for the minor species. Surface chemistry alone predicts very low amounts of H_2 and OH· radicals which keep constant after the gauze. If gas phase reactions are included in the model, the measured OH· radical profile is qualitatively reproduced even though the predicted absolute number density is below the experimental values. However, this quantitative mismatch should not be overrated taking the uncertainties of the LIF quantification into account. More important is that the declining concentration of OH· radicals downstream the gauze is another evidence for gas phase reactions. A noticeable qualitative disagreement is observed for H_2 where experimental and simulated profiles are nearly mirror images of each other. Whether this is an experimental artifact or a shortcoming of the microkinetic models cannot be concluded. To address the question whether the interaction between surface and gas phase chemistry is purely of thermal nature or also involves gas phase reactions triggered by radicals, e.g. OH· released from the platinum surface, further simulations were conducted. If gas phase chemistry alone is included in the model (plots not shown) no reactions are observed at gauze temperatures of 1300 K and 1500 K but full CH_4 conversion is observed at 1700 K. Hence the pure thermal light off temperature of gas phase reactions for the ϕ=0.5 stoichiometry used is between 1500 K and 1700 K. Figures 4.6 show the results for 1300 K, 1500 K and 1700 K gauze temperature if only surface reactions are included

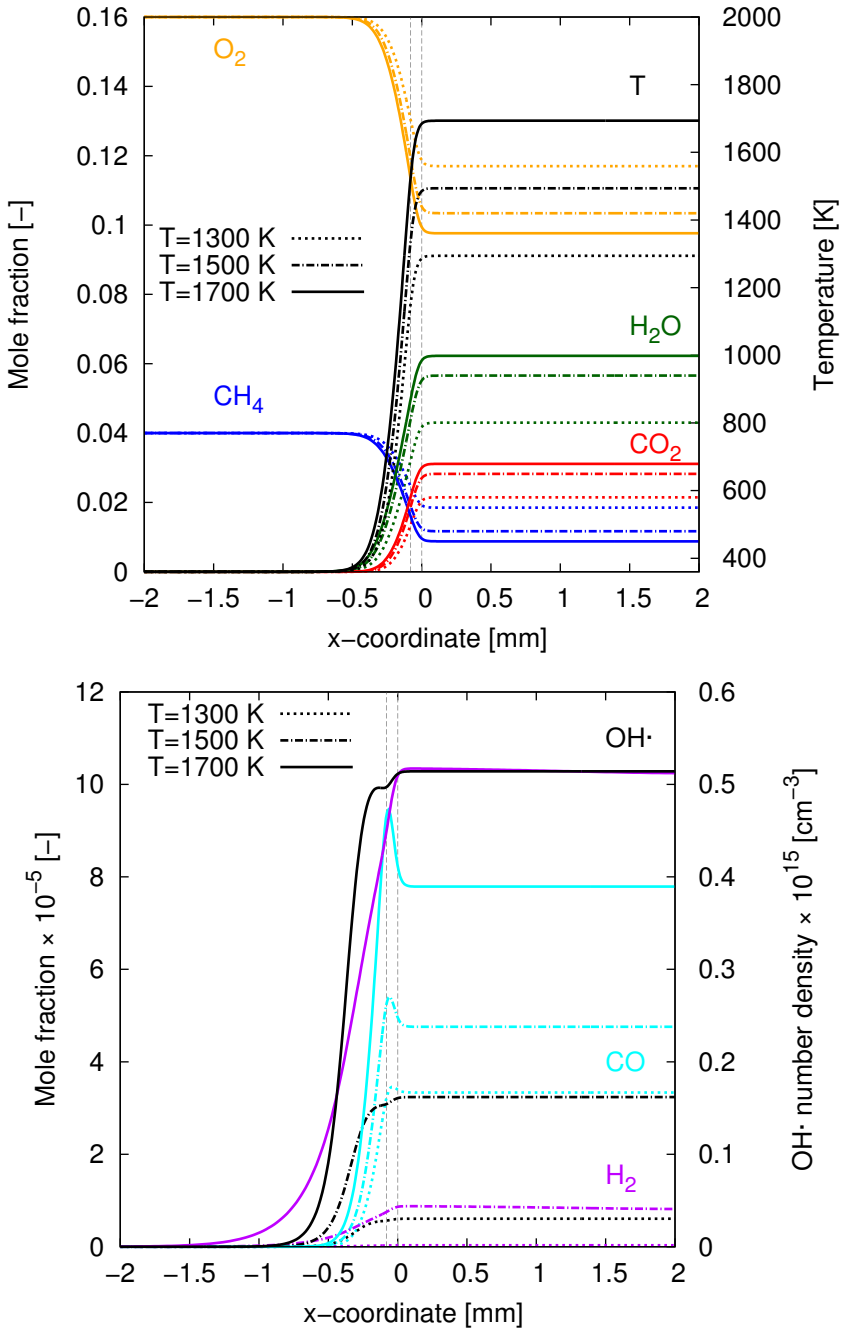

Figure 4.6: Influence of the gauze temperature on the simulated profiles if surface reactions are considered alone. Top: main species and temperature; bottom: minor species and OH· radical density.

in the model.

Even at a gauze temperature of 1700 K, CH_4 conversion is not complete after the gauze. The contact time with the gauze is simply too short. Furthermore, all species remain at constant concentration after the gauze and the gas stream takes on the temperature of the gauze. Taking these observations into account and considering also that full CH_4 conversion is reached at already at 1500 K gauze temperature if both gas and surface chemistry is included in the model, it can be concluded that radicals desorbing from the catalyst surface must play a role in the reaction network. The interaction of surface and gas phase chemistry cannot be of pure thermal nature. Reactive radicals such as OH· must desorb from the platinum surface and trigger radical chain reactions in the downstream section of the gauze, accounting for additional CH_4 conversion and product formation there. The numerically predicted decline of OH· radicals after the gauze which is also observed experimentally, directly shows the involvement of gas phase reactions.

4.4 Conclusions

With the spatial profile technique, it was possible to resolve the steep concentration gradients in the vicinity of a platinum gauze during catalytically assisted methane combustion. Quantitative OH· radical profiles could be measured by fiber-based Laser-Induced Fluorescence spectroscopy. By comparing these experimental data with numerical simulations including flow, mass and heat transport and microkinetic surface and gas phase chemistry, it is possible to show that the reaction occurs partly at the platinum surface and partly in the gas phase. The gradients upstream of the gauze are caused by diffusion while the gradients downstream of the gauze are a combined effect of diffusion and gas phase chemistry. It can further be concluded that the interaction between surface and gas phase chemistry is not limited to heat transfer only but also involves the desorption of surface-generated radicals which trigger gas phase chain reactions. As such, this chapter presents an example of coupled heterogeneous-homogeneous reactions in high temperature catalysis.

Microtomography-Based CFD Modeling of A Foam Monolith

5

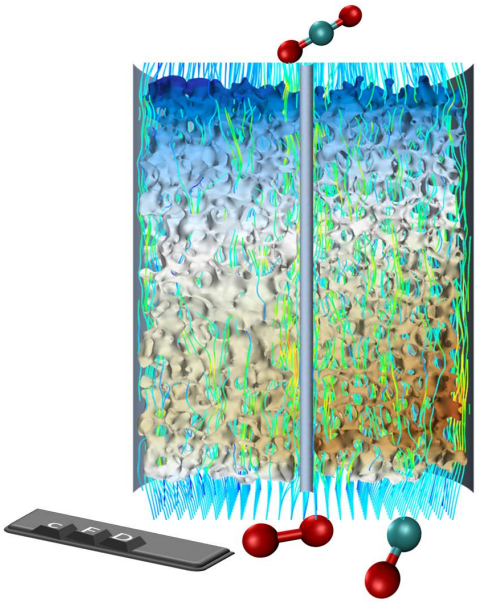

Foam monoliths made from mechanically stable, chemically inert and temperature resistant materials like refractory oxides, ceramics, silicon carbide or metals have attracted much interest as catalyst support in catalytic fixed-bed reactors. Due to their high porosity, foam monoliths generate low pressure drop even at high gas flow rates. High convection in the interconnected macro-pores enhances mass transfer, heat transfer and radial mixing [23, 178–180]. If the foam is made of materials of high thermal conductivity, heat transport in the struts of the irregular cell network increases which can be beneficial for exothermic reactions suffering from selectivity loss or hot-spot formation [181]. The intrinsic low specific surface area of foam supports can be increased by a washcoat carrying finely dispersed catalyst particles [182].

Strong modeling efforts have been made to understand the physical and chemical processes occuring inside fixed-bed reactors with foam monoliths [183, 184]. Much attention has been paid to hydrodynamics, heat transport inside the pore network [21, 22, 185] and heat transfer to the reactor wall [186, 187]. Heat and mass transport correlations have been derived from simulation data which can be applied for reactor design and development [182, 188–192].

In general, there are two approaches to model the foam structure. The unit cell approach [193] idealizes a foam monolith by periodic repetition of a representative unit cell in 3D space (e.g. Kelvin cells) [194]. The other approach is to simulate flow and transport using the foam geometry reconstructed from X-ray computed microtomography (μ-CT) scans [21, 22]. μ-CT is more costly, but it captures the irregular and randomized foam structure in high fidelity. μ-CT based CFD simulations deliver results closer to reality because the foam geometry in the model is the very same as that in the reactor.

This chapter is adopted from submitted manuscript: Y. Dong, O. Korup, J. Gerdts, R. Horn, Microtomography-based CFD modeling of a fixed-bed reactor with an open-cell foam monolith and experimental verification by reactor profile measurements. Submitted to Chemical Engineering Journal, 2018.

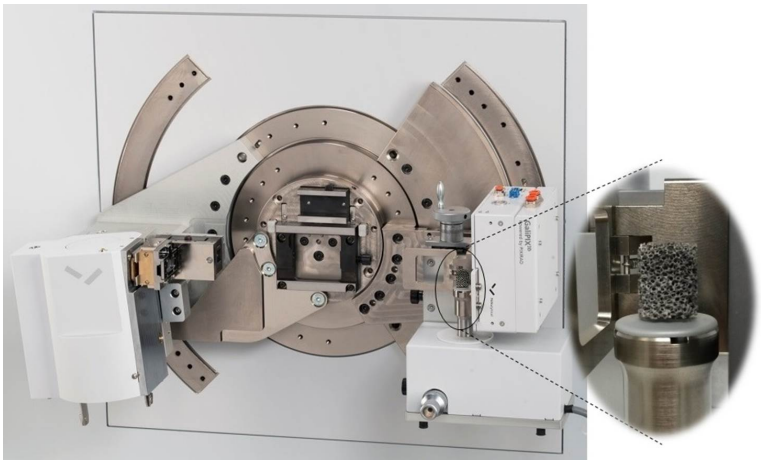

Figure 5.1: Photography of the PANalytical Empyrean interior: X-ray tube, sample holder (magnified) and GaliPIX^{3D} detector.

In order to gain confidence in μ-CT based CFD simulations, experimental validation is required. High resolution temperature and species concentration profiles measured through the centerline of foam catalysts offer currently the highest data point density for model validation [85, 195]. Spatial reactor measurements have also been used for validating CFD simulations of fixed-bed reactors with random packings of spherical [141] and non-spherical particles [27]. In those studies, the stochastic packing geometry is generated by DEM simulations. It represents the packing in the reactor within statistical bounds but it is not an exact copy of the bed inside the reactor.

If the packing geometry is reconstructed from μ-CT scans, as demonstrated in the present work for a foam monolith, the uncertainty in the bed structure is close to zero. Deviations between model and experiment are reduced to deficits in the kinetic model of the catalytic reaction, shortcomings in the description of momentum, mass and heat transport, inaccurate boundary conditions or erroneous experimental data.

In this work, we present, according to our knowledge for the first time, a comparison between temperature and concentration profiles measured through a foam catalyst under reaction conditions and μ-CT based CFD simulations of these data. We strive to keep uncertainties in the model as small as possible by choosing CO oxidation on Pt as a test reaction with well-known microkinetics, by using Pt nanoparticles with a narrow size distribution on a plain 45 ppi (pore per inch) α-Al_2O_3 foam monolith as simple catalyst system and by modeling transport processes and boundary conditions as accurately as possible including conjugated heat transport at the gas-surface interface and heat transport by radiation inside the foam. Deviations between the measured and simulated profiles are critically discussed in terms of having their origin in the experiment or in the model.

5.1 Experimental details

X-ray computed microtomography and reconstruction

The μ-CT system used in this work was the Empyrean research diffractometer from PANalytical [196]. Even though this instrument is normally used for X-ray diffraction, it can be operated as tomography setup. In this configuration, shown in Figure 5.1, the

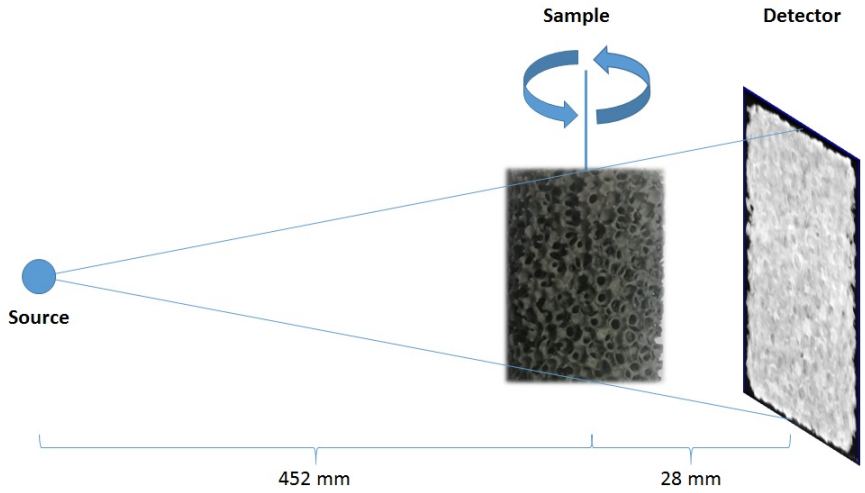

Figure 5.2: Illustration of the cone-beam μ-CT setup.

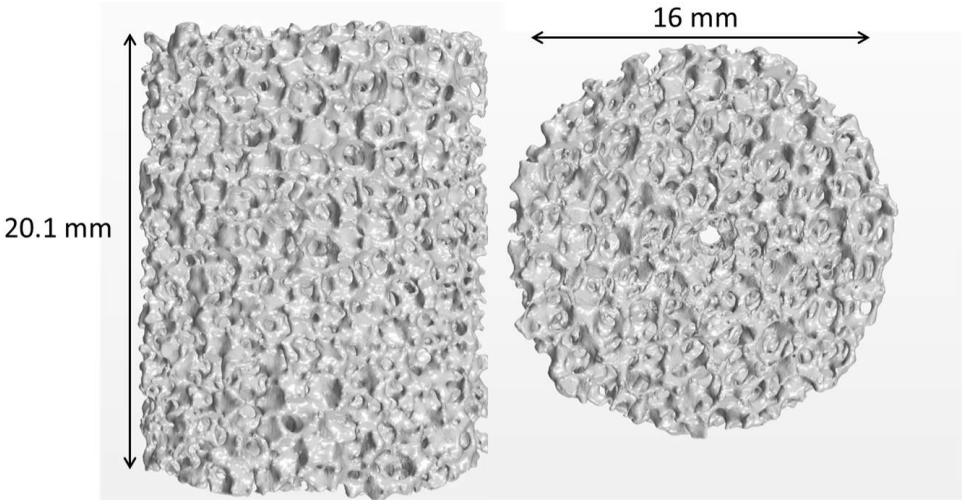

Figure 5.3: Side and top view of the CT reconstructed foam monolith.

X-ray tube is oriented line-of-sight to the detector ($2\theta = 0°$). A molybdenum tube was used because hard X-rays penetrate solid objects better than soft X-rays, e.g. from a copper tube. The tube was operated at 30 kV and 10 mA and a zirconium filter was used to remove the beta-line. The detector, the GaliPIX^{3D} from PANalytical, had a sensor area of 24.8 mm in width and 30.7 mm in height, pixel dimensions of 60×60 μm and was capable of detecting hard X-rays. The point focus of the X-ray tube was used with the X-rays being emitted in a cone like fashion from the Mo-anode. The catalyst foam was mounted on a rotatable sample platform 452 mm from the cone beam source and 28 mm from the detector (Figure 5.2) [88].

In a typical μ-CT-scan, the catalyst foam was rotated by 360 ° in steps of 0.2−2.0 ° and a measurement time of 0.5-2 s. After a flat field correction was performed on each X-ray transmission image, the 3D-structure of the foam was reconstructed in the software VGStudio MAX 2.2. Figure 5.3 shows side and top views of the reconstructed foam geometry. The channel in the center of the foam, seen in the view from top, accommodates the sampling capillary for the profile measurements [85, 195].

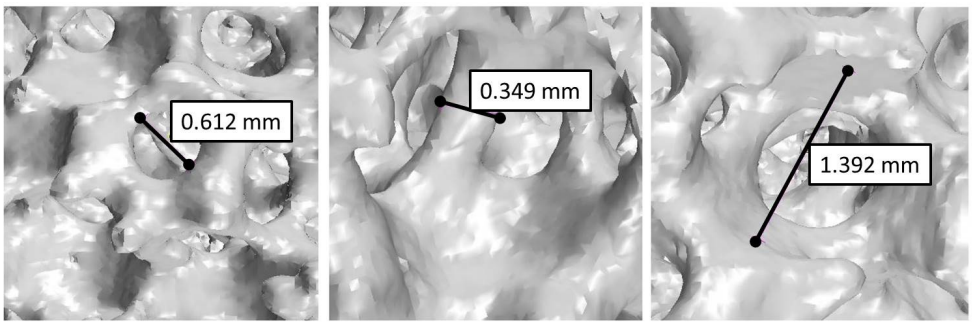

Figure 5.4: Image analysis to determine the average window size (left), bridge size (middle) and pore size (right).

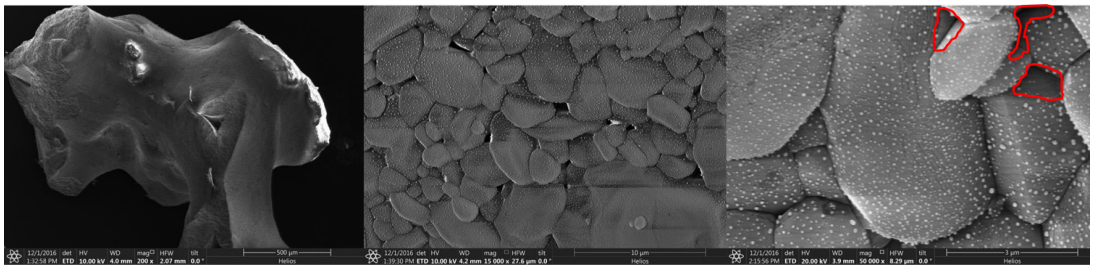

Figure 5.5: SEM images of the α-Al_2O_3 foam surface decorated with Pt nanoparticles at resolutions of 500 μm (left), 10 μm (middle) and 3 μm (right). The red encircled areas display a reduced density of Pt particles.

Characterization of the catalytic foam monolith

The pore-scale characterization of the 45 ppi α-Al_2O_3 foam monolith was carried out based on the CT-reconstructed surface as illustrated in Figure 5.4. Twenty representative pores and struts were analyzed to determine the average window size, pore size and bridge size. The results are summarized in Table 5.1. The total porosity was calculated from the solid volume of the foam monolith and the volume of a cylinder with same outer diameter and height as the foam (Figure. 5.3).

After all profile measurements on the foam were completed, it was removed from the reactor and a small part of the front edge was investigated by scanning electron microscopy (SEM)* using the FEI FIB Helios NanoLab G3. SEM images of different

Table 5.1: Morphological parameters of the investigated foam monolith. All parameters were evaluated from the CT-reconstructed surface.

Dimension Monolith (length/diameter)	20.1/16.0
Geometric surface area	1512 m^2/m^3
Pore size	1.35±0.09 mm
Bridge width	0.35±0.09 mm
Window size	0.65±0.09 mm
Porosity	0.73

*The SEM analysis was done by Dr. -Ing Martin Ritter from the Betriebseinheit Elektronenmikroskopie, TUHH

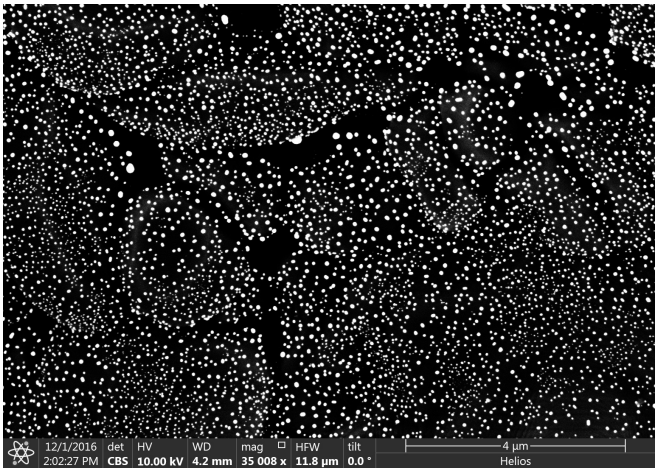

Figure 5.6: SEM image at 4 μm resolution after image processing. The white dots are the Pt particles, the α-Al_2O_3 crystals appear as black background.

resolutions are shown in Figure 5.5. The Pt nanoparticles are evenly distributed over the α-Al_2O_3 surface. Even though the reaction heated the foam catalyst to temperatures above 1500 K, no obvious sintering of the Pt nanoparticles was observed. As shown in Figure 5.6 and 5.7, the ratio of active Pt surface (A_{cat}) to the geometric surface of the foam (A_{geo}) was determined from a SEM image at a resolution of 4 μm. This ratio A_{cat}/A_{geo} is needed to incorporate the catalytic reactions as flux boundary condition in the CFD model by means of Eq. 3.65. In a first step the image analysis software ImageJ [197] was used to distinguish the Pt-particles from the α-Al_2O_3 crystals (Figure 5.6). The Pt particles were colored white, the α-Al_2O_3 crystals were colored black. From the processed image a size histogram was computed (Figure 5.7). The average particle diameter was determined to be 51 nm. It was assumed that all Pt nanoparticles were spherical and fully accessible. With this assumption a ratio $A_{cat}/A_{geo} = 0.4$ was obtained. This value is an upper bound because not all Pt atoms are accessible. The Pt atoms in contact with the alumina surface are not accessible for the catalytic reaction. Also crevices between the α-Al_2O_3 crystals (red encircled areas in Figure 5.5) seem to contain fewer Pt-particles than terraces accounted for in the image analysis. Therefore, the value of A_{cat}/A_{geo} was one of several model parameters that were investigated systematically in Section 5.3.

Profile measurement

The investigated Pt coated 45 ppi α-Al_2O_3 foam monolith was sandwiched between two inert, uncoated 80 ppi foam monoliths, wrapped in Interam^{TM} (3M^{TM}) and mounted in the fused silica reactor tube which had an inner diameter of 18 mm and an outer diameter of 38 mm (Figure 5.8). The two blank foams, each 12 mm long, reduced radiative heat losses from the catalyst foam. Gas flow was from bottom to top. Correspondingly and in agreement with earlier nomenclature, the blank foam below the catalyst was denoted as 'front heat shield (FHS)' and the blank foam above the catalyst as 'back heat shield (BHS)' respectively [198]. A channel of 1 mm diameter was drilled through the center of the foam stack in which a sampling capillary of 700 μm outer diameter and 530 μm inner diameter was inserted. The sampling capillary had a 100 μm side sampling orifice through which a gas sample could be extracted for gas chromatographic analysis. For measuring the catalyst temperature at the position of sampling, a thin pyrometer fiber was inserted into the sampling capillary and tip-

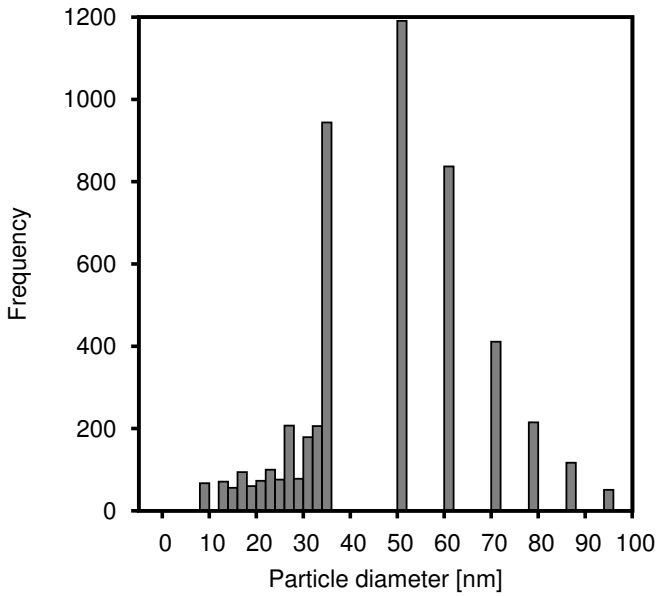

Figure 5.7: Particle size histogram computed from Figure 5.6.

Table 5.2: Meshing parameters used for simulating reactor packed with foam monolith. The extrusion mesh cells of the inlet and outlet are not counted in the cell counts.

Base size [mm]	Fluid cell counts	Solid cell counts
4	914248	299206
2	3630340	1230429
1	13352115	4252033

aligned with the sampling orifice. The tip of this fibre was polished to an angle of ≈ 30 ° collecting heat radiation from the catalyst and guiding it to a ratio pyrometer. The reactor tube was wrapped in Interam^{TM} limiting heat losses and providing for autothermal reactor operation. The reactor tube could be heated by a split furnace until catalyst light-off occurred. After light-off, the furnace was switched off and the catalyst operated autothermally.

Experiments were conducted with a stoichiometric CO/O_2 mixture diluted in Ar/He with the following mole fractions CO/O_2/Ar/He= 0.133/0.066 /0.736/0.065. A total inlet volumetric flow rate of 1200 mln/min (at 20 °C, 1 bar) was used. Profiles of gas phase species and catalyst temperature were measured by translating the assembly of sampling capillary/pyrometer fiber through the foam. A detailed description of the measuring process has been published earlier [198].

5.2 Simulation details

After reconstruction, the STL file of the reconstructed foam monolith surface shown in Figure 5.3 was imported into the CFD code STAR-CCM+ 11.04 [140]. The loaded tessellated surface was checked and repaired to obtain a continuous surface free of floating 'islands' due to the limited resolution of the CT scans. In the second step, the foam surface was meshed as shown in Figure 5.9. The simulation domain was created

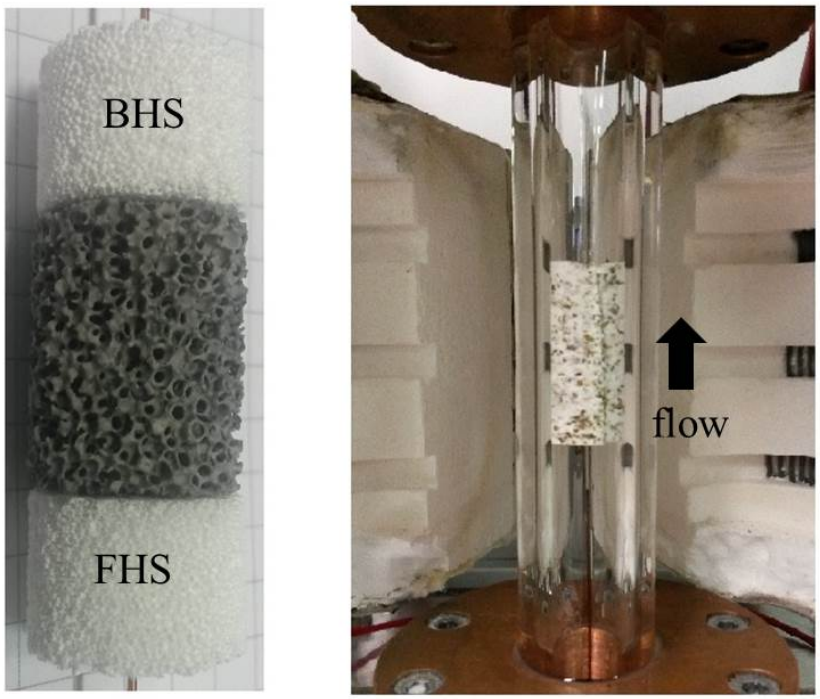

Figure 5.8: Left: Photography of the catalyst foam sandwiched between front heat shield below and back heat shield above. Right: Foam stack wrapped in Interam^{TM} inside the fused silica reactor tube.

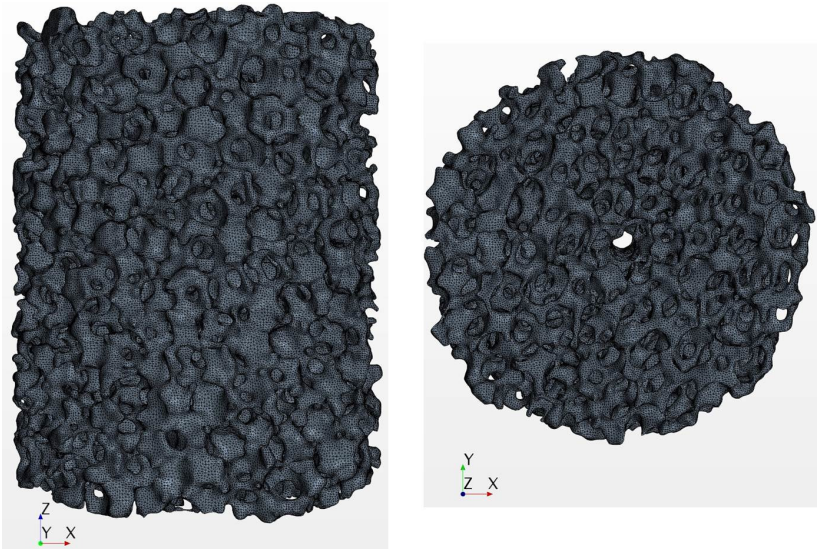

Figure 5.9: Foam monolith with meshed surface: side view (left) and top view (right).

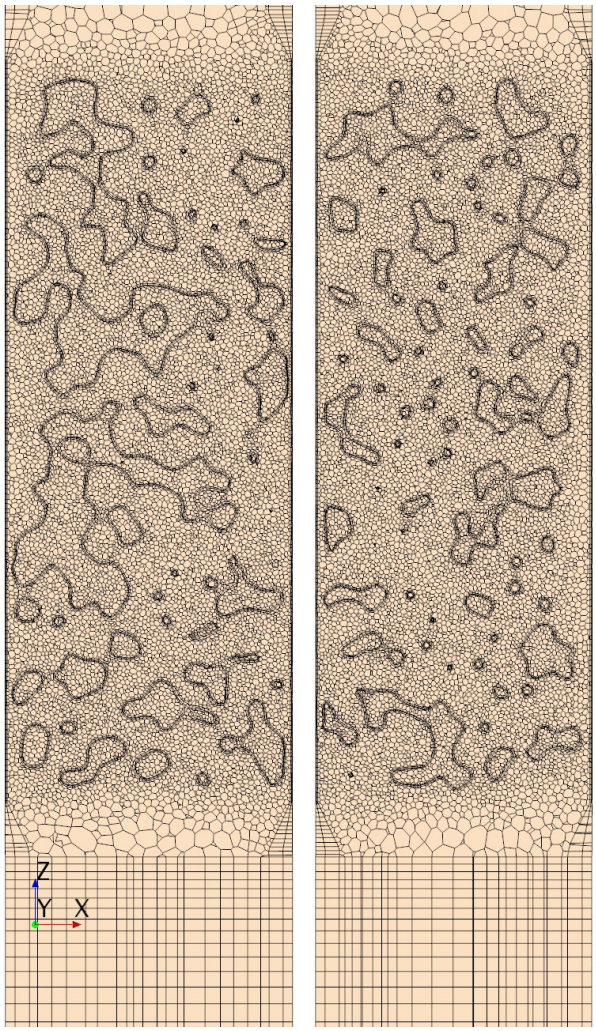

Figure 5.10: Translational plan section plot of the volume mesh.

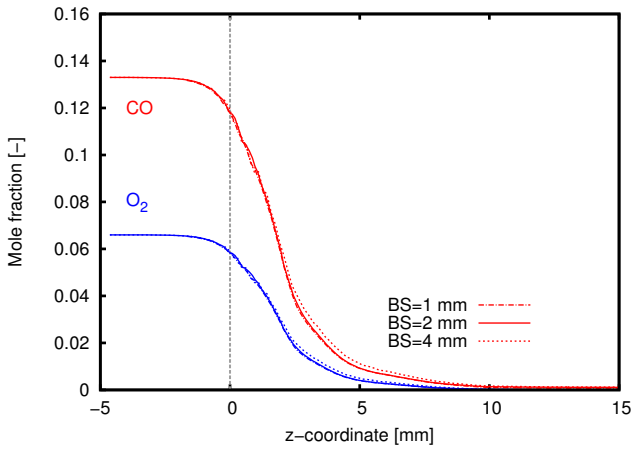

Figure 5.11: Simulated concentration profiles of CO oxidation on at different base size of the volume mesh.

by inserting the foam monolith into a cylindrical container representing the reactor tube and by placing a thin cylinder in the center hole simulating the sampling capillary. To keep computational time within bounds, only the catalyst foam was considered in the model. Front and back heat shield were indirectly considered in form of inlet and outlet boundary conditions but their geometry was not resolved in the CFD model. The simulation domain was then volume meshed (Figure 5.10). The mesh strategy was the same as in a previous paper by the authors [27]. Both, fluid and solid domain were meshed with a polyhedral mesh while two layers of prism meshes were applied to all surfaces (foam surface, capillary wall and reactor tube wall). Inlet and outlet surfaces were extended with a structured cuboid mesh to avoid back flow effects. Mesh parameters were set as percentage of the base size and mesh convergence was checked by reducing the base size until the simulated concentration profiles converged (Figure 5.11). Mesh independence was reached at a base size of 2 mm and all simulations discussed below were done with this base size.

The CFD simulations were set up to mimic the experimental profile measurements as closely as possible. Laminar flow ($Re \approx 10$), conjugated heat transfer between fluid and catalyst foam, CO oxidation on the foam surface and radiation were included and solved in STAR-CCM+ 11.04 [140]. Gravitational and external forces, thermal diffusion and viscous heating were not considered [148]. Uniform inlet velocity, temperature and gas composition were assumed as inlet boundary conditions. A pressure outlet boundary condition was used at the upper end of the computational domain. No-slip boundary conditions were assigned to all solid walls (foam surface, capillary wall, reactor tube wall). The capillary wall was set as adiabatic. Apart from few simulations where heat losses through the wall were considered the reactor wall was also considered adiabatic. All simulations were carried out at steady state and the corresponding governing equations are given in Chapter 3.

In this work, a mechanism from Deutschmann et al. [175] was used for describing CO oxidation on Pt. The reactions and the kinetic parameters are given in Table 5.3. The mechanism was imported into STAR-CCM+ 11.04 [140] as CHEMKIN files and the build-in stiff solver DARS was used for handling the microkinetics. In order to improve efficiency, the operator splitting algorithm was used which decouples the transport equations and the chemical reactions [176].

Due to the high reaction temperature, thermal radiation was also considered by employing the surface-to-surface (S2S) radiation model in STAR-CCM+ [140]. This brings a radiant flux q'_{rad} in W/m^2 in the energy equation source term at the solid boundaries. The gas phase between solid surfaces is non-participating (no absorption, emission, or scattering of thermal radiation). Radiation properties were treated as wavelength independent and the emissivity of the foam, the capillary and the reactor surface were set to 0.9 [199]. At first, STAR-CCM+ [140] calculates view factors by ray tracing for each pair of surface patches (discretized boundary surfaces). View factors are defined as 'fraction of uniform diffuse radiation leaving a surface that directly reaches another surface' [200]. From the view factors radiosity and irradiation fields are calculated on all surfaces. More details on the S2S radiation model can be found in the user guide of STAR-CCM+ [140] or in the work of Wehinger et al. [141].

Table 5.3: Surface reaction steps and rate parameters of CO oxidation on Pt used in this work. The mechanism is adopted from Deutschmann mechanism of CH_4 oxidation on Pt [175, 201, 202].

Reaction	Pre-exponential factor [a]	Temperature exponent, β	Activation energy [kJ/mol]
O_2 + 2 Pt(s) → 2 O(s)	0.023 [b]	0	0
2 O(s) → O_2 + 2 Pt(s)	$3.70 \cdot 10^{21}$	0	213.2-60 $\cdot\theta_{O(s)}$
CO + Pt(s) → CO(s) [c]	$1.618 \cdot 10^{20}$	0.5	0
CO(s) → CO + Pt(s)	$1.0 \cdot 10^{13}$	0	125.5
CO(s) + O(s) → CO_2 (s) + Pt(s)	$3.70 \cdot 10^{21}$	0	105
CO_2 + Pt(s) → CO_2 (s)	$5.0 \cdot 10^{-3}$ [b]	0	0
CO_2 (s) → CO_2 + Pt(s)	$1.0 \cdot 10^{13}$	0	20.5
C(s) + O(s) → CO(s) + Pt(s)	$3.70 \cdot 10^{21}$	0	62.8
CO(s) + Pt(s) → C(s) + O(s)	$1.0 \cdot 10^{18}$	0	184

[a] pre-exponential factor in units of [cm, mol, s]
[b] sticking coefficient [dimensionless]
[c] reaction order of Pt(s) is 2 for this step.
surface site density $\Gamma = 2.72 \cdot 10^{-9}$ mol/cm^2

5.3 Results and discussion

Figure 5.12 displays plots of the simulated pressure, velocity, temperature and concentration fields of CO, O_2 and CO_2 inside the foam. At the low flow rates used in the current study, the pressure drop along the foam is just a few Pascal. There is basically no radial pressure gradient. The flow field is very inhomogeneous with almost stagnant flow in windows, in the wake of struts and fast flow in the main channels, close to the wall and in the vicinity of the sampling capillary. Similar results were obtained for non-reacting flows by Fan et al. [21].

The temperature field is also very inhomogeneous but much more difficult to rationalize than the flow field. When the reactant mixture reaches the front of the foam, the gas temperature rises steeply. The reaction rate in the entrance region of the foam is high because CO and O_2 have their highest concentration there and the liberated heat increases temperature and reaction rate even further. Interesting and eye-catching however is the hot-spot that can be seen in the temperature plot of Figure 5.12, a few mm inside the foam close to the wall on the right side. This hot-spot forms because the geometry of the foam there is accidentally such that some unconverted O_2 and CO can channel a few millimeters into the foam. In consequence a gas stream with still rather high concentration of O_2 and CO hits a catalyst that is significantly hotter than the catalyst at the front face of the foam. Because the reaction rate depends more sensitively on temperature than on concentration, a very high reaction rate results in a spatially confined area leading to a hot-spot. On the left side of the temperature plot of Figure 5.12 no hot-spot is seen because there is no reactant channeling. This shows how complex the interplay between flow, heat generation and heat transport is and how subtle differences in geometry and flow velocity lead to pronounced non-uniformity in reaction rate and catalyst temperature. This challenges the unit cell approach because a regular foam structure would lead to a regular flow and temperature pattern which is not observed in reality.

With decreasing reactant concentration the reaction rate and the rate of heat production decrease and become zero once the reactants are fully consumed. Due to radiative heat losses at the back face of the foam and axial heat transport by conduction, convection and radiation, the temperature decreases in flow direction. Temperature gradients in radial direction smoothen out once the reaction comes to hold because of the adiabatic boundary condition at the reactor wall.

As mentioned in Section 5.1, an initial A_{cat}/A_{geo} ratio of 0.4 was determined from the SEM image in Figure 5.6 under the assumption that all Pt particles were spherical and fully accessible. In reality the particles wet the α-Al_2O_3 support partly which results in a lower A_{cat}/A_{geo} ratio. Also the SEM image in Figure 5.6 might not be representative of the entire foam because it was taken at the rather cold front edge of the used foam. In hot areas inside the foam, Pt sintering or even Pt losses could have occurred, e.g. by vaporization of PtO_2. Hence the A_{cat}/A_{geo} ratio is a parameter in the simulation and the value of 0.4 can merely be considered as a starting value. Figure 5.13 shows a screening study of this parameter in a range from 1 to 0.01 by comparing the experimental and simulated CO profile.

As can be expected, the A_{cat}/A_{geo} ratio influences the slope of the profiles. The higher the value, the faster CO is consumed. The decreasing CO concentration in front of the catalyst foam at $z < 0\ mm$ is due to diffusion. Gas phase chemistry was not considered in the model. Best agreement was found for a value $A_{cat}/A_{geo} = 0.03$. This value is much lower than the initial estimate of 0.4. Whether this is due to wetting of the Pt particles or Pt losses or whether this is due to erroneous kinetic parameters cannot be inferred from the present data. Other experimental methods like H_2 or CO

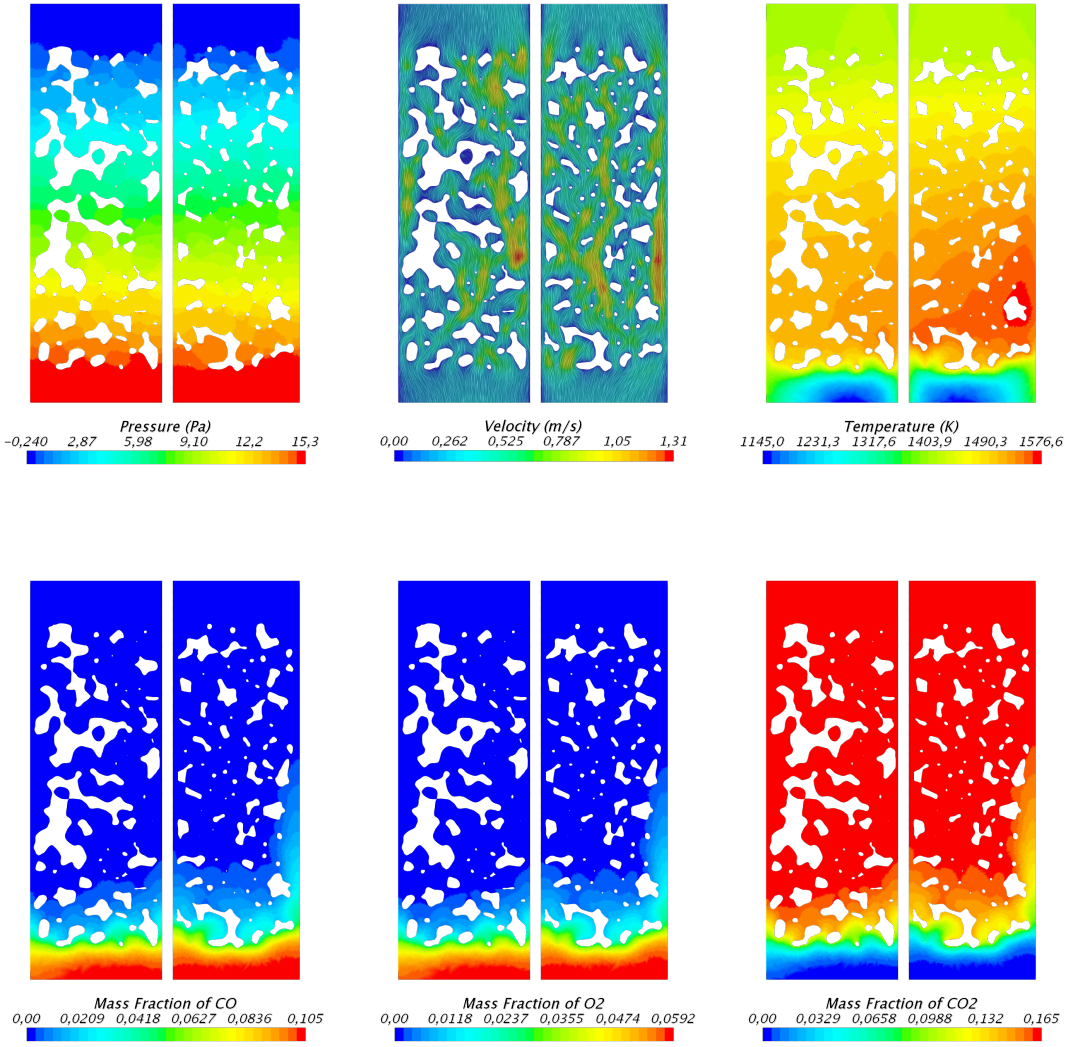

Figure 5.12: Translational cut plane plots of the simulated relative pressure (top left), velocity (top middle), gas phase temperature (top right), mass fraction of CO (bottom left), O_2 (bottom middle) and CO_2 (bottom right).

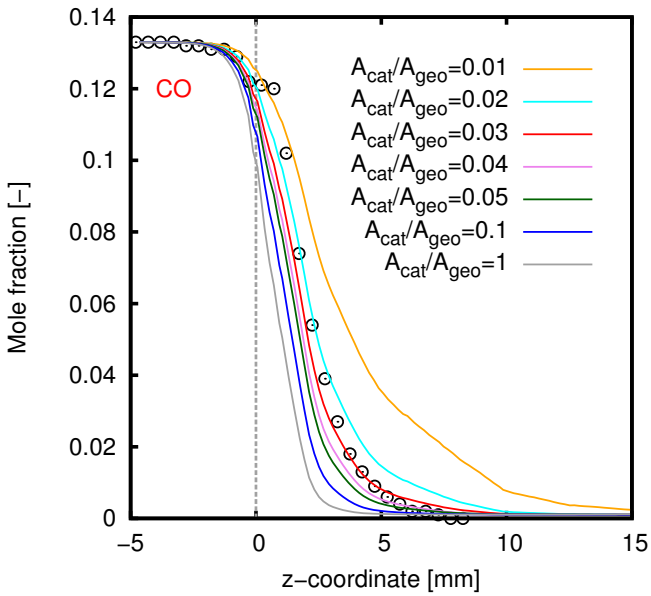

Figure 5.13: Effect of the A_{cat}/A_{geo} ratio on the simulated CO profiles.

chemisorption could be used to determine this value more accurately but the entire foam did not fit into any available sample cell and destruction of the foam would have created additional Al_2O_3 surface biasing the true value. Hence the best fit value of $A_{cat}/A_{geo} = 0.03$ was used in all simulations that follow hereafter.

A comparison of the simulated and measured species and temperature profiles is displayed in Figure 5.14. The catalytic foam monolith starts at z=0 mm as indicated by the vertical grey dotted line. The overall agreement between the simulated and measured species profiles is very good. The experimentally observed rapid conversion of CO and O_2 reaching full conversion at about z=8 mm is confirmed by the model. Similar good agreement is found for CO_2. The observed local deviations between the simulated profiles and the measured data points are due to the fact that the simulated trajectory is in all likelihood not the same as the scan line along which the sampling orifice was translated through the foam. Both the measured and simulated species profiles depend sensitively on the pore structure along the probed trajectory. In the current study the experimental scan line was chosen arbitrarily and local deviations are the natural consequence. The easiest and fastest way to illustrate this is by plotting simulation trajectories at the same radial coordinate but different azimuthal angles. Figure 5.15 shows four simulated CO trajectories at 0, $\pi/2$, π and $3/2\pi$ azimuthal angle at the outer wall of the sampling capillary. While the overall shape of the CO profiles is similar, pore structure effects lead to local deviations.

While such random deviations can be minimized by averaging a high number of simulated and measured trajectories, the simulated and measured temperature profiles in Figure 5.14 are systematically different. The temperature profile measured with the pyrometer fiber inside the sampling capillary increases slowly in the front heat shield from 1502 K at z=-5 mm to a maximum of 1544 K at the entrance of the catalyst foam (z=0 mm) and falls then steeply to 1005 K at the end of the catalyst foam (z=20 mm). Because the simulation domain did not include the heat shields, the simulated temperature profile starts at the entrance of the catalyst foam (z=0 mm) at 1490 K and rises to 1562 K at z=2.5 mm. The simulated temperature maximum coincides with the inflection point in the measured and simulated CO and O_2 profiles.

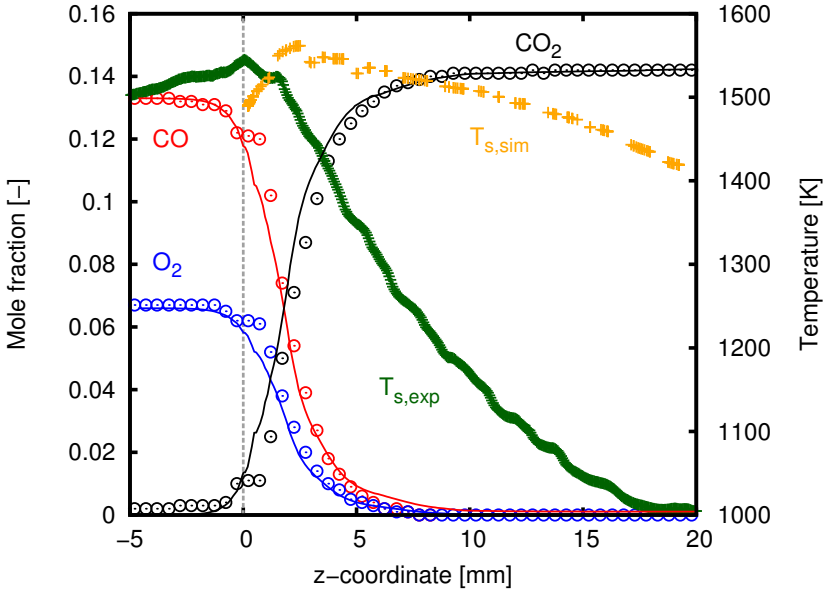

Figure 5.14: Comparison of the simulated (lines) and measured (dots) species profiles and solid surface temperature profiles of CO oxidation on Pt loaded α-Al_2O_3 foam monolith. The grey dotted line marks the inlet of the catalyst foam.

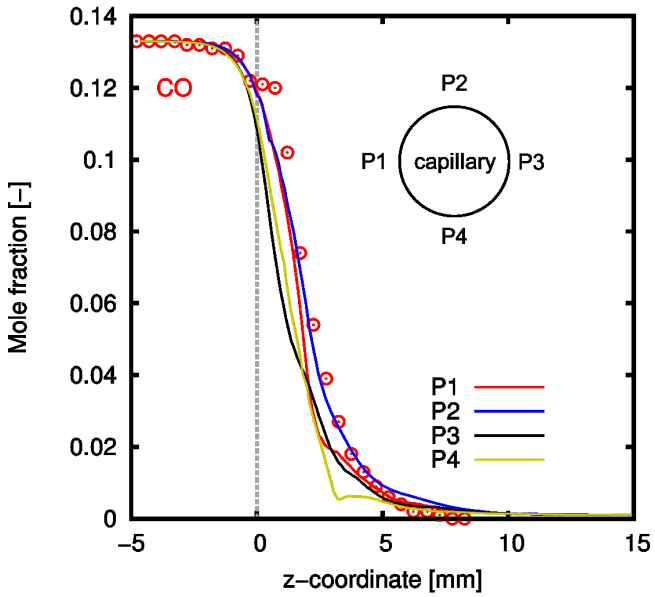

Figure 5.15: Effect of the local pore structure on the simulated species profiles. The lines P1, P2, P3, P4 are four trajectories taken at 0, $\pi/2$, π and $3/2\pi$ azimuthal angle at the same radial coordinate corresponding to the outer wall of the sampling capillary.

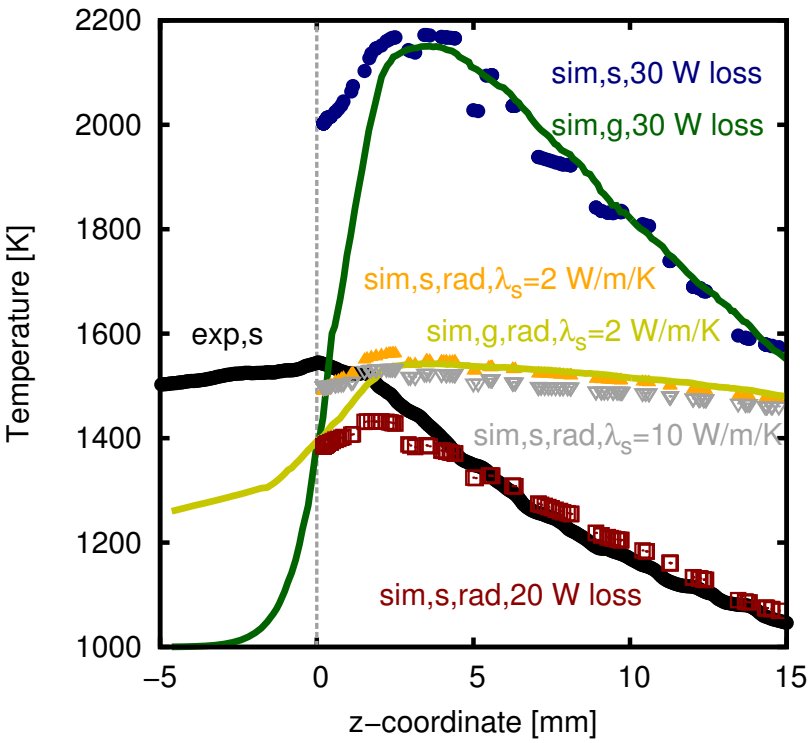

Figure 5.16: Effects of the different heat transport phenomenon (radiation, heat loss through the reactor wall, thermal conductivity of the solid material) on the simulated solid surface temperature.

Therefore, the position of the simulated temperature maximum is correct. While the measured and simulated maximum temperature values are close (1544 K vs. 1562 K respectively), it is physically impossible, that the temperature maximum occurs right at the entrance of the catalyst foam because the catalytic reaction is the only heat source and the maximum temperature occurs at the position of highest reaction rate. The measured temperature maximum at the entrance of the catalyst foam is therefore an experimental artifact. The fused silica fiber that is used to collect thermal radiation and guide it to the pyrometer has a rather flat acceptance angle and looks ahead, in this case about 2.5 mm. This 'looking ahead' phenomenon is well known and was experimentally and mathematically quantified in earlier publications [198, 203].

Not only the positions of the temperature maxima deviate significantly between experiment and simulation, the slopes before and after the temperature maximum are also quite different. Both, the simulated and the measured temperature profiles in Figure 5.14 decrease after the maximum until the end of the foam. This indicates heat losses. In a truly adiabatic reactor, the temperature would remain constant if heat release by exothermic chemistry ceases. In the model, as described in Section 5.2, the only heat losses occur by radiation at the front and back face of the catalyst foam. Because the front heat shield was neglected in the simulation to keep the computation manageable, the radiative boundary in the model is closer to the temperature maximum than in the experiment and hence the slope of the simulated temperature profile to the left of the maximum is steeper than that of the measured one. This is observed and according to expectations. To the right of the maximum the temperature in the simulated profile decreases less steeply than in the measurement even though the radiative boundary condition in the model is also closer due to the lacking heat

shield. This indicates that either the thermal conductivity of the foam material used in the model is too low or that the adiabatic boundary condition at the reactor wall is not correct.

To investigate these options, heat transport parameters and thermal boundary conditions were varied in the model and the simulation results were compared with the experimental temperature profile. Figure 5.16 summarizes the results. Increasing the thermal conductivity of the foam from $\lambda_{solid} = 2$ W/m/K (orange triangles) to $\lambda_{solid} =$ 10 W/m/K (grey triangles) has only a small effect on the simulated temperature profile. The temperature maximum and the slopes go down slightly. This shows that axial heat conduction in the struts of the foam play a minor role for heat transport. However, if a heat loss is applied to the reactor wall in the model, it has a strong influence on the simulated temperature profile. The temperature maximum goes down and the slopes before and after the maximum become steeper. A heat loss of 20 W at the wall (brown squares in Figure. 5.16) gives almost perfect agreement in terms of slope after the maximum but then the temperature maximum itself falls below the experimental value. If an attempt is made to bring the temperature maximum back up by turning off radiation losses at the front and back face of the catalyst foam, a temperature profile far above the measured one results. Even with 30 W heat losses at the wall, a temperature maximum of almost 2200 K is predicted if radiation losses are neglected (blue dots Figure 5.16).

The simulation results in Figure 5.16 show how difficult it is to capture the correct temperature profile in the foam at these high temperatures. Heat losses by radiation are very important but cannot be properly implemented in the model because the computational costs to also include the heat shields in the modeling domain are currently still too high. A shortcoming of the experiment is the ill-defined thermal boundary condition at the wall of the reactor tube. Because the reactor wall was wrapped by insulation material it was initially considered adiabatic in the model but the simulation results in Figure 5.16 show that there must be wall heat losses on the size of 20 W having a distinct impact on the slope of the temperature profile. Expansion of the modeling domain to include the heat shields and a more accurate definition of the thermal boundary conditions in the experiment will be necessary to bring the simulated and the experimental temperature profile in agreement.

The last question that will be addressed in this work is how it is possible that measured and simulated species profiles agree within statistical bounds while the measured and simulated temperature profiles are distinctly different. Two ideas come to mind which are i) the reaction is film transport limited and hence not very sensitive to the underlying kinetics and ii) the reaction is kinetically controlled but the rate limiting step is insensitive to temperature. It will be shown in the following that both effects are operational. The presence of film transport limitations can already be seen in Figure 5.16 which compares simulated gas and solid temperature profiles for the cases radiation + adiabatic wall and no radiation + 30 W losses at the wall (yellow line vs. orange triangles and green line vs. blue dots respectively). Because heat production by the exothermic surface reaction is initially much faster than heat transport to the gas phase, the solid temperature at the entrance of the foam (z=0 mm) is significantly higher than the gas temperature. By going into the foam, the gas temperature approaches that of the solid and from about 3 mm on they fall on top of each other.

If heat transport limitations are present mass transport limitations can be expected as well. Figure 5.17 shows a comparison of the surface concentration of CO, O_2 and CO_2 to their bulk gas phase concentration values. Due to the large pores of the foam the surface concentration values have some discontinuities but it can be clearly seen that in the first 3 mm of the foam the surface concentration values of the reactants CO

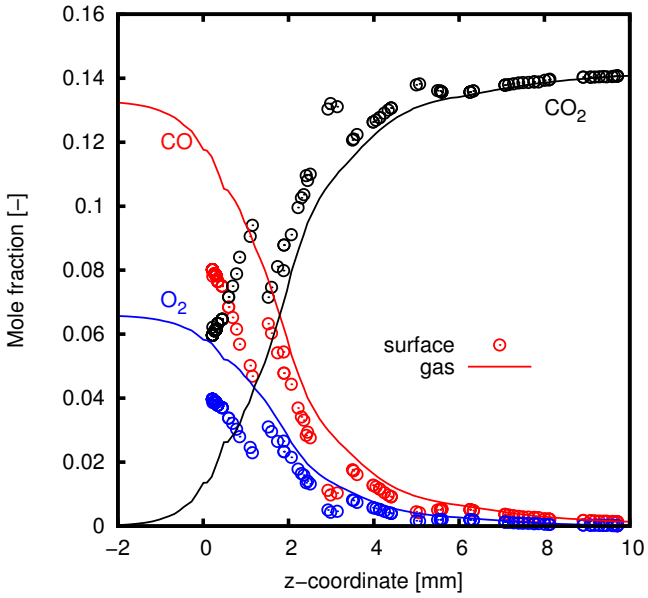

Figure 5.17: Comparison of the species profiles in the gas phase and on the nearest solid surface.

Table 5.4: Surface and gas compositions extracted from simulations at z-coordinate of 2 mm.

$\theta_{CO(s)}$	0.022	[-]
$\theta_{CO_2(s)}$	$1.11 \cdot 10^{-7}$	[-]
$\theta_{O(s)}$	0.0035	[-]
$\theta_{C(s)}$	$6.27 \cdot 10^{-8}$	[-]
$\theta_{Pt(s)}$	0.9745	[-]
c_{CO}	0.375	$\text{mol} \cdot \text{m}^{-3}$
c_{CO_2}	2.288	$\text{mol} \cdot \text{m}^{-3}$
c_{O_2}	0.178	$\text{mol} \cdot \text{m}^{-3}$

and O_2 are much lower and that of CO_2 much higher than their gas phase counterparts. This different concentration values show that diffusion to or from the surface limits the reaction rate to some extent but not fully. In the latter case the surface concentration of CO and O_2 would be zero. Still, the influence of diffusion reduces the temperature sensitivity of the reaction rate because the diffusion coefficient of a molecule in the gas phase is only a weak function of temperature ($D \sim T^{1.5}$).

To identify the rate limiting step in the catalytic cycle given in Table 5.3, a graphical method suggested by M. A. Vannice was applied [204]. At first, surface site fractions of all species as well as gas phase concentrations were extracted from the simulation results at a position close to the maximum reaction rate (z=2 mm). The numerical values are listed in Table 5.4. With this concentration values the local reaction rates of all elementary steps in the microkinetic network were calculated. Figure 5.18 shows a plot of these reaction rates divided by their stoichiometric numbers on a logarithmic scale. The lowest net rate is that of O_2 adsorption which equals the rate of the surface reaction step because the latter is irreversible. The CO adsorption step

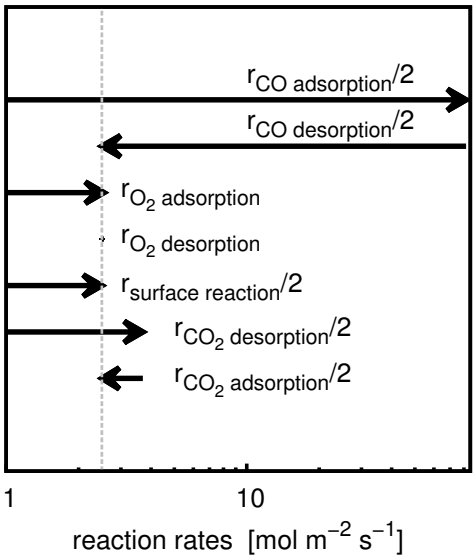

Figure 5.18: Analysis of the rate limiting step in a reaction sequence by plotting stoichiometry normalized reaction rates computed from the concentration values listed in Table 5.4.

and CO_2 desorption step are much faster and kinetically irrelevant. To distinguish whether the O_2 adsorption step or the surface reaction step is rate limiting species profiles were calculated for increasing O_2 sticking coefficients and for increasing pre-exponential factors of the surface reaction step. Figure 5.19 summarizes the results.

If the sticking coefficient of O_2 is increased, as shown in the upper plot of Figure 5.19, the profiles become steeper. If the pre-exponential factor of the surface reaction step is increased, as shown in the lower plot of Figure 5.19, the profiles do not change. This clearly shows that the adsorption of O_2 on the Pt catalyst is the rate limiting step under the high temperature reaction conditions encountered in the foam. That O_2 adsorption is rate limiting can also be seen by plotting surface site fractions of the most abundant surface species Pt(s) and CO(s) on the foam surface (Figure. 5.20). The surface is basically empty. Almost all Pt sites are free because any adsorbing molecules CO and O_2 molecules react immediately to CO_2 which desorbs. Only in a small strip right at the foam inlet where the catalyst surface is convectively cooled by the incoming gases can a measurable CO(s) coverage exist ($\sim 7\,\%$).

With this analysis it becomes clear why the simulated species profiles can fit nicely to the measured species profiles while the simulated temperature profile is quite different from the measured one. On the one hand the reaction rate is influenced by film diffusion which reduces the temperature sensitivity already. On the other hand and more importantly the non-activated O_2 adsorption is rate limiting and the only temperature dependence of this step is given by Equation 3.70 ($\sim T^{0.5}$) and hence even lower than that of diffusion.

5.4 Conclusions

CFD simulations of catalytic reactors become more and more popular because they are in many aspects superior to conventional pseudo-homogeneous and heterogeneous

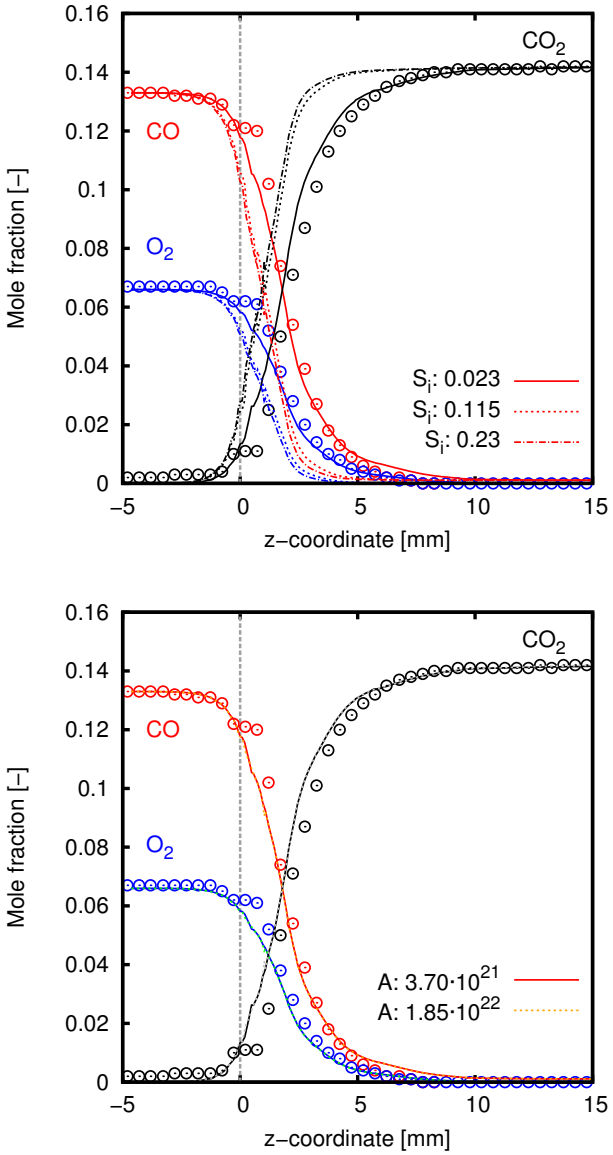

Figure 5.19: Top: Variation of the O_2 sticking coefficient (S_i) shows that O_2 adsorption is the rate limiting step for CO oxidation on Pt at the high temperature conditions of this study. Bottom: Variation of the pre-exponential factor (A) of the surface reaction step CO(s) + O(s) → CO_2(s) + Pt(s) has no effect on the simulated profiles. This step is fast and kinetically irrelevant at the conditions of this study.

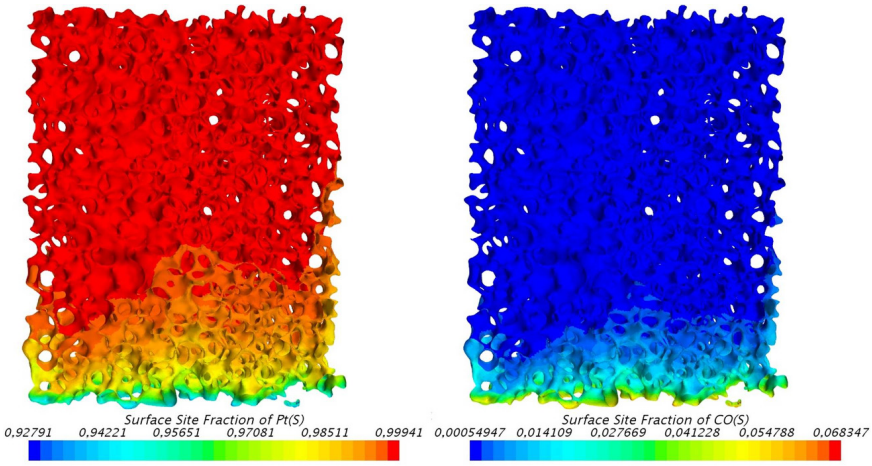

Figure 5.20: Illustration of the surface site fraction of the Pt sites (left) and adsorbed CO(s) species (right).

reactor models. They produce 2D or even 3D concentration-, flow- and temperature fields which are almost impossible to measure. If coupled with microkinetic reaction models CFD simulations even allow computing 3D pictures of surface coverages. Measurements are often restricted to what flows into the reactor and what comes out of it ('in-out' data). What happens inside the reactor remains hidden. CFD simulations of catalytic reactors can provide this much-wanted insight but the question is how realistic the simulation data are and how to validate them against experiments.

The present work is a critical comparison between CFD simulation results and sub-millimeter resolved species and temperature profiles measured through a catalytic foam monolith. Profile data have a much higher information content than conventional 'in-out' data and are therefore a much more stringent touchstone for model validation. CO oxidation on Pt nanoparticles with narrow size distribution supported on an α-Al_2O_3 foam was chosen as simple catalytic system with well known microkinetics. To keep uncertainties in the CFD geometry as small as possible, the structure of the foam catalyst was resolved by X-ray microtomography. Simulation parameters and boundary conditions were determined as accurately as possible. To validate the simulation results, concentration and temperature profiles were measured in a dedicated reactor setup on the very same foam of which the geometry was determined by X-ray tomography. To the best of our knowledge, it is the first time that such a comparison is made. It allows a critical assessment of strengths and weaknesses of both, the model and the experiment and can serve as basis for a knowledge based design of processes employing catalytic foams or similar random geometries.

The simulations reveal very inhomogeneous flow, temperature and concentration fields inside the foam due to the random nature of the foam structure and the complex interplay between flow, heat transport and heterogeneous chemistry. These local inhomogeneities challenge the accuracy of the unit cell approach for simulating catalytic foams which assume a regular structure. μ-CT based CFD simulations are therefore more realistic but of course much more expensive and restricted to rather small samples. By varying the A_{cat}/A_{geo} ratio, a parameter describing the density of Pt sites on the foam catalyst, the simulated and measured species profiles could be brought in close agreement while the simulated and measured catalyst temperature profiles could not. This at first contradicting result could be rationalized by showing that the reaction rate is partly controlled by film diffusion and kinetically limited by O_2 adsorption.

Both steps are rather insensitive to the catalyst temperature. An A_{cat}/A_{geo} ratio of 0.03 described the measured species profiles best. This value is much lower than the value of 0.4 determined by SEM image analysis implying that either the sticking coefficient of O_2 is too high in the kinetic model or that the Pt site density is lower than suggested by SEM image analysis. The latter could be due to the non-accessibility of the Pt atoms in contact with the α-Al_2O_3 support, platinum losses under reaction conditions or a reduced particle density in cracks and kinks of the support not captured by SEM image analysis.

To rationalize the mismatch between simulated and measured catalyst temperature the contribution of heat transport by conduction and radiation and the occurrence of heat losses through the reactor wall were explored in a series of simulations. While heat transport by conduction in the struts of the foam is negligible, radiation and heat losses through the reactor wall have a strong influence on the temperature profile. Neglecting radiation in the model leads to unreasonably high temperatures in the foam, way above what is measured. Considering radiative heat transport and radiative losses at the front and back face of the foam brings the temperature maximum down to what is measured but the slopes of the measured and simulated catalyst temperature profiles differ still substantially. Heat losses through the reactor wall are one cause of that. Despite thick insulation of the reactor tube about 20 W of heat are lost through the wall and the initial assumption of an adiabatic wall turned out to be incorrect. The other cause for the mismatch between simulated and measured catalyst temperature profiles are the missing heat shields in the model. With the computer hardware available it was simply not feasible to include them in the computational domain.

In summary it can be said that CFD simulations provide detailed insight into the chemical and physical processes inside catalytic reactors. No experimental method can provide comparable data. However, simulation results are only as good as the model from which they are produced and many parameters and boundary conditions must be specified in this type of simulations to obtain meaningful results. This requires sometimes to extent the computational domain beyond the frontiers of the possible. However computational power is every increasing and it is only a matter of time before CFD simulations will become the standard design tool in catalytic reaction engineering.

Packing Study: DEM Simulations and Validations

6

Fixed-bed reactors are typically packed by dropping particles in a random fashion. Due to the stochastic nature of the random packing process, duplicating experimental packing by computer model is not possible. Instead, a statistical representation by applying Discrete Element Method (DEM) has gain much attention since it offer a cost-effective way to mimic the experimental packing process closely [61].

In this work, random packings of both spherical and Raschig ring types of packing in fixed-bed reactors were modeled in the commercial software STAR-CCM+ [140]. Figure 6.1 illustrates a typical DEM simulation work flow. Particles were injected from the top of the reactor with randomized angular velocity and orientation and fall due to gravity. In order to accelerate the falling process, an initial velocity of 1 m/s was applied to the particles. Particles may collide with each other and the wall and settle layer by layer. Constant particle flow is injected to the reactor until the pre-set maximum number is reached. The packing generation was finished when all the particles were resting which means all the particles had a nearly zero velocity. In order to gain confidence of the DEM predictions for fixed-bed reactors with low D/d ratio in which the wall effects are dominant, radial porosity profiles of simulated packings are compared to experimental data available in literature and in-house measurement.

6.1 Spherical packings

For spherical packings, DEM simulations were conducted by injecting glass spheres of 3 mm in diameter into a cylindrical container of 17.88 mm in diameter (D/d ratio of 5.96) and 21 mm (D/d ratio of 7, used for heat transfer simulation in Chapter 7). The particle-particle and particle-wall interactions were described by the Hertz-

This chapter is adopted from publications: Y. Dong, B. Sosna, O. Korup, F. Rosowski, R. Horn, Investigation of radial heat transfer in a fixed-bed reactor: CFD simulations and profile measurements, Chemical Engineering Journal 317 (2017) 204-214. Submitted manuscript: Y. Dong, M. Geske, O. Korup, N. Ellenfeld, F. Rosowski, R. Horn, What happens in a catalytic fixed-bed reactor for n-butane oxidation to maleic anhydride? Insights from spatial profile measurements and particle resolved CFD simulations. Submitted to Chemical Engineering Journal, 2018.

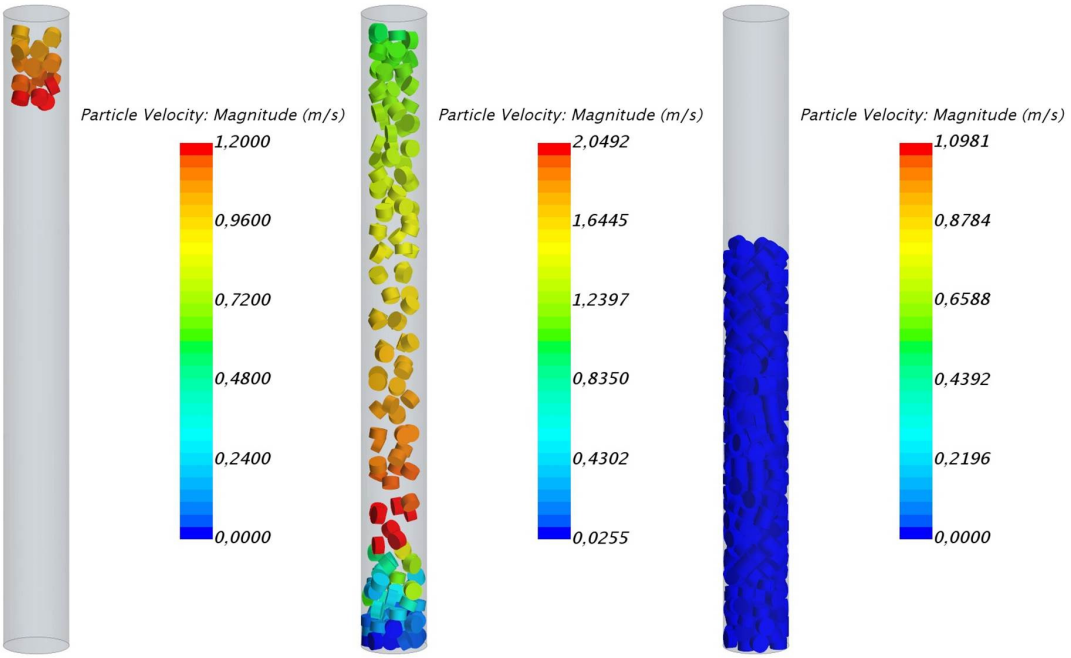

Figure 6.1: Example illustration of a general work flow in a DEM simulation.

Mindlin model as discussed in Section 3.2.1. The material properties were taken from the built-in material database from STAR-CCM+ [140] of glass. The radial porosity profiles were analyzed in the following way: Firstly, the container coordinates r, z, θ were discretized in 100 points in radial direction r, 200 points in height z and 360 points in azimuthal direction θ. Secondly, the distance between the coordinate of each point and the coordinate of the centroid of each sphere was calculated. The sphere centroids were extracted from the DEM simulations. If the calculated distance is smaller or equal to the sphere radius, the porosity is set to zero, otherwise the porosity is set to one. Thirdly, for a given magnitude of the radial coordinate, the porosity values were averaged over all z and θ values.

The resulting radial profiles are shown in Figure 6.2 and 6.3. Good agreement is found between our DEM simulated profile and experimental data from Mueller [205] for a D/d ratio of 5.96. Except for some points in the center of the packing also the correlation suggested by de Klerk [206] is in good agreement with our DEM porosity profiles and the experimental data reported by Mueller [205].

The correlation from de Klerk [206] is used to generate porosity profiles for the $D/d = 7$ ratio investigated in this work in terms of heat transfer (Chapter 7) for which no experimental porosity data could be found in the literature. The DEM simulated porosity profiles were calculated as described above and additionally by analyzing the volume mesh data (denoted as 'DEM, mesh' in Figure 6.3). For the mesh based analysis, the positions of the centroid of each particle from DEM simulations were extracted and the packing was reconstructed in the CAD module in a new simulations. Voids between the particles were volume meshed with polyhedral mesh and 'local flattening' method [26] as discussed in Section 3.2.2. The meshed bed structure was then circumferentially sliced at different radial positions and the averaged radial porosity profiles were obtained as the surface area of the slice divided by the total area (rectangular surface). An example cut plane is shown in Figure 6.4.

Both analysis methods give almost identical profiles with minor deviations in the

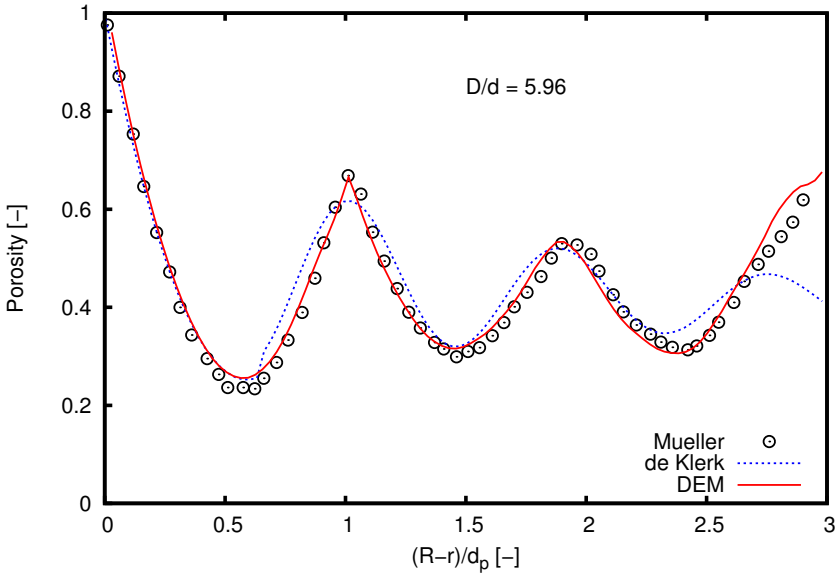

Figure 6.2: Comparison of a DEM simulated radial porosity profile (solid line) to experimental data from Mueller [205] (points) and a correlation from de Klerk [206] (dotted line) at D/d=5.96.

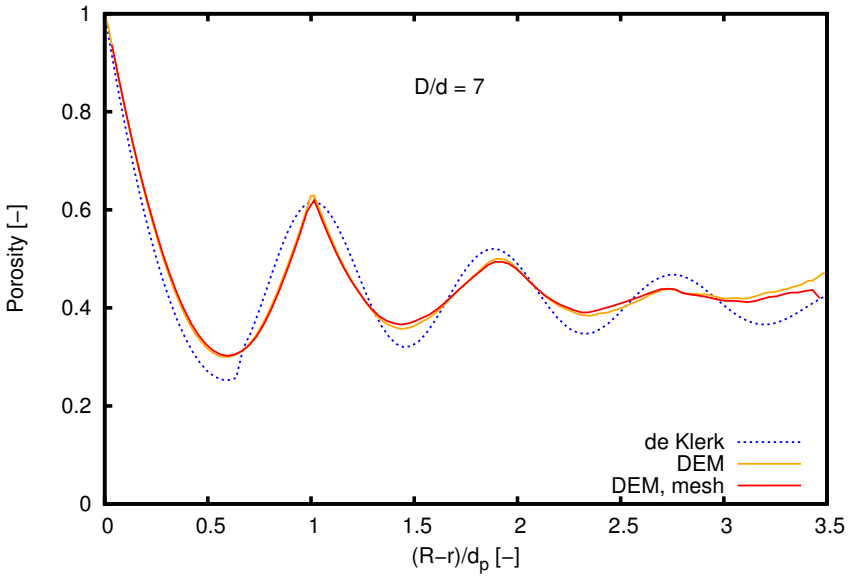

Figure 6.3: Comparison of a DEM simulated radial porosity profile (solid line) analyzed by two different methods described in the text to the correlation from de Klerk [206] (dotted line) at D/d=7.

Figure 6.4: Example cut plane of a spherical packing (left) and a Raschig ring packing (right) for evaluating the mesh based porosity profiles.

bed center indicating that the meshed structure represents the packing very well and that the 'local flattening method' has only a small effect on the porosity. Also, the DEM simulated porosity profile for D/d=7 follows closely the periodicity of the correlation from de Klerk [206] with small deviations in amplitude. The deviations increase towards the center of the packing due to the vanishing ordering effect of the wall [206]. Another possible cause of deviations is that the DEM simulated packing is not 'perfectly dense' in the sense of 'hammering' or 'shaking' the container as done in a packing experiment. In the DEM simulations the particles just drop into the container without any additional measures to densify the packing.

6.2 Raschig ring packings

For modeling Raschig ring packings in DEM simulations, the Raschig rings were approximated by a full cylinder with the same outer diameter and height as the ring. Contact forces between particles and particle with walls were modeled by the liner spring contact model [140]. The mesh based method is used to evaluate the radial porosity profiles. Unlike for spherical packings, radial porosity profiles for Raschig rings are scarce and no general agreement has been reached for correlations [24]. Giese et al. [134] have reported porosity data for glass ring packings ($d_o/d_i/h = 8/6/8$ mm) in a container with 80 mm diameter (D/d=10). This packing was simulated twice by DEM with the same parameters and settings.

Comparison with the experimental data reported by Giese et al. [134] is shown in Figure 6.5. Taking the stochastic nature of the packing process into account, the agreement between DEM simulation and experiment is fair. The periodicity of the porosity profile is nicely reproduced with some deviations in absolute values. In the DEM simulations the particles are dropped from the top of the container at randomized positions and randomized angular velocity. Perfect agreement of repeated simulations can therefore not be expected but the ordering effect of the wall leads to very similar simulation results close to the wall. Towards the center of the bed random fluctuations of the porosity values from repeated simulations occur.

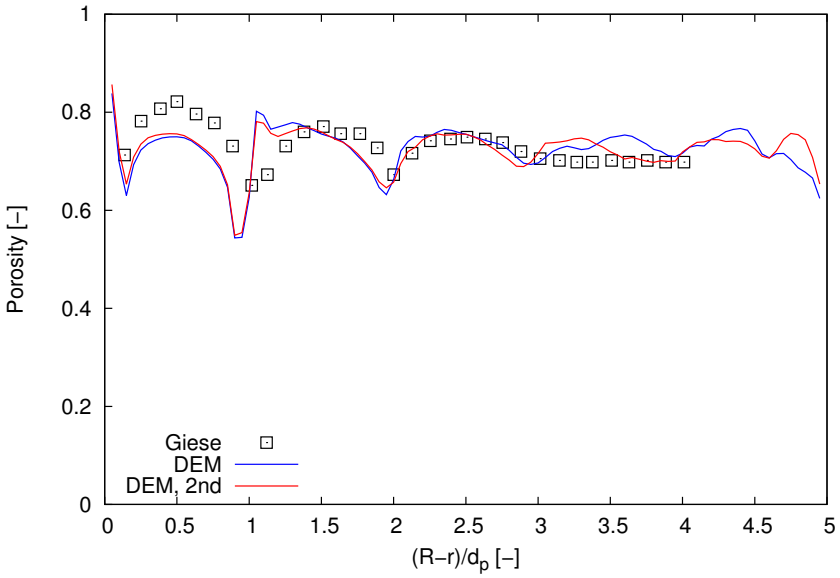

Figure 6.5: Comparison of DEM simulated radial porosity profiles (repeated twice) to experimental data reported by Giese et al. [134] for glass ring packings ($d_o/d_i/h$ = 8/6/8 mm) in a cylindrical container with 80 mm diameter (D/d=10).

Since no literature radial porosity data can be found for packings with low D/d ratio as for industrial reactor for n-butane oxidation, experimental measurement has been conducted with the VPP catalyst pellets (master thesis from Nils Ellenfeld [89]). First, packing of an empty tube was studied by filling an empty acrylic glass tube of 21 mm inner diameter with hollow cylinders of the VPP catalyst (Packing 1, not shown). In a second study, the influence of the central sampling capillary and additional fiber Bragg gratings for temperature measurements running through the reactor tube at different radial coordinates was studied (Packing 2). An acrylic glass tube, again of 21 mm inner diameter, was fitted with a concentric acrylic glass tube (d_o = 3 mm) simulating the central sampling capillary. Three additional acrylic glass tubes (d_o = 1 mm) 5.5 mm, 7.5 mm and 9.5 mm away from the center and at an angle of 120 ° relative to each other were used to simulate the fiber Bragg gratings (Packing 2, Figure. 6.6). Catalyst pellets were then filled in between these components, both in the laboratory and by DEM simulation.

Figure 6.7 and Figure 6.8 illustrate how the porosity profiles were then determined. After filling the acrylic glass tubes with catalyst pellets up to a height of approximately 10 cm, opacified resin was carefully filled in the voids without that air-bubbles were trapped in the packing. After five to seven days, the resin was completely hardened. In the next step, the hardened packings were cut into 40 slices, each approximately 2 mm thick. Each slice was then photographed from bottom and from top. The resulting 80 images were analyzed in the software GIMP [207]. Up to 18 radial positions with a radial step width of Δr = 0.5 mm were analyzed as shown in Figure 6.8. By counting the number of black pixels (solid phase) and white pixels (void), 80 radial porosity profiles were obtained, which, after averaging, gave a representative radial porosity profile of the packing [89].

The model parameters used for simulating these two packings are listed in Table 6.1. Even if physical properties required as input for DEM simulations are unknown or uncertain, e.g. friction coefficients of the catalyst pellets [58, 143], their influence

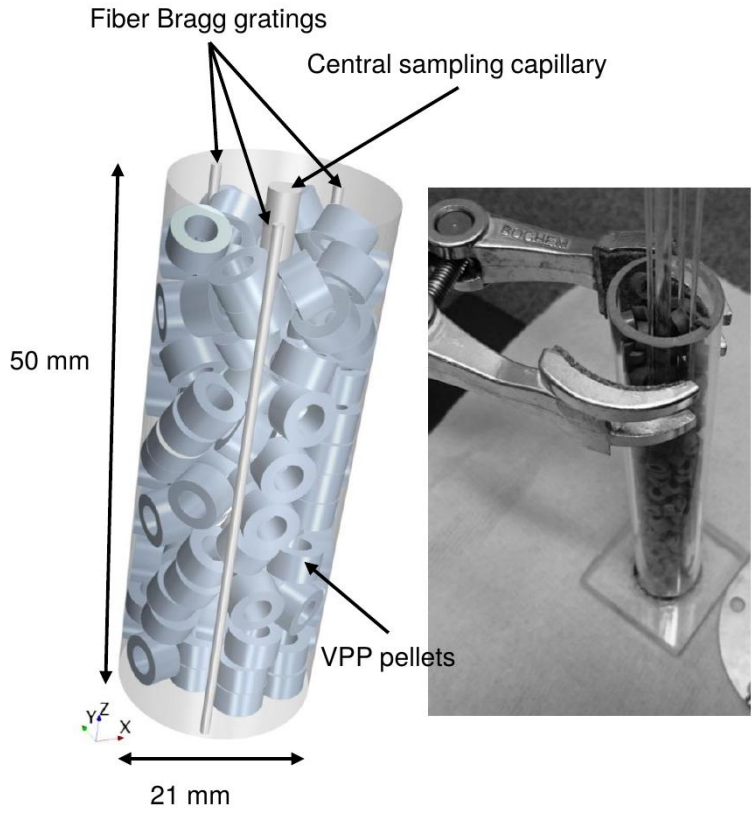

Figure 6.6: Illustration of the simulated (left) and experimental (right) packing of the reactor tube with central sampling capillary and three fiber Bragg gratings for temperature measurements (Packing 2).

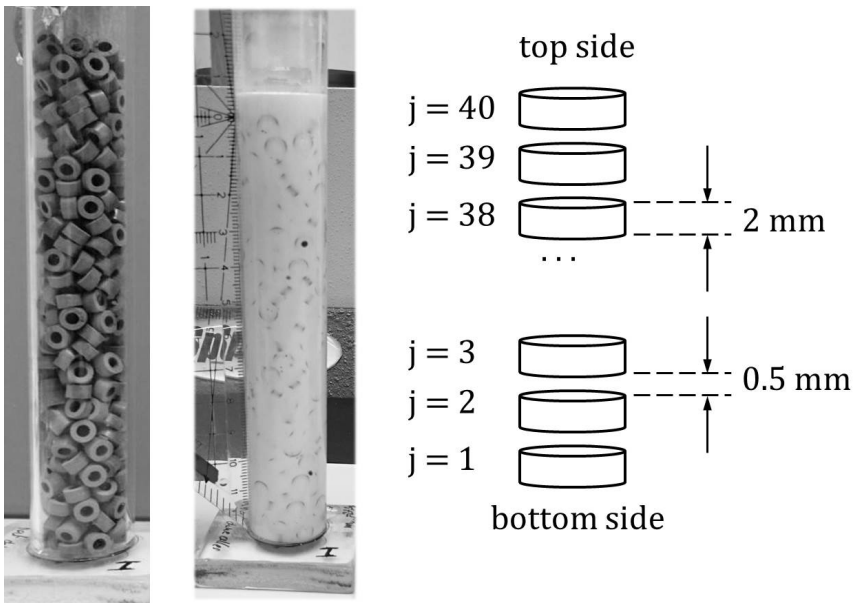

Figure 6.7: Work flow to determine radial porosity profiles: Acrylic glass tube with catalyst pellets (left). Packing filled with opacified and hardened resin (middle). Slicing of the packing into 40 slices of 2 mm thickness (right).

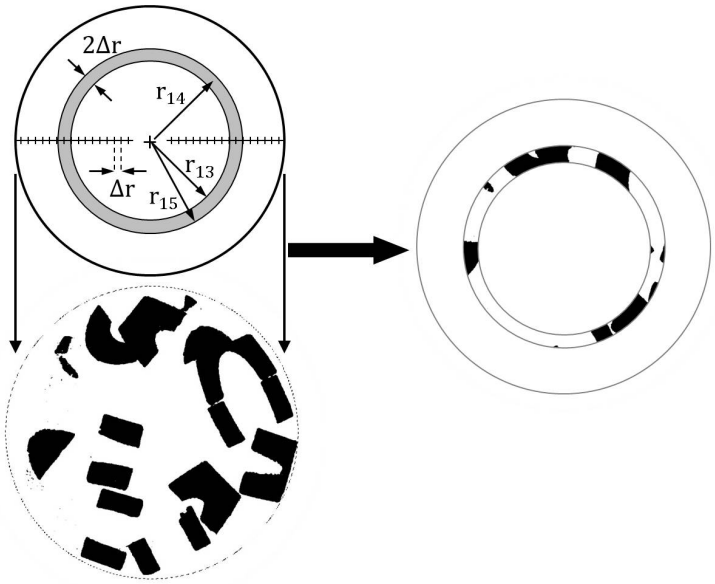

Figure 6.8: Image analysis of a photograph of a slice to obtain radial porosity profiles.

Table 6.1: Parameters used in the DEM simulations of VPP catalyst.

Property	Wall	Particle
Density [kg/m^3]	2500	2645
Poission' ratio [-]	0.235	0.225
Young's modulus [MPa]	78500	17000
Static friction coefficient [-]	0.2	0.2
Normal restitution coefficient [-]	0.9	0.9
Tangential restitution coefficient [-]	0.5	0.5
Coefficient of rolling resistance	0.002	0.002

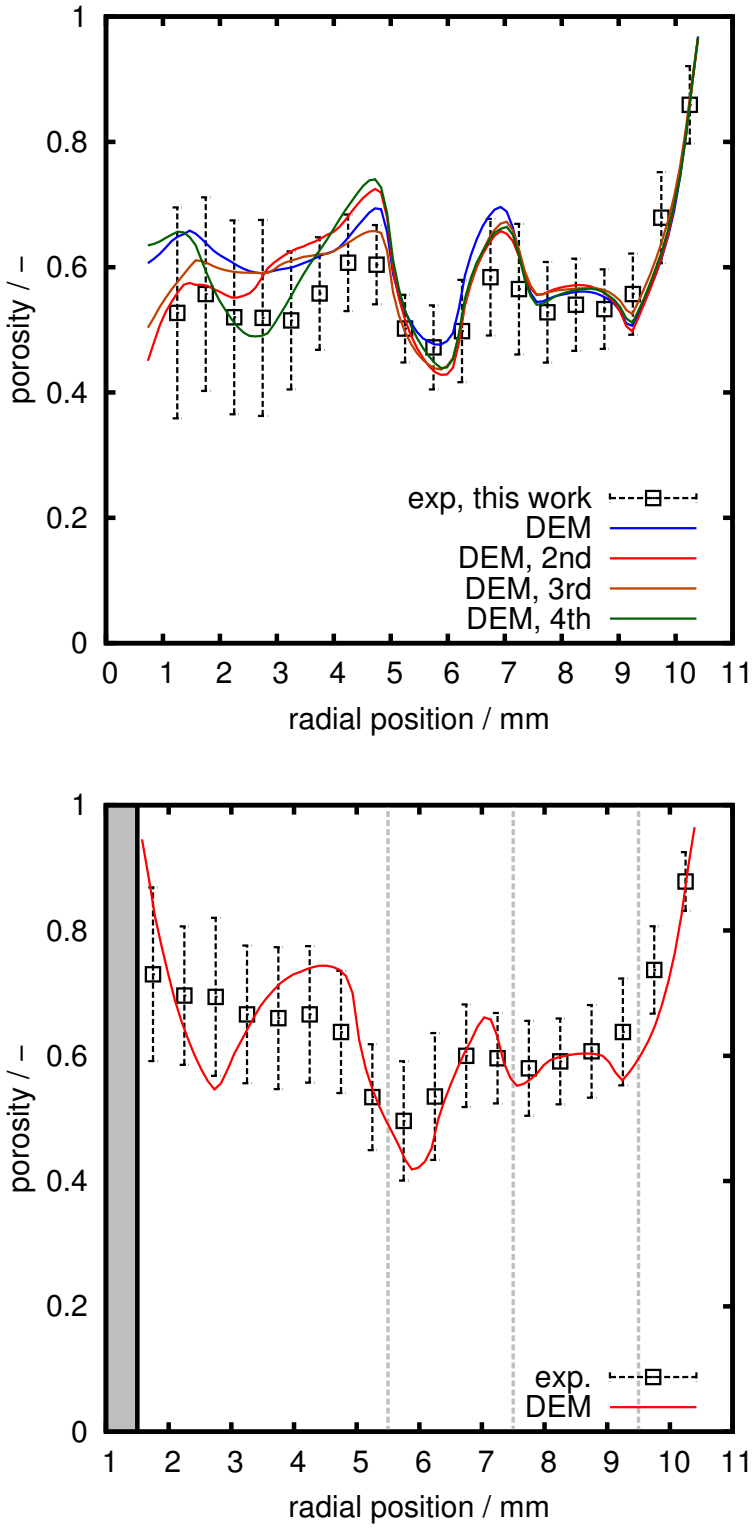

Figure 6.9: Top: Comparisons between simulated (lines) and measured (symbols) radial porosity profiles of Packing 1 (empty tube). Porosity profiles of four repeated DEM simulations are plotted to demonstrate the reproducibility and stochastic nature of the packing process. Bottom: Comparisons between simulated (lines) and measured (symbols) radial porosity profiles of Packing 2 (tube with central sampling capillary and three fiber Bragg gratings). Gray dotted lines indicate the positions of the extra thin tubes simulating three fiber Bragg gratings.

on the final packing is not too pronounced unless particle-fluid interactions or particle breakage are goal of the simulation. In fact it becomes common practice to take these parameters as calibration factors to reproduce the experimental porosity profiles [49, 58, 61].

The simulated and measured radial porosity profiles of the studied two packings are plotted in Figure 6.9. The experimental values are displayed as height-averaged mean values with error bars indicating the fluctuations of the porosity values along the bed. Simulation values are present as height-averaged values. For Packing 1, four simulation results are plotted to illustrate the reproducibility of the DEM simulations. Some difference is observed between the simulations due to the stochastic nature of the random packing. Similar behaviours are also observed for spherical packings in our earlier work [27].

The results are as follows. Close to the wall, porosity values are very high, the simulated porosity profiles agree well with the experimental one, experimental error bars are small and repeated simulations produce almost identical results. All of this is due to the ordering effect of the wall. In Packing 1, this wall ordering effect fades away towards the bed center, the porosity fluctuates around 0.55 and variations in the experimental data and among repeated simulations become larger. For Packing 2, the sampling capillary in the center of the reactor tube introduces another wall and leads to increased porosity values close to it. The disturbances of the thin fiber Bragg gratings are negligible.

6.3 Conclusions

Computer generated random packings by discrete element method are studied in this chapter. DEM simulation mimics the experimental filling process by dropping particles from the top of the container with randomized inject position, angular velocity as well as initial rotation for non-spherical particles. The packing structures generated from DEM simulations are verified by comparing the height-averaged radial porosity profiles from simulations with experimental data. DEM simulations have been validated as a reliable tool for generating realistic spherical and ring type packings at various D/d ratios. Two methods are used to evaluate the radial porosity profile of spherical packing: analytical and mesh based. Both methods give almost the same result indicating the meshing strategy used in this work has minimized influence on the resulting bed structure.

High porosity values are found in the vicinity of the container wall for both packings. This is due to the wall ordering effects which damps away towards the packing center. Due to the stochastic nature of random packings, DEM simulations with the same input generate not identical packings. Radial porosity profiles from repetitive simulations show same profile shape with minor difference towards the center where wall effect are less pronounced.

Packings of VPP catalyst pellets in an acrylic container with same diameters as the profile reactor (Chapter 8) have been investigated numerically and experimentally. In addition, the influence of possible extra sampling instruments to the packing is also studied. For both scenarios, good agreement has been found between simulated and measured radial porosity profiles and the influences of extra wall to the packing are well captured by the DEM simulations. In summary DEM generated packings reproduce the experimental packings within stochastic bounds. It can be concluded that packing and meshing are physically sound and can be used for particle resolved CFD simulations of fixed-bed reactors at small D/d ratios.

"Just because the results are in colour, it doesn't mean they are right."
Hugh Stitt et al. [57]

7 Heat Transport: CFD Simulations and Validations

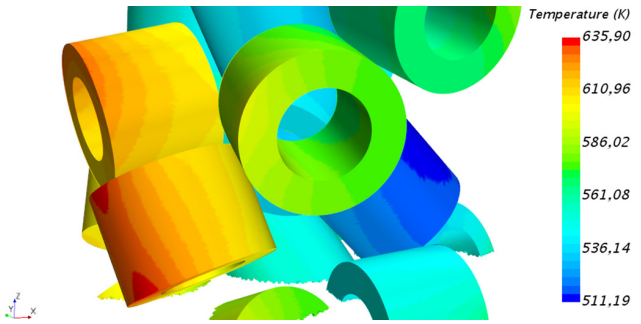

Randomly packed fixed-bed reactors with small reactor to particle diameter (D/d) ratios are widely used in industrial practice for exothermic oxidation reactions (e.g. oxidation of n-butane to maleic anhydride [72]) or endothermic reforming reactions due to the enhanced radial heat transport rate [116]. For those reactors, it is of vital importance to describe accurately the heat transport properties and the position of the hot-spot to prevent run-away and deactivation of the catalyst [208, 209]. Few studies have been carried out to validate CFD simulations of heat transfer in fixed-bed reactors. Simulations of pure heat conduction in the solid (no flow) have been proven to be correct [57]. Furthermore, validations of simulations of convective heat transfer by comparing to experimental results of spherical packings are reported [29, 114]. More validations at different operation conditions would be desirable. For non-spherical packings, which are more often employed in industry [30], no validation of DEM-CFD simulations of fixed-bed heat transfer is reported so far.

Critical validation study requires experimental input in high quality [210]. In previous studies temperature profiles were measured by inserting individual thermocouples in the packing at different radial positions [98]. This experimental set up has a few drawbacks: limitation of the number of the temperature points obtained, conduction by the metallic sheaths and damage of the thermocouples during experiments [98]. Further improvements in the experimental set up to increase the spatial resolution and remove the bias in the obtained data would be necessary. Profile measurement techniques developed by Horn et al. [211] have been applied to obtain sub-millimeter resolution species and temperature profiles under reaction conditions [85, 198, 212]. Hence, this chapter pursues two objectives: one is to propose an improved experimental technique to provide high quality temperature data. The other is to provide validations of CFD simulation of heat transfer in a fixed-bed reactor with low D/d ratio ($4 \leq D/d \leq 7$) for both spherical and Raschig ring packings in moderate flow conditions and high temperature ranges.

This chapter is adopted from publication: Y. Dong, B. Sosna, O. Korup, F. Rosowski, R. Horn, Investigation of radial heat transfer in a fixed-bed reactor: CFD simulations and profile measurements, Chemical Engineering Journal 317 (2017) 204-214.

Table 7.1: Physical properties of the packing materials used in experiments of measuring radial heat temperature profile.

packing type	geometry parameters [mm]	thermal conductivity [W/m/K]
glass spheres	d: 3	1.4
steatite rings	$d_o/d_i/h$: 6.2/3.5/4.5	2.5

7.1 Experimental details

A pilot-scale fixed-bed reactor of 21 mm inner diameter, with side ports for sampling in radial direction, was employed. A fused silica capillary (0.7 mm inner and 0.85 mm outer diameter) was placed in the side port. A type K thermocouple (0.5 mm diameter) was inserted in the capillary and the loose end was fixed on a linear axis with a stepper motor. This setting allowed the thermocouple to be moved through the reactor in radial direction with a resolution of 10 μm. With this procedure radial temperature profiles for two different angular positions were obtained. Figure 7.1 illustrates the experimental set up where the capillary is magnified for illustration purpose (master thesis of Bahne Sosna [90]).

Synthetic air (mixture of 80 % nitrogen and 20 % oxygen) pre-heated to 60 °C entered the reactor from the top. The reactor wall was heated by electrical heaters to 400 °C. Due to the fixed position of the side sampling port and fast flattening temperature profiles in the investigated system, only a short bed was packed without calming section. Two packing materials were used: glass spheres and steatite rings. The geometry and physical properties are given in Table 7.1. The packing height of the glass spheres was 3.4 cm and 6.6 cm whereas for steatite rings it was 6.0 cm and 9.4 cm above the sampling position. There was approximately 9.5 cm packing under the sampling position to avoid the influence of the metal holder and mixing effect of the gas stream. Measurements with flow rates of 10 and 15 l/min (at STP) were conducted at steady state.

7.2 Simulation details

The random packings of glass spheres and steatite rings are generated by the discrete element method. In the DEM simulations, both particle-particle and particle-wall interactions are considered and described by the Hertz-Mindlin model for glass spheres and liner spring model for steatite rings (section 3.2.1) [144]. The material properties are taken from the built-in material database from STAR-CCM+ [140]: glass for the glass spheres and magnesium oxide for the steatite rings. The particles are injected randomly from the top of the reactor and fall down due to gravity. The steatite rings are approximated by a cylinder particle with the same outer diameter and height as given in Table 7.1. For the injection of the cylinders, randomized angular velocity is used to mimic the experiment. The DEM simulation is stopped when all the particles are settled i.e. when the particle velocity is almost zero.

Simulations were set up according to the experiments with the same operation parameters and packing heights. Hence, both heat transfer in the empty tube and in the packing was simulated. The influence of the capillary and the packing below the capillary was not considered in the simulations. The flow is non-isothermal and

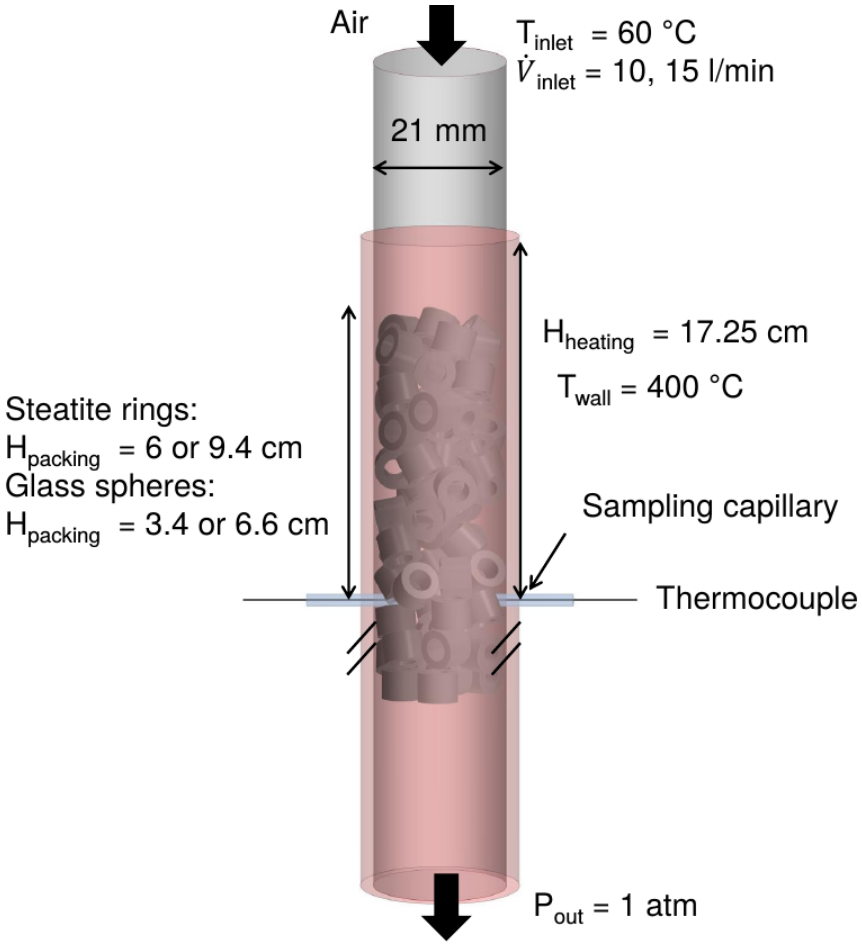

Figure 7.1: Schematic illustration of the experimental set-up of measuring radial heat temperature profile. The size of the capillary is magnified for illustration purpose.

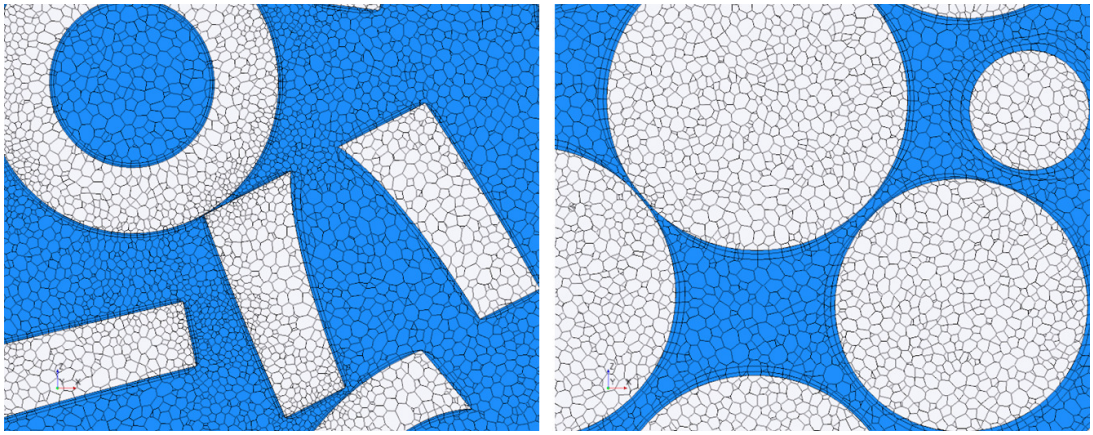

Figure 7.2: Illustration of the meshed surface of a ring packing (left) and a spherical packing (right).

Table 7.2: Meshing parameters used in heat transfer study. The packing height for glass spheres is 3.4 cm, for steatite rings 6 cm. The extrusion mesh cells of the inlet and outlet are not counted in the cell counts.

packing type	particle counts [-]	base size [mm]	cell counts [million]
glass spheres	444	4	4.2
		3	11.8
		2	29.2
steatite rings	66	4	3.6
		3	5.5
		2	8.8

standard conservation formulations of momentum, mass and energy were applied [114]. The particle Reynolds numbers are calculated based on the volume equivalent diameter for the Raschig rings and diameter for spheres [24]. They are in the range of 60-100, which fall in the transient range between laminar and fully turbulent flow [26]. Hence, simulations with both a laminar model and the 'realizable $k-\varepsilon$' model with 'all $y+$ treatment' were conducted. This model with combined wall treatment is recommended for both low and high '$y+$' situations. The physical properties of the fluid were taken from air and considered as temperature dependent by means of kinetic theory. The physical properties of the solid phase are given in Table 7.1. The following boundary conditions were applied: velocity and temperature at the inlet and ambient pressure at the outlet. 'No-slip' boundary conditions were applied at the reactor wall as well as at the particle surfaces. A fixed value of 400 °C was set at the reactor wall. All simulations were done at steady state and were computed parallel on a computing cluster.

Mesh independence studies were carried out for a base size of 2-4 mm. Simulated radial temperature profiles for glass spheres and steatite ring packings are given in Figure 7.3. For both packings, mesh independence is reached at a base size of 3 mm. Therefore, all simulations were done with a base size of 3 mm. Meshing is the bottleneck in the whole work flow since it is highly RAM (Random-Access Memory)

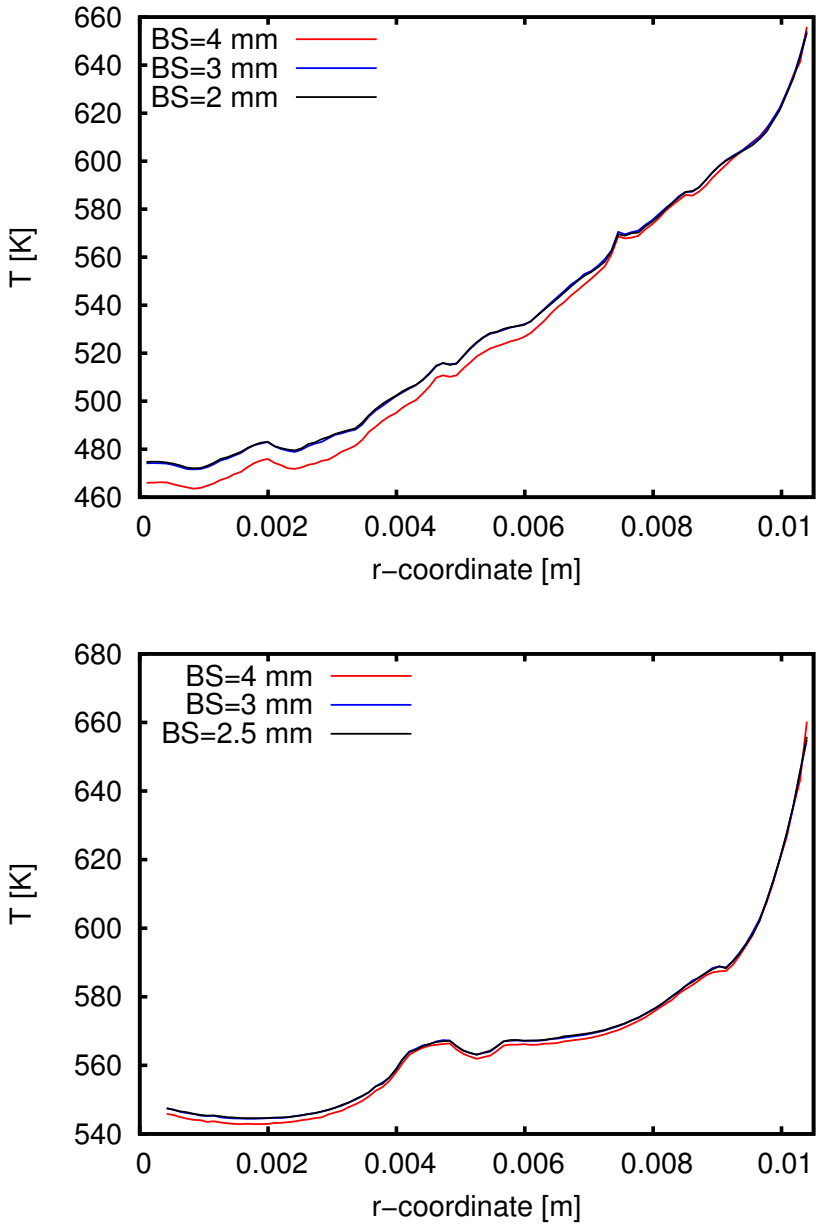

Figure 7.3: Simulated radial temperature profiles at different mesh base size for: (left) a glass sphere packing with a packing height of 3.4 cm and a volumetric flow rate of 15 l/min, (right) a steatite ring packing with a packing height of 6.0 cm and a volumetric flow rate of 15 l/min.

Table 7.3: Global bed porosity of glass spheres and steatite ring packings.

packing type	experimental value [-]	simulation value [-]
glass spheres	0.38 ± 0.066	0.46
steatite rings	0.66 ± 0.009	0.69

demanding. As shown in Table 7.2, refinement from a base size of 4 mm to 3 mm more than doubles the mesh size for packing of 444 spherical particles. Thus, for further implementation of a higher number of particles, a trade-off between accuracy and computational efforts has to be made.

7.3 Results and discussion

In addition to comparing DEM simulated porosity profiles to correlations and experimental data as shown in Chapter 6, the global bed porosity of the packings used in the present work on heat transfer was measured in a glass tube with the same inner diameter (21 mm) as the reactor tube shown in Figure 7.1. The results are summarized in Table 7.3. The global porosity of the DEM simulated steatite ring packing is in good agreement with the measured value. The global porosity of the simulated glass sphere packing is higher than the measured value. Possibly the rate of dropping particles into the container is higher in the DEM simulation than in the experiment resulting in slightly 'looser' packings. However, also the experimental error bar for the glass sphere packing is much higher than for the steatite rings indicating that also the experimental values are prone to error. Overall the results presented above are reassuring that the DEM simulations conducted in the present work generate realistic particle packings for the simulations presented in the following.

Typical velocity- and temperature fields of sphere and steatite ring packings from the particle-resolved CFD simulations are shown in Figure 7.4 and Figure 7.5, respectively. For both packings, local inhomogeneities in the velocity fields are observed [213]. Channeling or bypass is found near the wall and in areas where the packing is loose. At some points, especially in the wake of the particles, the velocity is very low or the gas is even stagnant. These observations are typical for flow inside fixed-beds with small D/d ratio [26, 114, 118]. In reactors employing such packings wall effects are high and the internal flow is far from plug-flow [97]. The local inhomogeneity is higher for the steatite ring packing due to the low D/d ratio (around 4) and arbitrary orientation. In Figure 7.5, many local voids with high velocity can be seen, whereas stagnant zones are visible inside the rings and in places where the packing is more dense [118].

The temperature field in each packing 'maps' the velocity field closely. Lower temperature spots can be seen where the local velocity is high and vice versa. The inhomogeneity in the temperature field of a steatite ring packing is much higher than in a sphere packing. As shown in Figure 7.5, the shape of some individual particles can even be recognized in the temperature field. In contrast to the almost rotationally symmetric temperature field in a sphere packing, there is no rotational symmetry in the temperature field of a steatite ring packing. Hence, it is difficult to reach a high enough accuracy when applying axis-symmetric two-dimensional models for steatite ring packings at low D/d ratios. Particle resolved CFD simulations resolve local

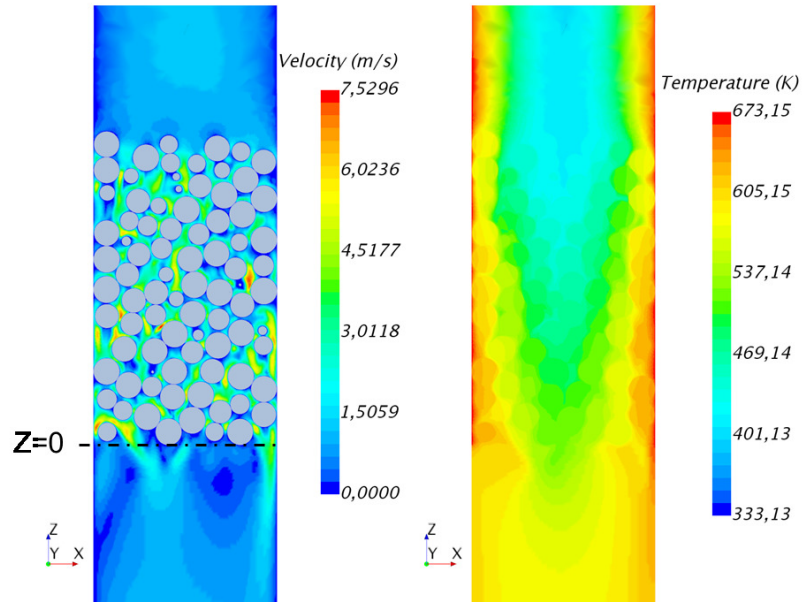

Figure 7.4: Typical velocity field (left) and temperature field (right) of a spherical packing. The packing height in this example is 6.6 cm.

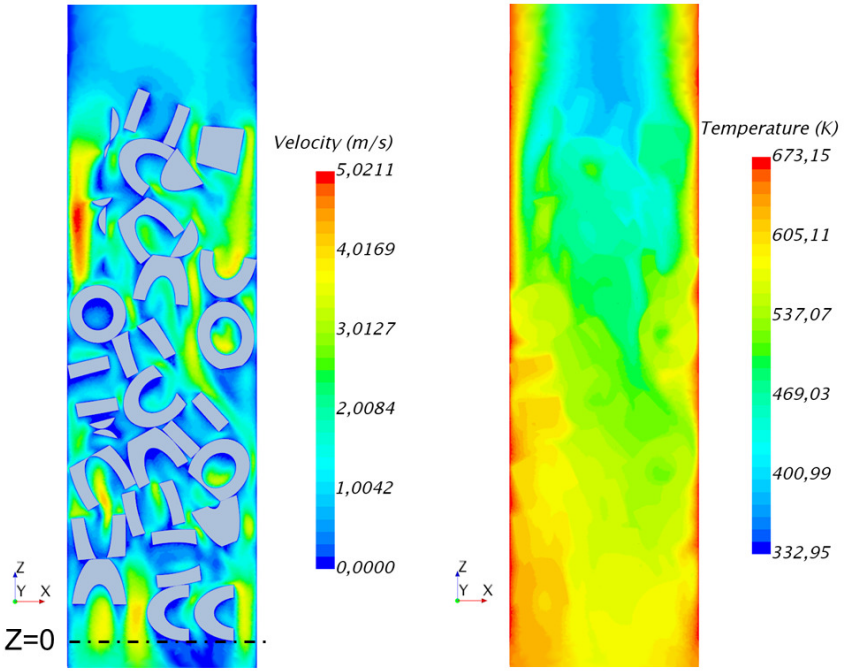

Figure 7.5: Typical velocity field (left) and temperature field (right) of a ring packing. The packing height in this example is 6.0 cm.

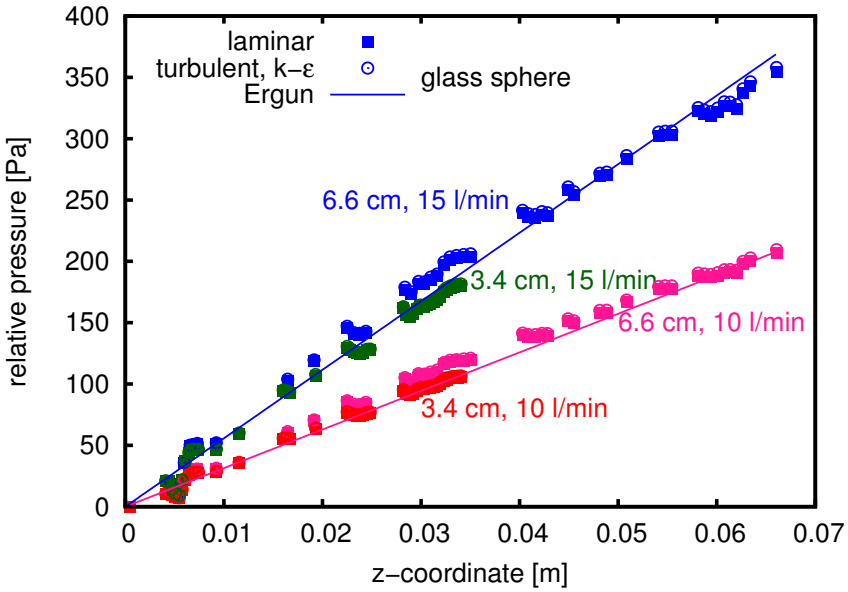

Figure 7.6: Simulated pressure drop of glass sphere packings with laminar model (squares) and $k-\varepsilon$ model (points) compared to the Ergun equation (lines).

velocity and temperature inhomogeneities in ring packings much better.

In order to gain confidence of the prediction of the turbulence model with the wall treatment function used in this work at low particle Reynolds numbers, laminar simulations were also conducted. The pressure drop along the center line of the bed is sampled for all packings and flow rates for both glass spheres and steatite rings.

Comparisons of the predicted pressure drop are presented in Figure 7.6 and Figure 7.7. The laminar and the turbulence model give almost identical results, both for the glass spheres and for the steatite rings. This indicates that in the studied flow regime ($Re_p = 60-100$), the turbulence effects are very small and that the flow behaves almost laminar. Also the low values of $y+$ (< 1) found after initializing the simulations point in this direction. More important than the choice of the flow model at low Re_p numbers is the packing structure. For sphere packings, up to 350 Pa pressure drop is observed in good agreement with the Ergun equation based on the simulated global porosity listed in Table 7.3. For the steatite rings the porosity is higher and the pressure drop is lower. In contrast to the well established Ergun equation for sphere beds no reliable correlation exists for ring packings.

Figure 7.8 compares CFD simulations and experimental radial temperature profiles of glass sphere packings at different bed heights and different inlet volumetric flow rates. The experimental values are taken as average of the two values measured at the same radial positions. The original experimental data have a resolution of 10 μm. For illustration purpose, only data points at every 500 μm are plotted. The simulation results are evaluated as circumferential average of the fluid temperature at different radial positions. Simulation results of both the laminar model and the turbulence '$k-\varepsilon$' model are presented. For one set of conditions: packing height of 3.4 cm and flow rate of 10 l/min, a turbulent '$k-\omega$' simulation was conducted. As can be seen in Figure 7.8 all three models give very similar radial temperature profiles.

Fair agreement can be found between measurement and simulation, especially for the packing height of 3.4 cm. Higher deviations can be found for the packing height of 6.6 cm with a maximum temperature difference of 30 K in the bed center. Similar

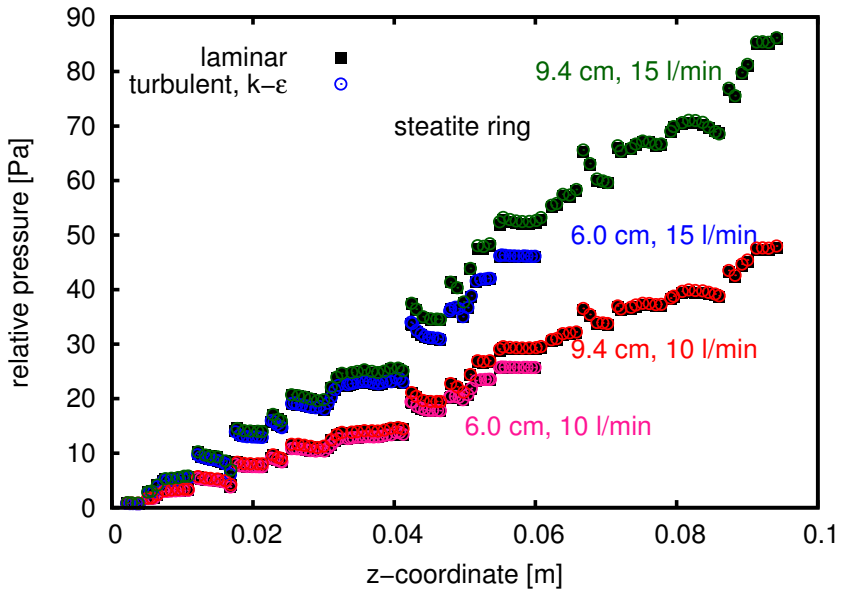

Figure 7.7: Simulated pressure drop of Raschig ring packing with laminar model and $k - \varepsilon$ model.

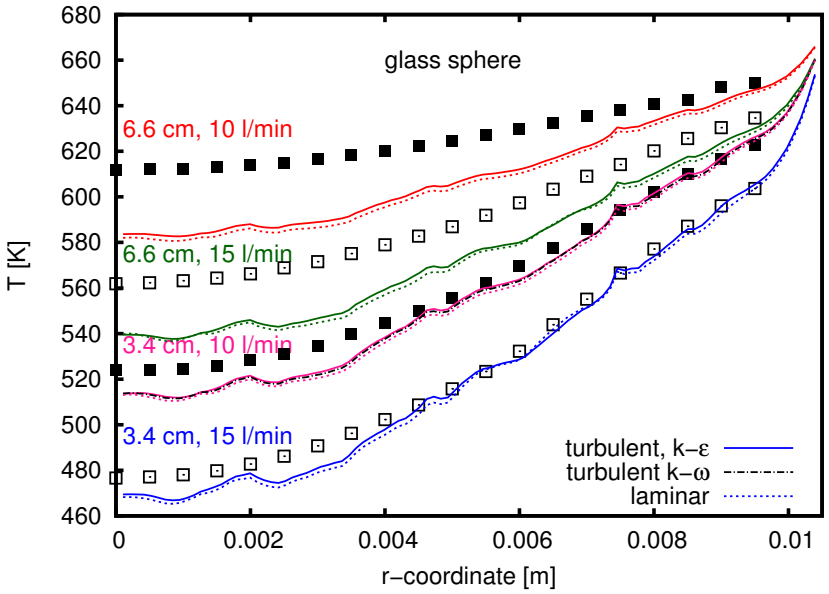

Figure 7.8: Comparison of simulated radially averaged temperature profiles (lines) with experimental measurements (points) at different bed heights and flow rates for glass sphere packings.

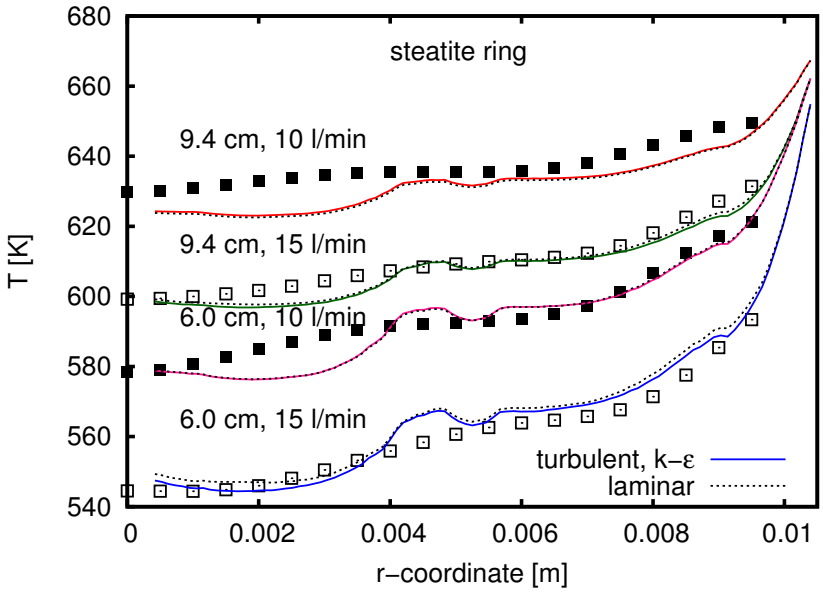

Figure 7.9: Comparison of simulated radially averaged temperature profiles (lines) with experimental measurements (points) at different bed heights and flow rates for steatite ring packing.

trends are reported in earlier studies [29, 114]. Both experimental errors and model deficiencies may contribute to this deviations. In the investigated flow region, conduction plays a big role [107]. Because heat is conducted from the tube wall to the bed center, a higher porosity from the DEM simulation will lead to a systematic underestimation of temperatures inside the packing. This systematic underestimation is less pronounced at high flow rates because convection becomes the dominant heat transport mechanism. Another systematic source of error is the meshing, where local flattening techniques are used for the contact point problem as shown in Figure 7.2. This artificially creates fluid volume in between the particles which reduces heat conduction from the reactor wall to the particles and in between them. Also this effect results in a systematic lower temperature profile than in reality. A third systematic error leading to underestimation of heat transport to the bed center is omission of radiation. Radiation becomes important if materials are glowing but because temperatures are low in this study ($T_{max} = 400\ ^\circ\mathrm{C}$) it was omitted here. Including radiation would introduce a large number of uncertain parameters into the model like emissivities and would make the computations even more demanding than they already are.

Figure 7.9 shows the comparison of the simulated and measured radial temperature profiles of the steatite ring packing at different packing heights and inlet volumetric flow rates. The missing values of the simulation data in the center ($r = 0$) are due to the occupancy of the particle while only fluid temperature is sampled. The laminar and turbulent '$k-\varepsilon$' model predict the same radial temperature profiles at the studied Re_p. For this packing, good agreement is observed between simulations and experiments.

In terms of random errors, the stochastic nature of the packing process has to be considered. The DEM simulated packing will be different from the experimental bed and hence the experimental temperature profile will always be slightly different from the simulated one. To study the influence of the packing simulation on the predicted temperature profiles, additional simulations were conducted in which physical packing parameters were varied. Figure 7.10 shows a variation of Young's modulus for all

experimental conditions. A low value of Young's modulus causes a quick dissipation of kinetic energy and hence a quick settling of the particle bed. For a high value of Young's modulus the particle bed takes long to come to rest. As can be seen the effect of Young's modulus on the resulting porosity profiles is small and within the stochastic variation of the packing process itself (Figure 7.10, top). Accordingly, no systematic effect on the temperature profiles can be observed (Figure 7.10, bottom).

In a further set of simulations shown in Figure 7.11, the static friction coefficient of the particles was varied. If the particles are modeled with a smooth surface (low friction coefficient), a globally more dense packing is obtained. If the particles are modeled with a rough surface (high friction coefficient), a globally less dense packing results. The difference in global porosity is high enough to cause a systematic influence on the temperature profiles [61].

Furthermore, the measured profiles represent only one trajectory across the reactor while simulation values are circumferential averages. Figure 7.12 (left) shows an example of the temperature field at the bottom plane section of the glass sphere packing. The temperature profiles are different in each radial direction. For detailed analysis, fluid temperature points are sampled in two directions ($-x$ to $+x$, $-y$ to $+y$) and plotted in Figure 7.12 (right) together with the original experimental data. Both measured and simulated temperature profiles are not exact axis-symmetrical with 5 to 10 K difference at $-r$ and $+r$. Up to 20 K difference in the simulation results from different sampling directions can be found. To minimize this random variations in the experimental data, more measurements at different directions would be required.

As already discussed in Figure 7.5, fixed-bed reactors packed with rings at low D/d are more inhomogeneous and the temperature profiles do not show axis symmetry. This inhomogeneity is illustrated in a radial cut section shown in Figure 7.13. Compared to the spherical packing shown in Figure 7.12, local fluctuations of the temperature profile are much more pronounced. The radial fluid temperature profiles at two directions are sampled and plotted in Figure 7.13 (right). Since only the fluid temperature is sampled, the line plots have a different span according to the occupancy of the ring particles. Up to 50 K difference can be observed at certain radial position e.g. at r= -0.0075 m. In validation studies such local effects must be considered. In certain cases, the simulation performance may appear poor simply by comparing to the experimental data from other directions.

The accuracy of the heat transport simulations depends also on the correct modeling of the gas properties, in particular at high temperatures. Figure 7.14 compares the radial temperature profiles with constant gas properties taken at room temperature and with temperature dependent gas properties calculated by kinetic theory. The profiles differ by more than 20 K. Similar results are found for the glass sphere packings. In previous studies, experiments were done with steam-heated jackets at atmospheric pressure and were limited to 100 °C [98]. At this low temperature range, deviations due to constant gas properties may not be observable [114]. In higher temperature ranges, it is recommended to use temperature dependent gas properties. Also the physical properties of the solid packing material vary with temperature. At steady state, only the thermal conductivity is relevant. Due to a lack of the temperature dependent thermal conductivity of the packing materials used in the present work this could not be studied.

The high inhomogeneity of ring packings cannot be captured by rotationally symmetric pseudo-homogeneous models employing effective transport parameters. For systems similar to the present study, three-dimensional CFD simulations are more accurate. Ring packings, e.g. Raschig rings, are often used in industry. Tubular fixed-

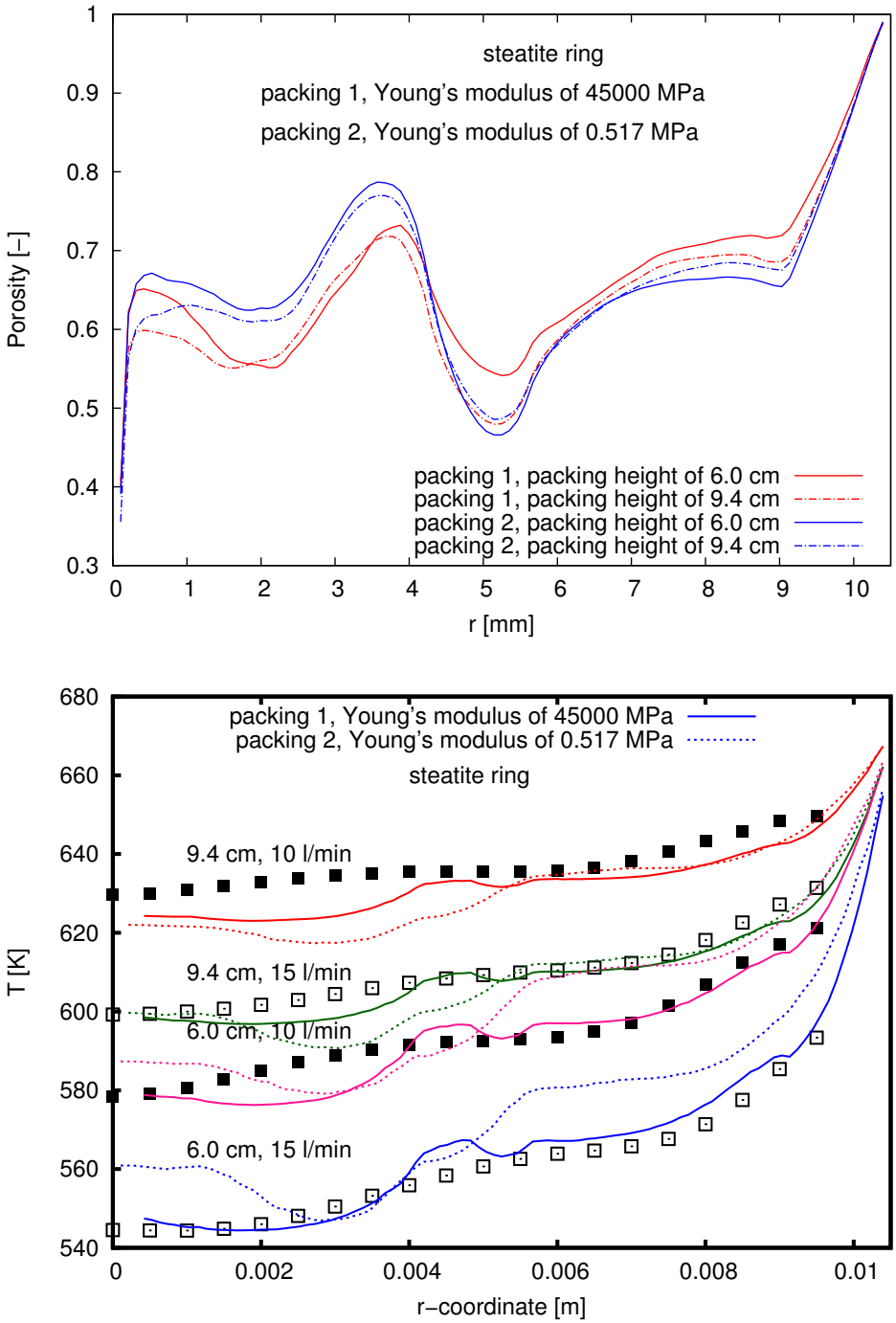

Figure 7.10: DEM simulations of steatite ring packings with different values of Young's modulus. Top: Porosity profiles. Bottom: Temperature profiles.

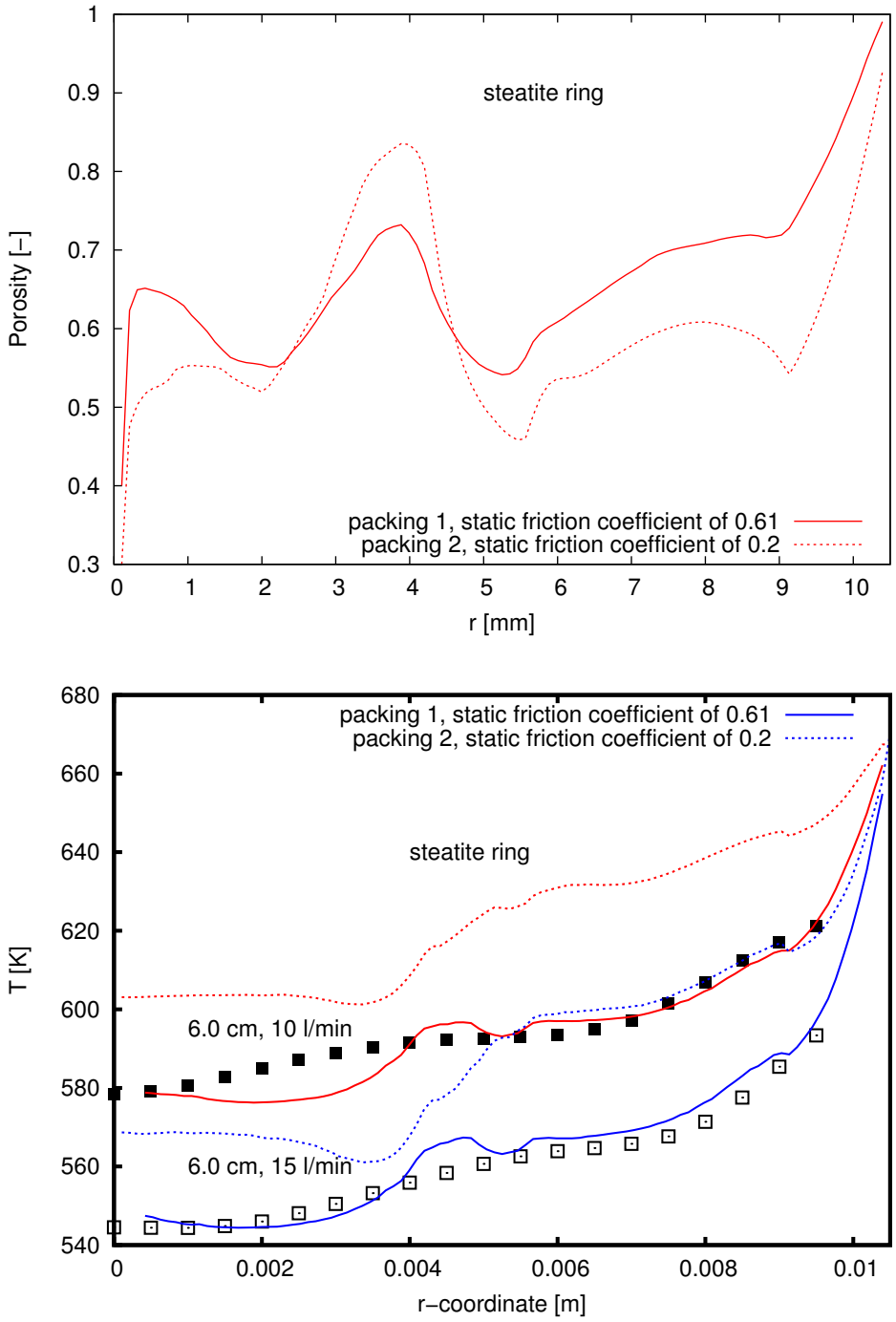

Figure 7.11: DEM simulations of steatite ring packings with different values of the static friction coefficient. Top: Porosity profiles. Bottom: Temperature profiles.

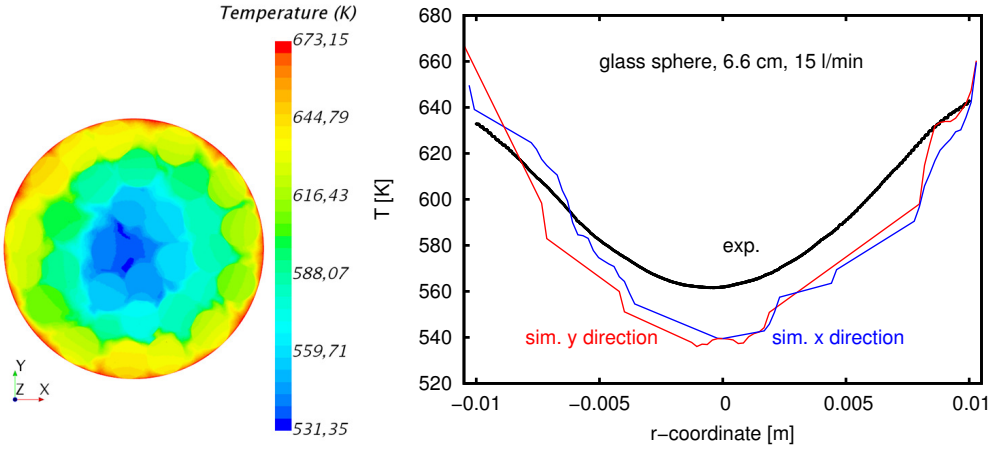

Figure 7.12: Left: temperature field at the bottom plane section of the glass sphere packing (z = 1.5 mm). Right: comparison of the experimental data with the radial temperature profiles of glass sphere packing sampled at two directions. Packing height is 6.6 cm, inlet volumetric flow rate is 15 l/min.

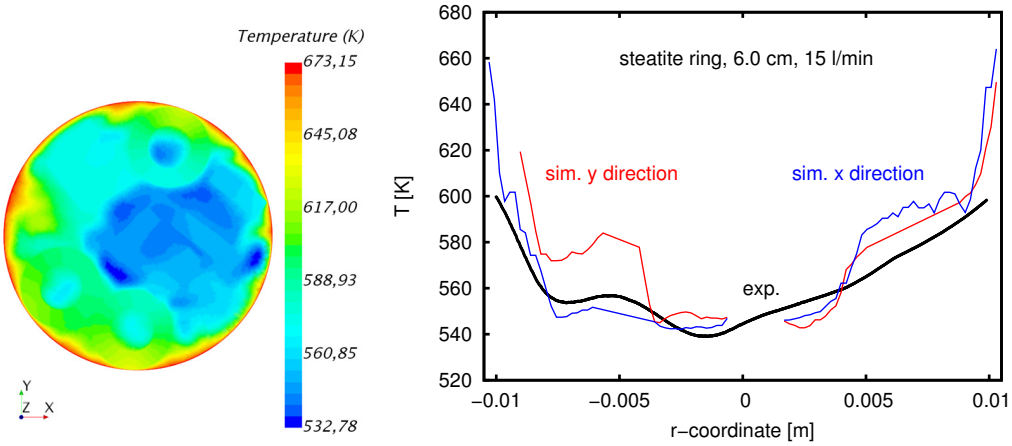

Figure 7.13: Left: temperature field at the bottom plane section of the steatite ring packing (z = 2 mm). Right: comparison of the experimental data with the radial temperature profiles of steatite ring packing sampled at two directions. Packing height is 6.0 cm, inlet volumetric flow rate is 15 l/min.

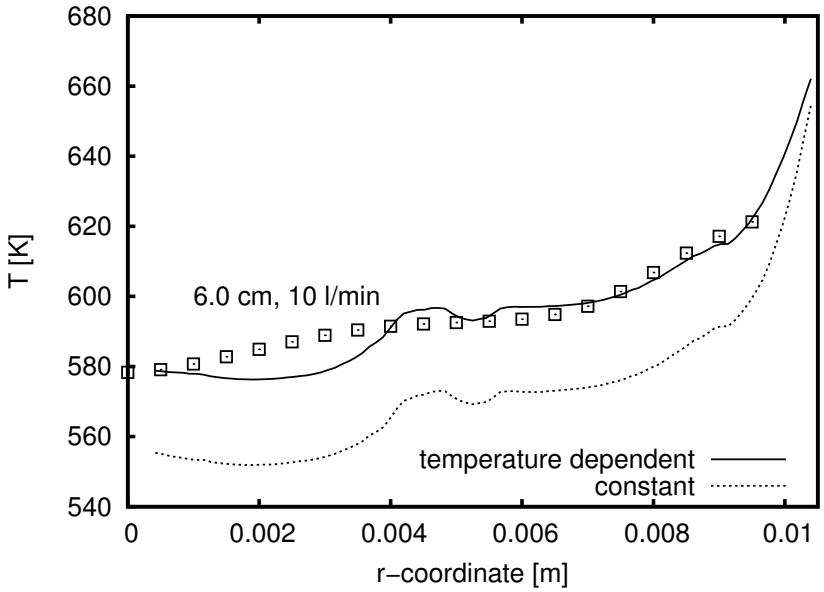

Figure 7.14: Effect of the gas properties on the radial temperature profiles of the steatite ring packing. Packing height is 6.0 cm, inlet volumetric flow rate is 10 l/min.

bed reactors with low D/d are employed for highly exothermic reactions like catalytic oxidations (e.g. n-butane oxidation to maleic anhydride). Due to the heat of reaction, local temperature inhomogeneities might even be higher than without chemistry and the catalyst pellets packed in the same axial position might see very different thermal environments. Because reaction rates depend exponentially on temperature the concentration field around a single pellet can be very different. Therefore, spatially resolved simulations are needed for more accurate predictions.

The critical judgement of the simulation performance is based on the high resolution of the experimental points achieved by the profile measurement techniques [195, 211]. Even though the point density inside the bed is high, the resolution of temperature points near the reactor wall remains a challenge. In Figures 7.8 and 7.9, the experimental points in the vicinity of the reactor wall are not presented. This is due to the difficulty avoiding influence from the ambient air near the side sampling ports. We believe with further development of profile measurement techniques, more precise description of heat transport in fixed-bed reactors can be achieved.

7.4 Conclusions

This chapter provides validations of the DEM-CFD approach for simulating heat transfer in a fixed-bed reactor with small D/d ratio at different flow rates and packing heights. Good agreement is found between the simulated and measured radial temperature profiles of spherical and ring type packings at different packing heights and flow rates. The DEM-CFD approach works particularly well in cases when the packing can be accurately modeled like in this work for steatite rings. If the packing is not accurately simulated like for long sphere packings systematic errors result. The high resolution of experimental data obtained from spatial profile measurements makes it possible to critically evaluate the predictions of the simulations. Therefore, the profile measurement techniques can be a useful tool to provide insight into the reactor and to deliver high quality data for theoretical developments.

Both simulation and experiment reveal the local inhomogeneity of fixed-bed reactors with small D/d ratio especially for ring type packings which are often used industrially. Spatially resolved CFD simulations with computer generated packings are superior to pseudo-homogeneous or heterogeneous models in terms of details and accuracy. With the ever increasing computational power this type of simulations might become the industry standard for future reactor modeling.

8 N-butane Oxidation to Maleic Anhydride: CFD Simulations and Profile Measurements

N-butane oxidation to maleic anhydride (MA, Eq. 8.1) is an important catalytic oxidation process. In 2015 the annual worldwide MA consumption amounted to 2.8 Mio metric tons [68]. One popular process variant employs multi-tubular fixed-bed reactors filled with catalyst pellets of vanadyl pyrophosphate (VPP) cooled by circulating molten salt [69, 70]. The fixed-bed process runs typically at 80-85 % n-butane conversion achieving an overall MA yield of about 57-65 % [72]. This unsatisfactory MA yield motivates chemists and chemical engineers to improve reactor and catalyst performance. In view of the large scale of the process even small improvements translate into significant revenue [72].

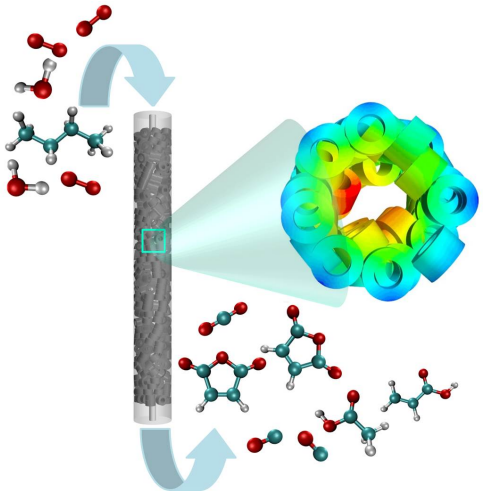

$$C_4H_{10} + 3.5\ O_2 \rightarrow C_4H_2O_3 + 4\ H_2O \quad \Delta H^{\circ}_{R,298K} = -1240\ \frac{\text{kJ}}{\text{mol}} \tag{8.1}$$

Radial heat transfer limitations require rather small reactor tubes for this exothermic reaction (Eq. 8.1). Typical inner diameters are on the order of a few centimeters. Pressure drop determines size and shape of the catalyst pellets. Hollow cylinders of bulk VPP with an outer diameter of 5-6 mm are often used. Therefore, industrial catalytic fixed-bed reactors for n-butane oxidation are characterized by small D/d ratios (ratio of reactor diameter D to pellet diameter d). The random packing of catalyst pellets in reactor tubes fitting only a few particles across the tube diameter leads inevitably to pronounced local inhomogeneities. The interactions between flow, heat and mass transfer and catalytic reactions in such highly inhomogeneous packings are of particular interest and subject of this work. High resolution spatial measurements of species and temperature inside the reactor combined with particle resolved CFD modeling of chemistry and flow is a promising approach to understand the physical and chemical processes inside a catalytic n-butane oxidation reactor and provide a methodology for knowledge based optimization of this important industrial process.

This chapter is adopted from submitted manuscript: Y. Dong, M. Geske, O. Korup, N. Ellenfeld, F. Rosowski, R. Horn, What happens in a catalytic fixed-bed reactor for n-butane oxidation to maleic anhydride? Insights from spatial profile measurements and particle resolved CFD simulations. Submitted to Chemical Engineering Journal, 2018.

The conventional way to study catalytic reactions and to test new catalysts in the laboratory is the 'in-out' approach. If concentration and temperature gradients over the catalyst bed are kept small, it is sufficient to analyze what is flowing in the reactor and what comes out of the reactor. A thermocouple inside the catalyst bed delivers a representative temperature value. In pilot scale reactors operating at industrial conversion levels concentration and temperature gradients are naturally pronounced. 'In-out' species analysis and a single temperature reading from the center of the fixed-bed are not sufficient to resolve the gradients occurring inside the reactor. Side sampling ports equipped with thermocouples provide some spatial resolution but the point density in regions of steep gradients is often insufficient and wall effects compromise the representativeness of the measured concentration and temperature values.

In recent years movable capillaries with side sampling orifices have been used to measure species profiles through laboratory fixed-bed reactors with submillimeter resolution [85, 211, 214]. Temperature sensors or spectroscopic fibers placed inside the capillary provide temperature profiles and spectroscopic information about the catalyst [215]. In the present work this methodology has been taken to pilot-scale for the first time. A pilot-scale profile reactor was designed and built for studying n-butane oxidation on vanadyl pyrophosphate (VPP) pellets under industrially relevant conditions. The fixed-bed reactor has the same diameter (D=2.1 cm) as a single tube in an industrial multi-tubular reactor. VPP pellets of industrial dimensions were used as catalyst packing. The catalyst bed was 50 cm in height to keep gas flow rates within bounds.

To interpret the measured species and temperature profiles and to allow for model-based optimization the reactor was modeled by means of particle-resolved three-dimensional computational fluid dynamics (CFD) [28]. A particle-resolved CFD model was chosen over the more common pseudo-homogeneous models because transport correlations in the 'pseudo-' model family become inaccurate in fixed-beds at small D/d ratio (below 10), especially for heat transfer and highly exothermic reactions [24, 98]. Furthermore, pseudo-homogeneous or heterogeneous models are unable to reproduce spikes and dips observed in the experimental profiles due to the very inhomogeneous packing [141] and to separate reaction effects from dead zones or bypass flow.

Several factors affect the prediction performance of CFD simulations of fixed-bed reactors [57]. Besides the computer generated packing and meshing as discussed in Chapter 6. The most important factor is the kinetic model [9]. Most of the published CFD simulation of fixed-bed reactor use microkinetics for surface reactions [80, 117, 121]. The model prediction is sensitive to the value of the active site density and discrepancies between experiment and simulation often result because the active site density of the used catalyst is different from the value in the microkinetic model. Also this parameter is often tuned for the simulations to match the measurements [141].

Microkinetic models consisting of sequences of elementary steps are most reliable for metal catalysts with simple active sites, e.g. single surface atoms or monoatomic steps, and work best at conditions where the mean field hypothesis applies, e.g. at high temperatures. This type of kinetic model has been applied in this work for methane combustion on Pt gauze in Chapter 4 and CO oxidation on Pt loaded foam catalyst in Chapter 5. For n-butane oxidation on vanadium phosphate catalysts no reliable microkinetic model exists. Kinetic models comprising power rate laws and Langmuir-Hinshelwood-Hougen-Watson type rate expressions do exist [216] and seem more applicable to this rather complex catalytic reaction because catalyst properties are lumped together in model parameters which are obtained from fitting the model to kinetic data [217].

Consequently a kinetic model with experimentally determined parameters was used in the present work. The kinetic model augments the widely applied reaction scheme to incorporate acrylic and acetic acid in the network. The kinetic measurements were done with crashed catalyst in a classic kinetic test reactor and delivered intrinsic reaction rates with negligible impact of mass and heat transfer. Since the profile measurements were conducted with full-size catalyst pellets, effectiveness factors had to be introduced into the CFD model to take pore diffusion into consideration [81]. Due to the unknown pore structure of the industrial catalyst pellet, effectiveness factors were adjusted in the kinetic model such that for one set of operation conditions (training set) the predicted temperature and species profiles match the experimental profiles as closely as possible. The model was then used to predict profiles at different operation conditions.

This approach worked well and resulted in a model with predictive power suitable to screen the space for reactor operation parameters that would give a higher maleic anhydride yield. The wall temperature profile was selected for optimization. N-butane oxidation in fixed-bed reactors has been reported to suffer from the development of a hot-spot temperature (max. 60 K) inside the bed [69, 71]. This hot spot shortens the lifetime of the catalyst and promotes the combustion route to CO_2 and CO [76]. By optimizing the wall temperature profile of the reactor hot spot formation could be avoided and the yield to maleic anhydride could be improved.

8.1 Experimental details

Species and temperature profile measurements were carried out in a in-house developed pilot-scale fixed-bed profile reactor. A sketch of the operational principle is shown in Figure 8.1. The reactor tube had an inner diameter of 21 mm and was filled with hollow cylinders of bulk VPP catalyst to a bed height of 50 cm. The industrial VPP reference catalyst was synthesized according to Patent [218] via an organic synthesis route using iso-butanol. A pre-packing (15 cm) of inert Raschig rings was installed to preheat the feed to the desired temperature before it enters the catalyst section. The reactor was equipped with five independent electrical heating zones as shown in Figure 8.1. Each heating zone was 12.5 cm long. The reactor could be operated at pressures up to 5 bar, was fully automized and could run unattended for extended periods of time.

The capillary sampling technique used to measure species and temperature profiles was based on the work of Horn et al. [211] published previously. In brief, a fused silica capillary with a side sampling orifice runs through the center of the catalyst packing. A small amount of the reaction mixture is extracted through the side sampling orifice and sent to a GC for quantitative analysis. A thermocouple inside the sampling capillary, tip aligned with the side sampling orifice and in direct contact with the sampled gases, measures the local gas temperature. By means of a stepper motor, the sampling capillary with the thermocouple inside, can be translated up and down along the centerline axis of the catalyst bed, allowing for simultaneous measurement of species concentration and gas temperature profiles.

Quantitative species analysis was accomplished in two gas chromatographs (Agilent 7890 B) operated sequentially reducing the total measurement time for a full profile to about 7.5 hours. The reactor profiles presented in this work have been measured by feeding 1 % n-butane and 3 % water vapor in synthetic air to the reactor inlet. The total volumetric flow rate was 5.7 ln/min and the reactor pressure was 2 bar.

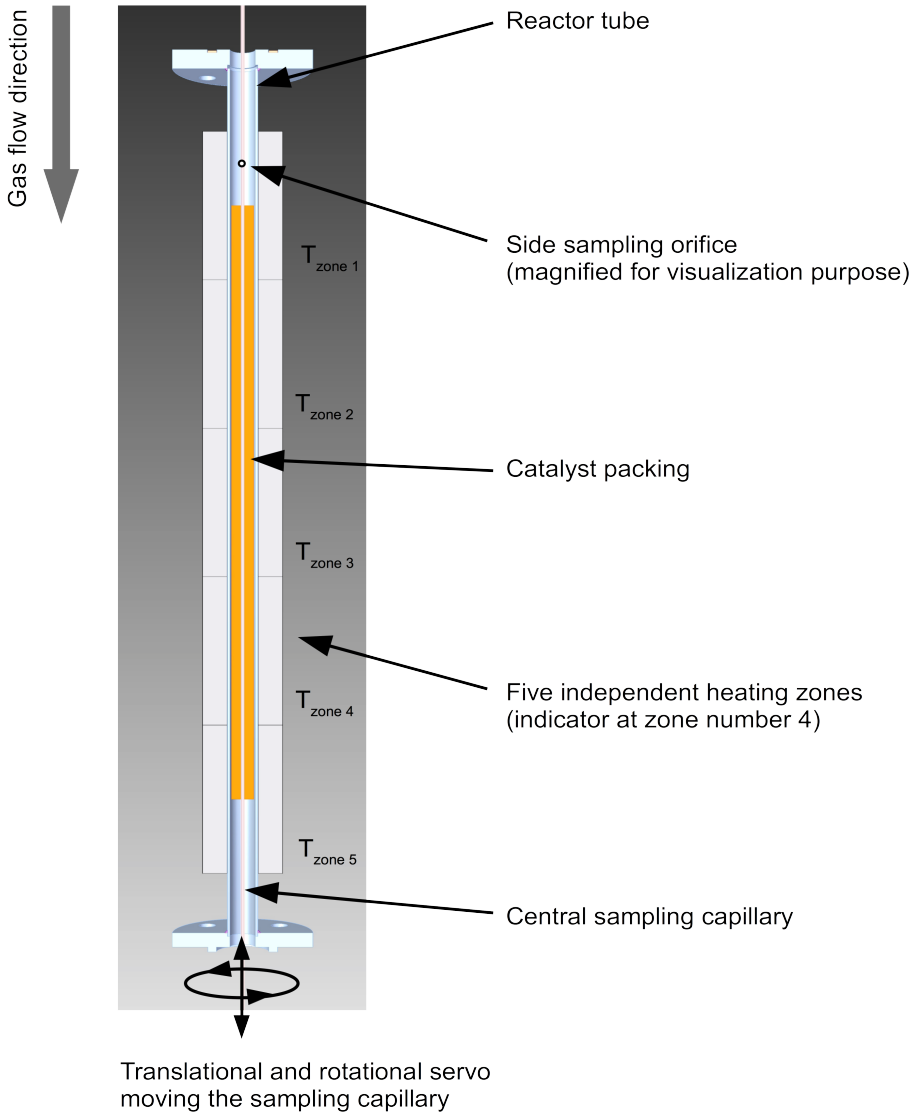

Figure 8.1: Sketch of the pilot-scale fully automated profile reactor.

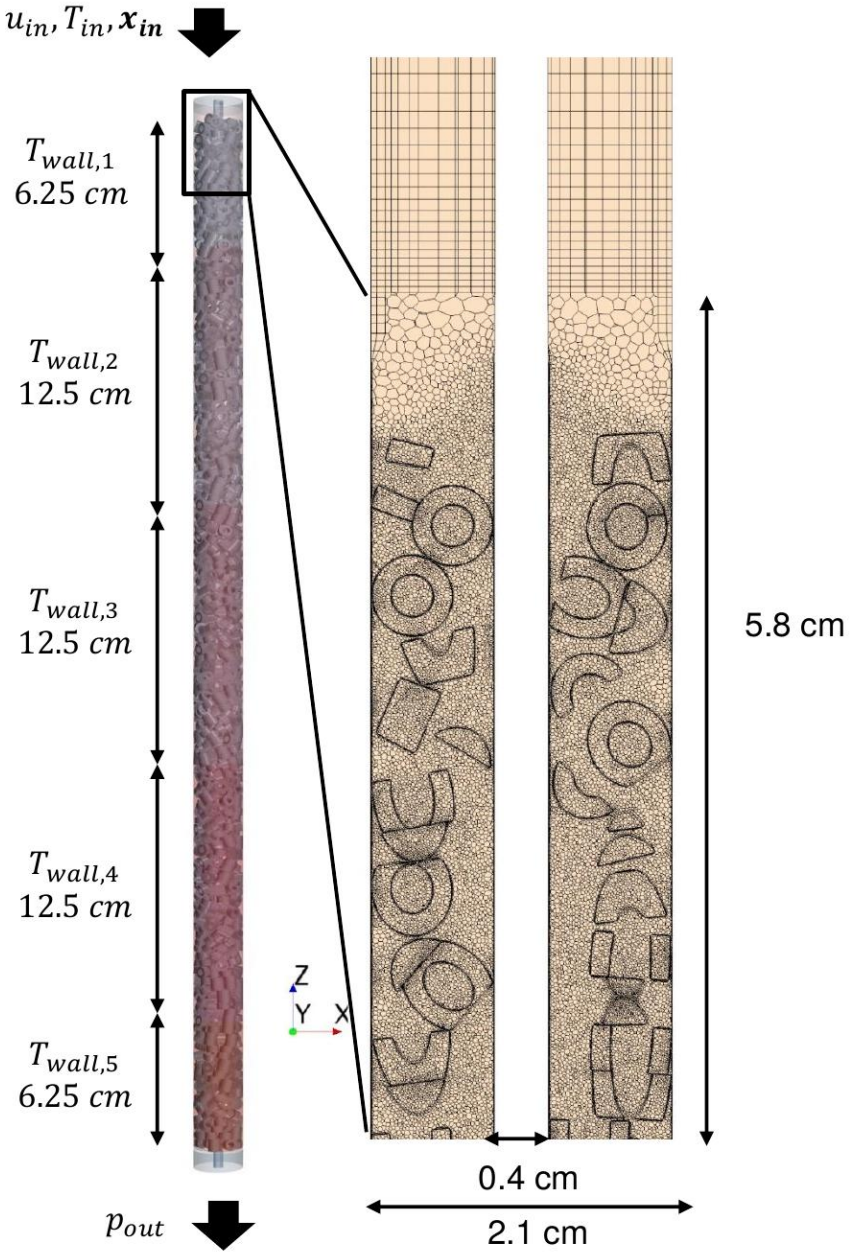

Figure 8.2: Left: Calculation domain and boundary conditions used for particle resolved CFD simulation. Right: translational plane plot of mesh.

8.2 Simulation details

A graphic illustration of the calculation domain is shown in Figure 8.2. DEM simulations (cf. Section 6.2) were used to fill the reactor tube of 21 mm inner diameter with packings of hollow VPP cylinders to a height of 50 cm representing the catalyst bed. In the center of the tube, a cylinder of 4 mm outer diameter represented the sampling capillary. Both, the solid region and the fluid region (voids between the particles) were meshed as shown in Figure 8.2. The pre-packing used in reactor experiments was not considered in the CFD model. It just provided uniform inlet temperature (T_{in}) and inlet velocity (u_{in}) conditions. The inlet temperature was set to the experimental temperature value measured at the entrance of the catalyst packing. It turned out that the feed gas had reached the wall temperature at this point. The inlet flow velocity was calculated from the set experimental volumetric flow rate (5.7 ln/min), inlet temperature and inlet pressure. The inlet gas composition ($\mathbf{x_{in}}$) was 1 % n-butane and 3 % water vapor in air. A pressure boundary condition, set to 2 bar, was used at the outlet. No-slip boundary conditions were applied at the reactor wall and the capillary wall. In terms of temperature boundary conditions, the reactor wall was subdivided into five zones each set to the temperature used experimentally (Figure 8.2, $T_{wall,1}...T_{wall,5}$).

The particle Reynolds number at the studied operation condition is 52 and hence the flow is calculated as laminar with standard governing equations given in Section 3.2.3. All the calculations were carried out at steady state in the CFD software STAR-CCM+ [140]. Since more than 90 % of the gas is air in the studied system, the molecular diffusivity is simplified to the binary diffusivity of each component in air calculated by the Fuller equation [99]. The equations and parameters are given in Eq. 3.8 and Table 3.1.

For most species, the specific heat capacity at constant pressure $c_{p,i}$ was computed from NASA polynomials built-in the thermodynamic database of STAR-CCM+ [140]. For $C_4H_2O_3$, $C_3H_4O_2$ and $C_2H_4O_2$, polynomials are not available and constant values of 1531 J/(kg·K), 1917 J/(kg·K) and 1933 J/(kg·K) respectively were taken from the NIST Chemistry WebBook [219]. The thermal conductivity of the mixture λ was taken as that of air and treated as temperature dependent.

Catalytic reactions were included as boundary conditions at the surface of each catalyst particle (Eq. 3.65). In steady state the diffusional flux of each species normal to the surface was set equal to the catalytic consumption or production rate of the respective species [146] as discussed in Section 3.2.4. To calculate the catalytic consumption/production rate of each species i, the following reactions were considered:

$$C_4H_{10} + 3.5\ O_2 \xrightarrow{r_1} C_4H_2O_3 + 4\ H_2O \tag{8.2}$$

$$C_4H_{10} + (6.5 - 2\ \phi_1)\ O_2 \xrightarrow{r_2} 4\ \phi_1\ CO + 4\ (1 - \phi_1)\ CO_2 + 5\ H_2O \tag{8.3}$$

$$C_4H_2O_3 + (3 - 2\ \phi_2)\ O_2 \xrightarrow{r_3} 4\ \phi_2\ CO + 4\ (1 - \phi_2)\ CO_2 + H_2O \tag{8.4}$$

$$C_4H_{10} + (3.5 - 0.5\ \phi_1)\ O_2 \xrightarrow{r_4} C_3H_4O_2 + \phi_1\ CO + (1 - \phi_1)\ CO_2 + 3\ H_2O \tag{8.5}$$

$$C_3H_4O_2 + (3 - 1.5\ \phi_1)\ O_2 \xrightarrow{r_5} 3\ \phi_1\ CO + 3\ (1 - \phi_1)\ CO_2 + 2\ H_2O \tag{8.6}$$

$$C_4H_{10} + 2.5\ O_2 \xrightarrow{r_6} 2\ C_2H_4O_2 + H_2O \tag{8.7}$$

$$C_2H_4O_2 + (2 - \phi_1)\ O_2 \xrightarrow{r_7} 2\ \phi_1\ CO + 2\ (1 - \phi_1)\ CO_2 + 2\ H_2O \tag{8.8}$$

The stoichiometric coefficients ϕ_1 and ϕ_2 were set to values of 0.556 and 0.5 respectively to match the experimentally observed CO/CO_2 ratio. Power rate laws were used to describe the rate of each of the seven reaction steps.

$$r_1 = k_1 \cdot p_{C_4H_{10}}^{n_1} \cdot p_{O_2}^{n_2} \tag{8.9}$$
$$r_2 = k_2 \cdot p_{C_4H_{10}}^{n_3} \cdot p_{O_2}^{n_4} \tag{8.10}$$
$$r_3 = k_3 \cdot p_{C_4H_2O_3}^{n_5} \cdot p_{O_2}^{n_6} \tag{8.11}$$
$$r_4 = k_4 \cdot p_{C_4H_{10}}^{n_7} \cdot p_{O_2}^{n_8} \tag{8.12}$$
$$r_5 = k_5 \cdot p_{C_3H_4O_2}^{n_9} \cdot p_{O_2}^{n_{10}} \tag{8.13}$$
$$r_6 = k_6 \cdot p_{C_4H_{10}}^{n_{11}} \cdot p_{O_2}^{n_{12}} \tag{8.14}$$
$$r_7 = k_7 \cdot p_{C_2H_4O_2}^{n_{13}} \cdot p_{O_2}^{n_{14}} \tag{8.15}$$
$$k_j = A_j \cdot exp\left(\frac{-E_{a,j}}{RT}\right) \tag{8.16}$$

Reaction orders, activation energies and pre-exponential factors were determined by fitting the rate laws to kinetic measurements which were free of transport artifacts and conducted on crushed and sieved catalyst particles in an isothermal kinetic test reactor. The kinetic experiments covered a temperature range from 360 - 420 °C, a n-butane fraction from 0.5 - 2 %, an O_2 fraction from 15 - 20 % as well as co-feeding 3 % of water vapor. The parameters are given in Table 8.1. Details on the kinetic experiments and model parameter determination will be published in a forthcoming paper [220, 221].

Table 8.1: Kinetic parameters for n-butane oxidation to maleic anhydride developed in house.

A_1	14613	$E_{a,1}$	81740.5	n_1	0.5	n_2	0.42
A_2	43221	$E_{a,2}$	101173	n_3	0.34	n_4	0.37
A_3	4363.3	$E_{a,3}$	86342.2	n_5	0.5	n_6	0.24
A_4	$1.8441 \cdot 10^9$	$E_{a,4}$	155539	n_7	0.83	n_8	0.53
A_5	$1.6959 \cdot 10^9$	$E_{a,5}$	143761	n_9	0.68	n_{10}	0.33
A_6	2.2077	$E_{a,6}$	51545.6	n_{11}	0.63	n_{12}	0.17
A_7	852.07	$E_{a,7}$	91629.1	n_{13}	0.21	n_{14}	0.11
	$mol/(kg \cdot s)$		J/mol		-		-

To convert the molar reaction rates based on mass of catalyst $r_1 - r_7$ to consumption/production rates of each species at the surface of each catalyst particle R_i^{het} in $g \cdot m^{-2} \cdot s^{-1}$, the following equation was used:

$$R_i^{het} = \sum_{j=1}^{7} \nu_{ij} \eta_j r_j \rho_{catalyst} \frac{V_{catalyst}}{S_{catalyst}} M_i \tag{8.17}$$

Eq. 8.17 takes into account that diffusional resistances might exist in the full catalyst pellets used in the profile reactor which are absent in the kinetic measurements on crushed pellets. Hence an internal effectiveness factor η_j is introduced for each reaction step. To convert reaction rates from unit mass of catalyst to unit surface as needed in Eq. 3.65 a conversion factor $\rho_{catalyst} \cdot V_{catalyst}/S_{catalyst}$ is introduced. $\rho_{catalyst}$ is the experimentally determined catalyst density of 1630 kg/m^3. The ratio of pellet volume $V_{catalyst}$ to pellet surface $S_{catalyst}$ was extracted from the mesh. ν_{ij} is the stoichiometric coefficient of species i in reaction j and M_i denotes the molar mass of

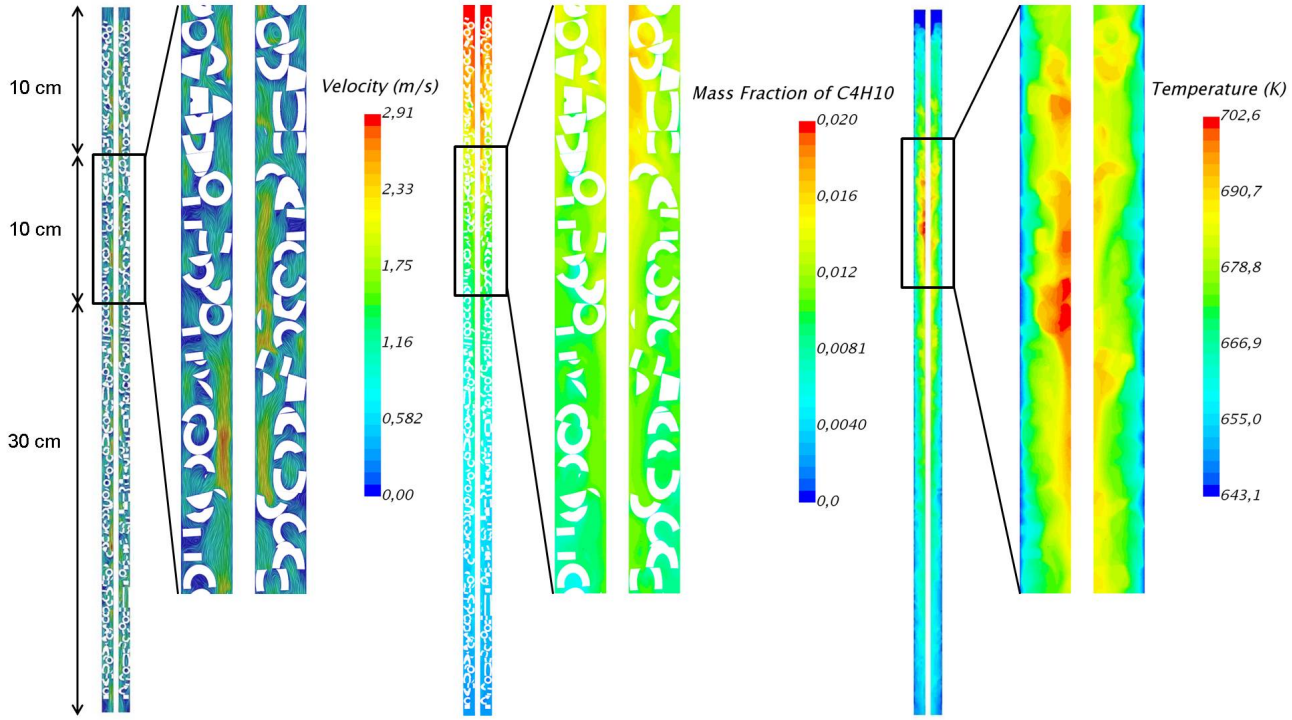

Figure 8.3: Velocity field (left), mass fraction of C_4H_{10} (middle) and temperature field (right) at a uniform reactor wall temperature of 370 °C predicted by particle resolved CFD simulations. The zoomed sections show details around the hot-spot.

species i. The heat generated at each surface element was calculated from

$$Q = R_i^{het} \cdot h_i \tag{8.18}$$

and released to the gas phase and the solid phase by conduction.

8.3 Results and discussion

Cross sections of typical flow, concentration and temperature fields at a uniform reactor wall temperature of 370 °C are shown in Figure 8.3 for a packing height of 50 cm. Pronounced local inhomogeneities are observed in the flow field due to the random arrangement of the catalyst pellets. If the hollow cylinders are oriented perpendicular to the tube axis, dead zones inside and behind them arise with flow velocities close to zero. If the hollow cylinders are oriented parallel to the tube axis, the gas flows through them very quickly. The same holds for gaps in the packing which are often found near the sampling capillary because the space between capillary and tube wall fits only one pellet on average. The temperature and the concentration field in the reactor are very inhomogeneous as well because they result from an interplay between flow velocity, residence time, exothermic reactions and radial heat transfer. Little butane conversion happens in gaps and parallely oriented hollow cylinders due to high flow velocity and short contact time with the catalyst. Zones of low flow velocity, e.g. in perpendicularly oriented hollow cylinders or in the wake of catalyst particles lead to high butane conversion. In the first 10 cm of the tube, the velocity field and the butane mass fraction field are almost a superposition of each other. The high butane concentration due to channelling and the increasing temperature due to the heat of reaction lead to a high reaction rate in the upper half of the catalyst bed forming

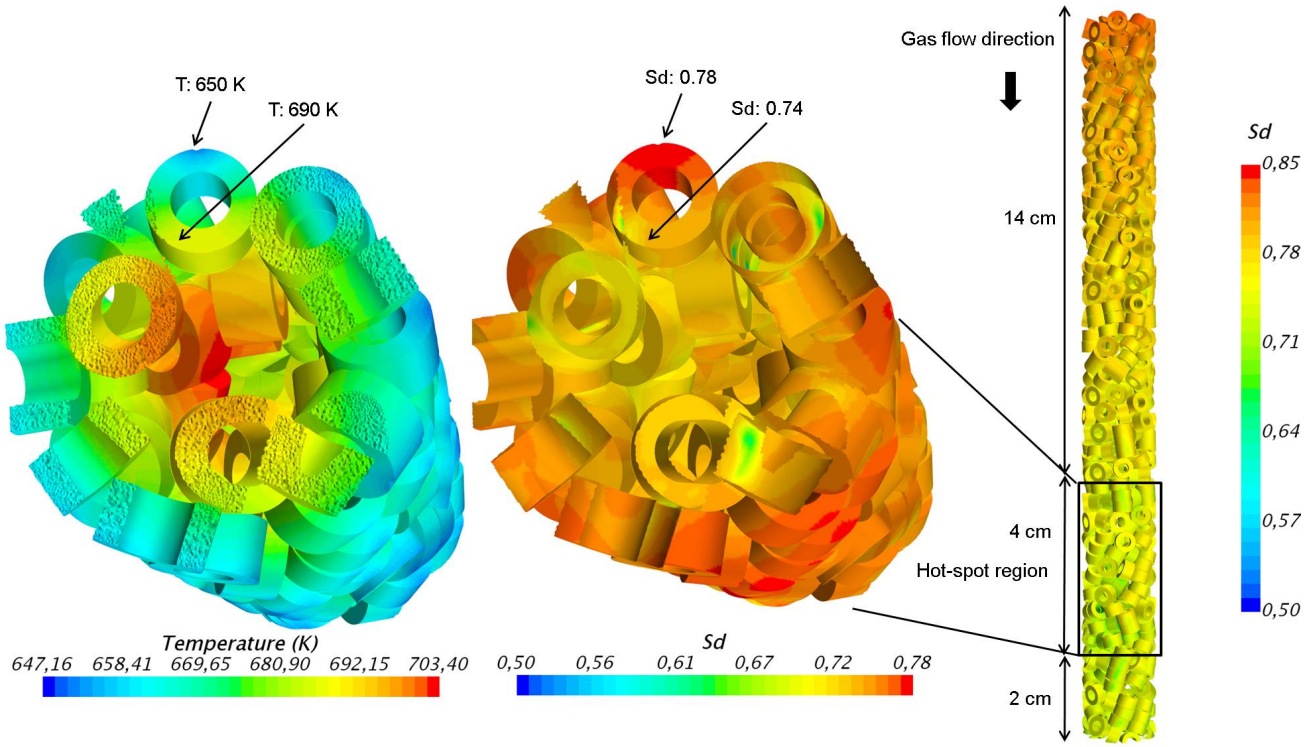

Figure 8.4: Zoomed 3D plot of temperature (left) and differential selectivity according to Eq. 8.19 (middle) of catalyst pellets in the hot-spot of the reactor forming at a uniform reactor wall temperature of 370 °C. The 3D plot on the right side shows the differential selectivity along the first 20 cm of the catalyst packing.

a hot-spot. The hot-spot is locally confined with some pellets exceeding 700 K. In industrial practice, phosphorous compounds are added to the feed to lower catalyst activity, broaden the temperature profile and extend the lifetime of the catalyst [68]. In the second half of the reactor, concentration and temperature gradients become smaller due to the decreasing n-butane concentration and heat removal through the tube wall. Consequently, the catalyst is rather unevenly used in the reactor. Whereas the first half of the bed accounts for about 2/3 of the butane conversion and suffers from thermal stress due to hot-spot formation, the second half of the bed accounts for only 1/3 of the butane conversion and operates almost isothermally at wall temperature level.

Spatial inhomogeneities are not only pronounced on the reactor scale, they are even pronounced on the pellet scale. Figure 8.4 shows two 3D plots of pellets from the hot-spot of the reactor forming between 14 cm and 18 cm inside the catalyst bed if the tube wall temperature is set to 370 °C. Figure 8.4 compares the temperature profile of the pellets with the differential selectivity of n-butane oxidation to maleic anhydride at the surface of each pellet computed according to Eq. 8.19.

$$S_d = \frac{R^{het}_{C_4H_2O_3} \cdot M_{C_4H_{10}}}{|R^{het}_{C_4H_{10}}| \cdot M_{C_4H_2O_3}} \tag{8.19}$$

Temperature differences of 40 K or more exist on one and the same pellet. The side of the pellet pointing inwards has a much higher temperature than the side pointing towards the tube wall. Because high temperatures lead to low selectivity in maleic anhydride formation, temperature differences of several ten Kelvin across a pellet

translate into selectivity differences of several percentage points.

The particle resolved CFD simulations in Figure 8.3 and 8.4 illustrate that conventional pseudo-homogeneous or heterogeneous reactor models would not be able capturing the very inhomogeneous concentration, temperature and velocity field inside this reactor. Both model families treat the catalyst phase as continuum and are not able to resolve gradients caused by the discrete nature of the catalyst particles. Particle resolved reactor simulations reproduce physical reality much better. They would even allow studying the effect of pellet orientation on pressure drop, hot spot formation, product selectivity and yield. Unfortunately, particle resolved CFD simulations are computationally much more expensive than conventional pseudo-homogeneous or heterogeneous models. At the time of this writing, the simulations shown in Figure 8.3 and 8.4 took several weeks on a computational cluster to converge. Nevertheless, computational power is ever increasing and particle resolved reactor simulations might become routine in the not too distant future. To illustrate their potential, a knowledge based manipulation of the reactor wall temperature profile will be presented next.

Training Case: Uniform Reactor Wall Temperature

The kinetic model (Eq. 8.2-8.16, Table 9.1) describes intrinsic reaction rates, free of diffusional resistances. It was measured in a gradient free kinetic test reactor on crushed and sieved catalyst. Used in the particle resolved CFD simulations as is, diffusion limitations inside the VPP hollow cylinders would not be accounted for. Reaction rates would be too high and the model would predict full conversion of n-butane before the end of the packing. Therefore, reaction rate multipliers ($\eta_i \leq 1$) were introduced and multiplied with the pre-exponential factors (A_i in Table 9.1) to decrease the reaction rates. Activation energies and reaction orders were kept constant.

The reactor profiles that were measured with all five heating zones set to 370 °C wall temperature was chosen as 'training set' to determine these multipliers. To check for catalyst deactivation, profile measurements were conducted twice with two months time on stream in between. Measured and simulated species profiles with the reaction rate multipliers $\eta_1 = 1.0$, $\eta_2 = 0.8$, $\eta_3 = 0.6$, $\eta_4 = 1.0$, $\eta_5 = 0.6$, $\eta_6 = 1.0$ and $\eta_7 = 1.0$ are shown in Figure 8.5. These multipliers, lumping besides pore diffusion also effects of film transport and deviations of the DEM packing from the real packing, gave the best fit to the measured species profiles. Another systematic difference between the kinetic measurements leading to Equations 8.2-8.16 and Table 9.1 and data measured in the pilot scale profile reactor is the CO to CO_2 ratio expressed by the parameters ϕ_1 and ϕ_2. In the kinetic measurements, a CO/CO_2 ratio close to 1 was observed ($\phi_1 = 0.556$ and $\phi_2 = 0.5$). All profiles measured in the pilot-scale reactor show a higher CO/CO_2 ratio. Similar findings have been reported in [71]. Hence, the stoichiometric factor ϕ_1 in Equation 8.3, the main source of CO and CO_2, was increased to a value of 0.75 in order to reproduce the measured ratio. Why the CO/CO_2 ratio depends on reactor and catalyst size is not yet clear and requires further investigations.

Another parameter that was determined from the training data set was the thermal conductivity of the catalyst pellets. The only value reported in the open literature is 0.585 W/m/K [222]. Figure 8.6 shows a screening study on this parameter using a slightly shorter catalyst bed of 30 cm length to save computational time. If the original value of 0.585 W/m/K is used, the hot-spot is markedly overpredicted. Best agreement was found with a value of 1.2 W/m/K which was then used in all simulations discussed hereafter.

The experimental profiles in Figure 8.5 are very reproducible taking into account that they were measured with two months time-on-stream in between. The spikes

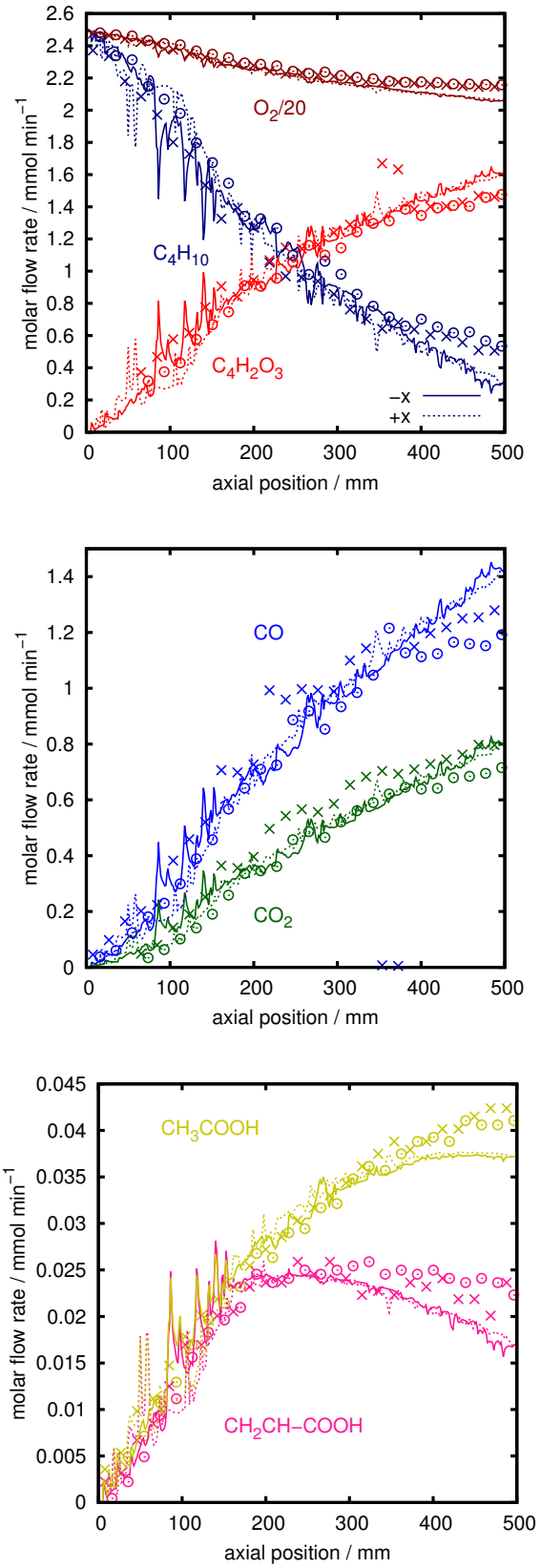

Figure 8.5: Measured (points) vs. simulated (lines) species profiles. All five heating zones were set to 370 °C. Simulation results are displayed from two axial trajectories extracted at the same radial distance from the tube center but opposite azimuthal angle (solid lines, dotted lines). Profile measurements were repeated twice with two months time on stream in between (two types of symbols).

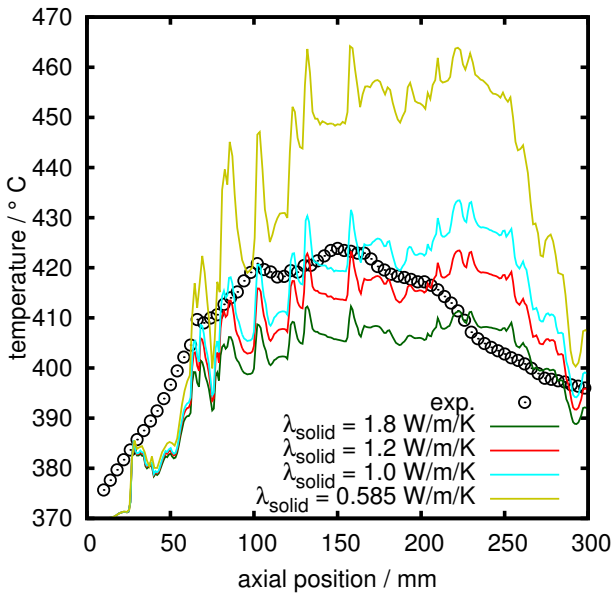

Figure 8.6: Effect of the thermal conductivity of the solid (λ_{solid}) on the simulated temperature profiles. The experimental temperature profile corresponds to the case where all five heating zones were set to 370 °C.

and dips in the experimental data are real and no scatter. They are caused by the random orientation of the catalyst pellets in the reactor and the local flow, temperature and concentration conditions around the sampling orifice. This can be seen best by analyzing simulation data which are free of experimental scatter. The solid and dotted lines in Figure 8.5 correspond to two simulated axial species profiles extracted at the same radial distance from the tube center but opposite azimuthal angles. The spikes and dips in the simulated profiles are even more pronounced than in the measured profiles because sampling through the orifice, which had a diameter of 100 μm in this study, averages over a finite volume smoothing the amplitudes to some extent.

A similar comparison is shown in Figure 8.7 for the temperature profiles. The simulated temperature profiles are sampled at four axial trajectories around the central sampling capillary at the same radial distance from the tube center but at four different azimuthal angles $+x = 0, -x = \pi, +y = \pi/2, -y = 3/2\pi$. There is a qualitative agreement among the four simulated temperature profiles in terms of hot-spot position and slopes before and after the hot-spot. Quantitatively the simulated temperature profiles differ slightly due to the random orientation of the particles. For example, the hot-spot temperature varies by up to 18 K among the four simulated profiles shown.

Deviations between simulated and measured profiles are easier spotted if the simulated profiles are angular averaged as shown in Figure 8.8 for the species profiles. Systematic deviations from the measurements are found for all species from 350 mm to 500 mm. This is most likely caused by the slightly over-predicted temperature in this section (cf. Figure. 8.7) leading to a higher consumption rate of n-butane and a higher production rate of the reaction products.

Eye-catching different profiles, both measured and simulated, were observed for the two acids, acetic acid CH_3COOH and acrylic acid $CH_2CH\text{-}COOH$. Acetic acid is formed along the entire catalyst bed. Acrylic acid is formed at the same rate as acetic acid up to about $z \approx 150$ mm, the location of the hot-spot. At this point, acrylic acid formation stops. From 150 mm to about 280 mm the molar flow rate of acrylic acid

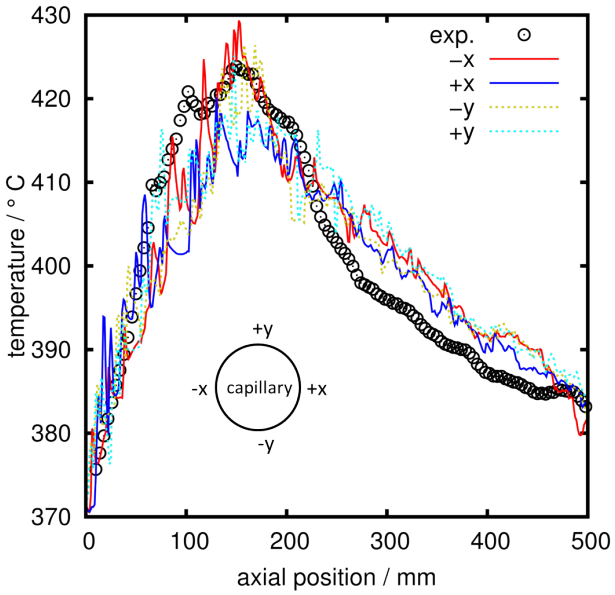

Figure 8.7: Measured (points) vs. simulated (solid and dotted lines) temperature profiles. All five heating zones were set to 370 °C. Simulated temperatures are displayed for four axial trajectories extracted at the same radial distance from the tube center but four different azimuthal angles ($+x = 0, -x = \pi, +y = \pi/2, -y = 3/2\pi$).

stays almost constant. From 280 mm onwards, the acrylic acid profile goes down until the end of the catalyst bed at 500 mm. In this zone, the production rate of acrylic acid is negative.

The molecular details of this different behaviour are not yet clear but the development of the two acids is nicely captured by the kinetic model (Eq. 8.2-8.16, Table 9.1). According to this reaction network, the formation rate of CH_3COOH is $2 \cdot r_6 - r_7$ and that of $CH_2CH\text{-}COOH$ is $r_4 - r_5$. Figure 8.9 plots these reaction rates along the bed. The reaction rates producing and consuming acrylic acid, r_4 and r_5 respectively, follow the temperature profile closely. This is due to the high values of the activation energy of these two reactions ($E_{a,4} = 156$ kJ $\cdot$ mol^{-1}, $E_{a,5} = 144$ kJ $\cdot$ mol^{-1}). Downstream of 300 mm, the value of r_4 becomes lower than that of r_5 explaining the slow decrease of the $CH_2CH\text{-}COOH$ profile. The reaction rates producing and consuming acetic acid, r_6 and r_7 respectively, have lower activation energies ($E_{a,6} = 52$ kJ$\cdot$mol^{-1}, $E_{a,7} = 92$ kJ $\cdot$ mol^{-1}) and are less sensitive to temperature variations. The net formation rate of acetic acid, $2 \cdot r_6 - r_7$ decreases along the catalyst bed but never becomes negative. In consequence, the molar flow rate of acetic acid increases monotonously along the reactor but flattens in slope.

Predictive Case: Staged Reactor Wall Temperature

After 'training' the kinetic model to match the measured reactor profiles as closely as possible at a uniform wall temperature of 370 °C, predictions were made for other reactor wall temperatures and compared with measurements. Because a uniform reactor wall temperature of 370 °C led to a non-acceptable hot-spot of about 425 °C, the temperature of all five heating zones was lowered to 360 °C. The corresponding temperature and species profiles are provided in Figure 8.11 and Figure 8.10. Agreement between experiment and simulation is still good. The hot-spot temperature in

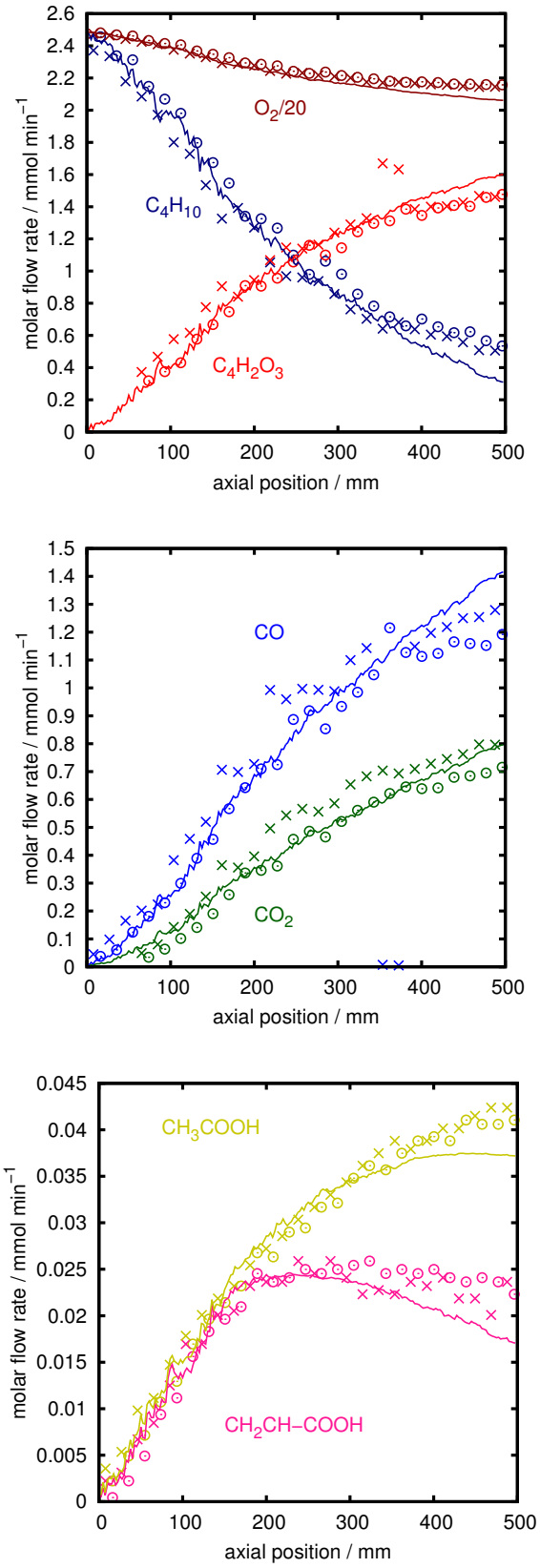

Figure 8.8: Angular averaged simulated species profiles (lines) vs. measured species profiles (symbols). The measured species profiles correspond to two measurements along the same axial trajectory but with two months time on stream in between. All five heating zones were set to 370 °C.

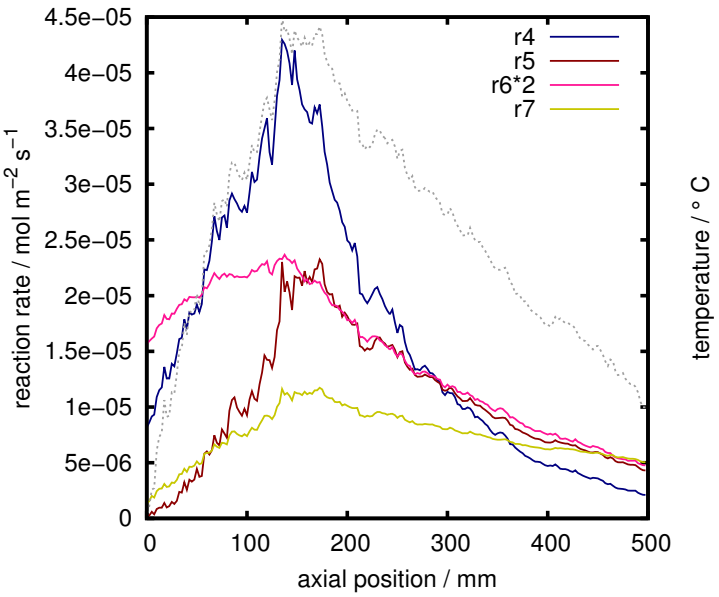

Figure 8.9: Angular averaged simulated reaction rates related to acetic acid CH_3COOH and acrylic acid $CH_2CH\text{-}COOH$. All five heating zones were set at 370 °C. The grey dotted line shows the simulated temperature profile for comparison.

the catalyst bed is reduced disproportionately due to the parametric sensitivity of the system ($T_{meas}^{max} \approx 397$ °C, $T_{sim}^{max} \approx 392$ °C). The reduced temperature in the reactor lowers the thermal stress on the catalyst which is desirable but it also lowers reaction rates and leads to reduced maleic anhydride production which is not acceptable from an industrial point of view. Lowering the reactor wall temperature along the entire reactor is therefore not an option.

Without knowledge of the concentration and temperature profiles inside the reactor and without a predictive reactor model time consuming and costly trial and error campaigns would now be in order to reduce the thermal stress on the catalyst without compromising maleic anhydride production. With the knowledge from the profile measurements and with the predictive model, knowledge based reactor optimization allows reaching this goal faster and cheaper. At 370 °C reactor wall temperature the profiles showed a detrimental hot-spot formation in the first half of the catalyst bed because high butane concentrations meet hot catalyst particles. As described above 2/3 of the butane was converted under these conditions in the first half of the catalyst bed while the second half only accounted for 1/3 of the overall butane conversion. This knowledge implies that an optimum reactor wall temperature profile features gradually increasing temperatures with lower temperatures and reduced reaction rates at the reactor inlet and higher temperatures towards the outlet compensating for the decreasing butane concentration. The predictive reactor model can now be used to calculate an optimized wall temperature profile according to this general strategy.

To demonstrate this concept, Figure 8.12 shows a side-by-side comparison of experimental and computed reactor profiles for the 'training' case of 370 °C uniform reactor wall temperature on the left side and a stagewise increasing wall temperature profile on the right side. For the staged profile the heating zones 1-5 were set to $T_{wall,1} = 360$ °C, $T_{wall,2} = 365$ °C, $T_{wall,3} = 370$ °C, $T_{wall,4} = 375$ °C and $T_{wall,5} = 380$ °C respectively. For better comparison of reactor performance, the profiles in Figure 8.12 are plotted as conversion profiles for n-butane (C_4H_{10}) and selectivity profiles for the main products

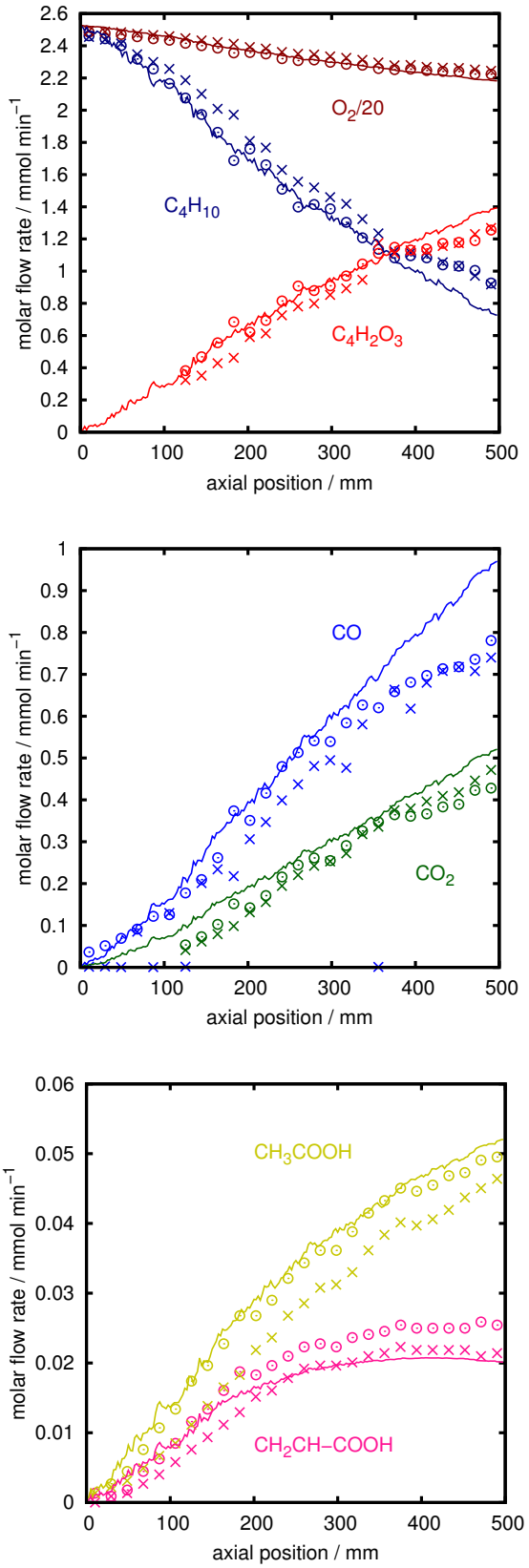

Figure 8.10: Angular averaged simulated species profiles (lines) vs. measured species profiles (symbols). The measured species profiles correspond to two measurements along the same axial trajectory but with two months time on stream in between. All five heating zones were set to 360 °C. Experiments were repeated twice and indicated by two types of symbols.

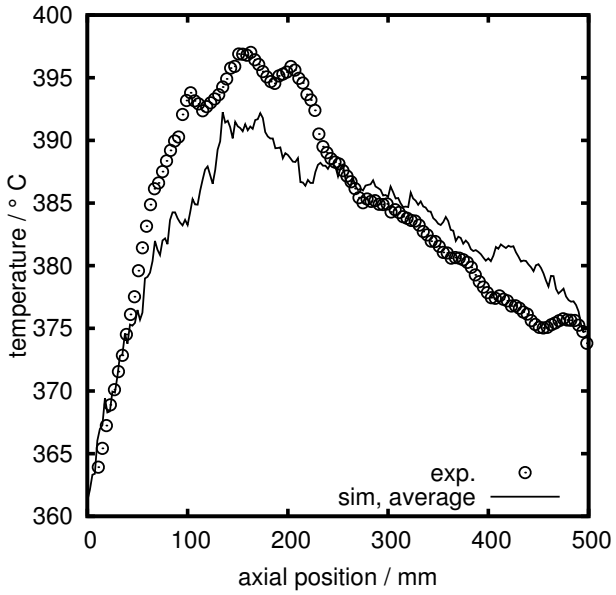

Figure 8.11: Comparison of the measured center line reactor temperature profile (points) with the angular averaged simulated temperature profile (line). All five heating zones were set to 360 °C.

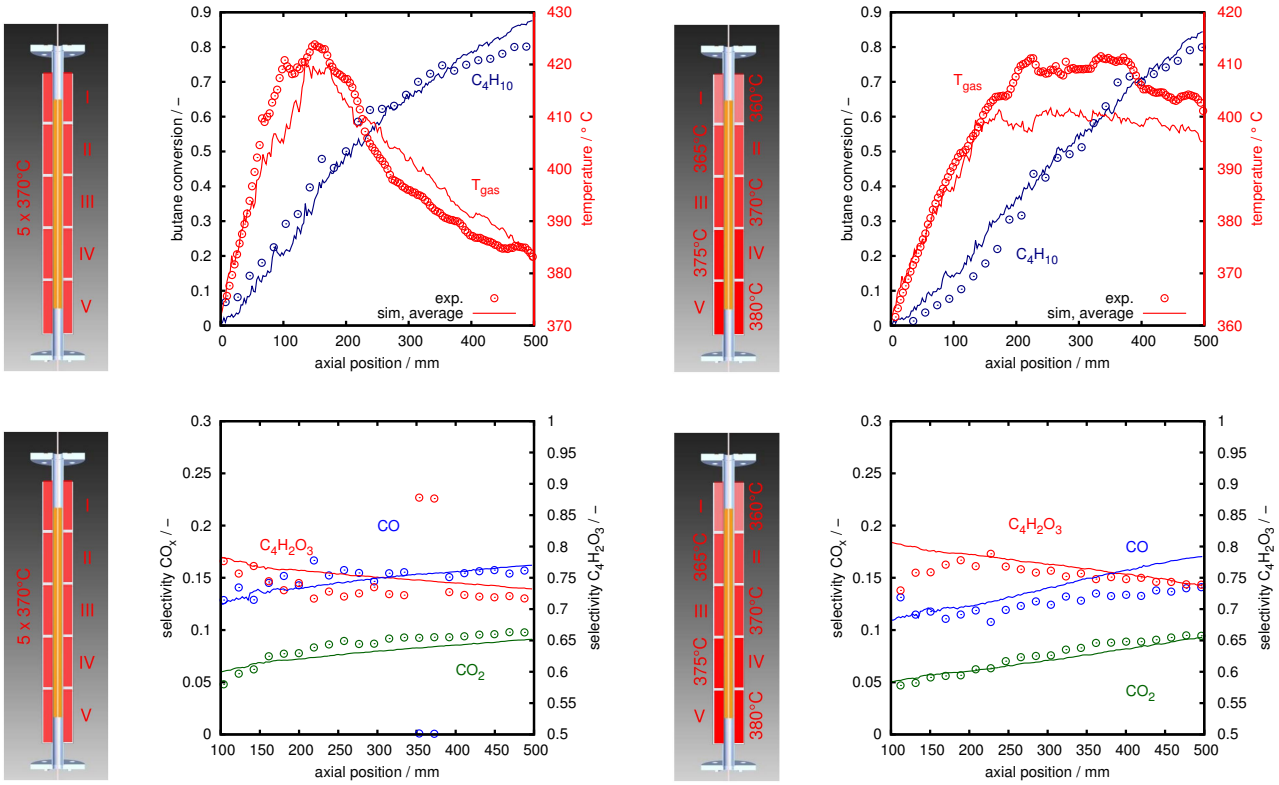

Figure 8.12: Comparisons of the simulated (line) and measured (points) conversion, selectivity and temperature profiles. Left: five heating zones are set uniform at 370 °C. Right: five heating zones are set stepwise increase from 360 °C to 380 °C. Simulation results are circumferentially averaged. The applied reactor wall temperature settings are show as sketch.

maleic anhydride ($C_4H_2O_3$), carbon monoxide (CO) and carbon dioxide (CO_2).

In both cases a butane conversion of about 80 % was measured at the end of the catalyst bed. This conversion level is comparable to industrial reactors. In case of the stagewise increasing wall temperature profile the butane conversion rate is indeed reduced in the first half of the catalyst bed and increased in the second half of the catalyst bed. As intended, this leads to a more uniform temperature profile inside the catalyst bed without punctual hot-spot formation. The temperature increases almost linearly from the inlet value of 360 °C at 0 mm to 410 °C at about 220 mm, staying constant up to about 380 mm before decreasing to 400 °C at the end of the catalyst bed (500 mm). The differences to the 370 °C wall temperature case seem subtle but an inspection of the selectivity profile shows that not only the thermal stress of the catalyst is reduced but that also the selectivity to maleic anhydride is increased. This comes as no surprise because the detrimental influence of high catalyst temperatures on the maleic anhydride selectivity was already seen in Figure 8.4. While the measured integral maleic anhydride selectivity is about 72 % for a uniform wall temperature of 370 °C, the stagewise increasing wall temperature profile increases the measured integral maleic anhydride selectivity to almost 75 %. This increase seems minor but at a world scale production of 2.8 Mio t it translates into significant savings in n-butane consumption, reduced CO_x emissions and increased revenue [79].

8.4 Conclusions

We present for the first time species and temperature profiles inside a pilot-scale fixed-bed reactor for n-butane oxidation on VPP catalyst pellets under industrially-relevant temperature-, flow- and pressure conditions. Besides high resolution profiles for the main species n-butane, oxygen, maleic anhydride, CO and CO_2 profiles of the intermediates/by-products acetic acid (CH_3COOH) and acrylic acid (CH_2CH-$COOH$) were measured. The species and temperature profiles provide insight into the reaction network and lead to strategies for reactor optimization. For optimization of the reactor wall temperature profile, the pilot-scale profile reactor was equipped with five independent heating zones offering the possibility to imprint a temperature profile onto the reactor wall.

To make predictions of the reactor performance at different operation conditions, a particle-resolved CFD reactor model was developed. Classical pseudo-homogeneous or heterogeneous reactor models would not be able to capture the very inhomogeneous velocity-, temperature- and concentration fields inside the catalyst bed because the large catalyst pellets inside the narrow reactor tube cannot be approximated as one continuous phase. The packing structure generated from DEM simulations was found to be in very good agreement with the experimentally determined porosity profile. Close to the reactor wall agreement was almost perfect due to the ordering effect of the wall. In the tube center measured and simulated porosity profiles agreed within the statistical bounds of the packing process. The influence of the central sampling capillary on the packing was also well captured by the DEM simulations.

The catalytic reactions inside the catalyst pellets were described by an intrinsic kinetic model, measured on crushed and sieved catalyst particles in a separate kinetic setup under conditions free of transport artifacts. Because it was computationally not possible to solve reaction-diffusion equations in each catalyst pellet on top of the already very demanding CFD simulations, reaction rate multipliers were introduced in the kinetic model lumping transport effects and minor deviations between the simulated and the real catalyst packing. These reaction rate multipliers were determined by

changing them until the best possible agreement with a set of reactor profiles measured at a uniform reactor wall temperature of 370 °C was reached. The trained model was then used to make predictions for the reactor profiles at other wall temperature conditions and good agreement was found with the corresponding measurements. Particle resolved CFD reactor modeling suggested a stagewise increasing temperature with increments of 5 °C from 360 °C to 380 °C as close to optimum. When this temperature profile was imprinted onto the reactor wall, the hot-spot was indeed eliminated, conversion remained at 80 % and the integral selectivity to maleic anhydride at the end of the catalyst bed increased from 72 % to almost 75 %. The reduced thermal stress on the catalyst extends the lifetime of the VPP catalyst and the increasing selectivity to maleic anhydride at constant n-butane conversion translates into a better use of the feedstock n-butane, reduced CO_x emissions and higher revenue.

This work demonstrates the potential of combining spatial reactor measurements with appropriate reactor modeling to improve even well established catalytic processes. The oxidation of n-butane to maleic anhydride on vanadyl pyrophosphate was chosen as test reaction in this work but this approach can be extended to all heterogeneous catalytic reactions carried out in fixed-bed reactors.

"Catalyst particles have a very complicated pore structure and describing diffusion from the external surface to the active sites where the reactions take place is not a simple task."

Gilbert F. Froment et al.[2]

9 Catalyst Pore Structure Study

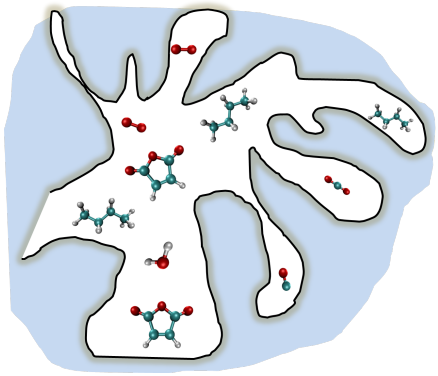

Most applied vanadyl pyrophosphate (VPP) catalysts for n-butane oxidation to maleic anhydride (MA) in industrial fixed-bed reactors are bulk catalysts typically made by pressing the active powder into a pellet with the desired dimensions [91]. The resulting catalyst pellets therefore have a bimodal pore structure, i.e. the micro-porous structure from the chemical synthesis of the active powder and the macro-porous region between the powder formed by the pelleting process. Due to diffusion limitation, the global reaction rate of the catalyst pellet in the reactor can be different from the intrinsic reaction rate measured for the active powder [71]. Hence, the real performance of the VPP catalyst pellet in a technical fixed-bed reactor is an overall result of the chemistry nature of the active component and the pore structure of the pellet. Most of current research on n-butane oxidation focus on improving the catalytic chemistry of the VPP catalyst [72, 223, 224]. New synthesis methods are continuously proposed to increase the intrinsic activity of the VPP precursors [75, 225]. To the best of our knowledge, the pore structure optimization of the VPP catalyst for n-butane oxidation is not explored yet.

Early studies have shown that an optimal pore structure of the catalyst pellet can be of great importance [226–228]. With the development of experimental techniques, rational design and synthesis of catalyst pellets with desired pore structure for better performance is nowadays possible [229, 230]. The effect of the pore structure parameters of the VPP catalyst pellet on the reactor performance for n-butane oxidation in a fixed-bed reactor is investigated in this work by means of detailed mathematical modelling. If the overall yield of maleic anhydride can be improved by 1 % with altering the catalyst pore structure, this may open up a new direction for research of this process.

9.1 Simulation details

A two-dimensional heterogeneous model [2] including mass, heat and momentum balances in both axial and radial direction were applied to model a fixed-bed reactor. The

This chapter is adopted from publication: Y. Dong, F.J. Keil, O. Korup, F. Rosowski, R. Horn, Effect of the catalyst pore structure of fixed-bed reactor performance of partial oxidation of n-butane: A simulation study, Chemical Engineering Science 142 (2016) 299-309.

three-dimensional reactor was simplified to a two-dimensional rectangular geometry assuming rotational symmetry. The pseudo-homogeneous and heterogeneous models have been applied successfully to simulate the n-butane oxidation in fixed-bed reactors [71, 222, 231–233] and membrane reactors [78, 234, 235]. The micro- and macro pore model of Wakao and Smith [92, 131] was applied for describing diffusion-reactions inside the porous catalyst pellet. Details of the models are described in Section 3.1. All the simulations were carried out with COMSOL Multiphysics 5.0® [236].

For this simulation work, the triangle (three-reaction) network as shown in Figure 9.1 was used which includes the main reaction of n-butane to maleic anhydride, total oxidation of n-butane to carbon oxides (CO_2 and CO) and consecutive MA oxidation to CO_2 and CO [237]. The formation of other by-products such as acetic acid, acrylic acid, phthalic and methacrylic acids are generally neglected in the reaction model because of observed low concentrations (lower than 2 %) [78, 234].

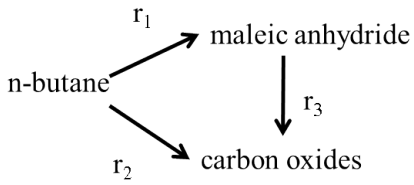

Figure 9.1: Triangle reaction network for n-butane oxidation [237].

The stoichiometric equations used were as follows:

$$C_4H_{10} + 3.5\ O_2 \xrightarrow{r_1} C_4H_2O_3 + 4\,H_2O \quad \Delta H^{\circ}_{R,298K} = -1240\ \text{kJ/mol} \tag{9.1}$$

$$C_4H_{10} + 5.5\ O_2 \xrightarrow{r_2} 2\,CO_2 + 2\,CO + 5\,H_2O \quad \Delta H^{\circ}_{R,298K} = -2092\ \text{kJ/mol} \tag{9.2}$$

$$C_4H_2O_3 + 2\,O_2 \xrightarrow{r_3} 2\,CO_2 + 2\,CO + H_2O \quad \Delta H^{\circ}_{R,298K} = -852\ \text{kJ/mol} \tag{9.3}$$

The intrinsic rate expressions and kinetic parameters were taken from Guettel et al. [233], and the parameters are given in Table 9.1:

$$k_j = A_j \cdot exp\left(\frac{-E_{a,j}}{RT}\right) \tag{9.4}$$

$$r_1 = \frac{k_1 p_{C_4H_{10}} p_{O_2}^{0.5}}{1 + K_1 p_{C_4H_{10}} + K_2 p_{H_2O}} \tag{9.5}$$

$$r_2 = \frac{k_2 p_{C_4H_{10}} p_{O_2}^{0.5}}{1 + K_1 p_{C_4H_{10}} + K_2 p_{H_2O}} \tag{9.6}$$

$$r_3 = \frac{k_3 p_{C_4H_2O_3} p_{O_2}^{0.25}}{1 + K_1 p_{C_4H_{10}} + K_2 p_{H_2O}} \tag{9.7}$$

Since the aim of the present simulation is to investigate the effect of the pore structure of the catalyst pellet on the reactor performance, the above mentioned reaction rates r_j which are in units of mol/(kg_{cat}· s) were converted to the surface area based reaction rate $r_{j,s}$ which is in units of mol/ (m^2· s) with assumed active surface per catalyst mass S_g of 6.7 ·10^5 m^2/kg.

The shape of the catalyst pellet studied in the present paper is cylindrical ($d = h = 3$ mm) and physical parameters of the catalyst were adapted from Guettel et al.

Table 9.1: Kinetic parameters for partial oxidation of n-butane taken from Guettel et al. [233]

Parameter	Value	Unit
A_1	1.28	mol/ $(s \cdot kg_{cat} \cdot Pa^{1.5})$
A_2	15.1	mol/ $(s \cdot kg_{cat} \cdot Pa^{1.5})$
A_3	0.26	mol/ $(s \cdot kg_{cat} \cdot Pa^{1.25})$
$E_{a,1}$	114	kJ / mol
$E_{a,2}$	132	kJ / mol
$E_{a,3}$	97	kJ / mol
K_1	$6.8 \cdot 10^{-4}$	1/Pa
K_2	$5.8 \cdot 10^{-4}$	1/Pa

Table 9.2: Properties of the catalyst pellet [222, 233].

Property	Symbol	Value	Unit
Mean macro pore diameter	d_M	100	nm
Mean micro pore diameter	d_m	1	nm
Total porosity	ε_{total}	0.5	-
Macro pore porosity	ε_M	0 - 0.5	-
Micro pore porosity	ε_m	0 - 0.5	-
Density of the solid	ρ_{solid}	3000	kg/m^3
Thermal conductivity of the pellet	λ_{pellet}	0.585	W/(m·K)

[233]. Due to the limited published information on the available pore structure of this catalyst, parameters d_M, d_m, ε_M were estimated. The estimated physical properties for the reference case are listed in Table 9.2.

9.2 Results and discussion

In the first part of this section, the obtained reactor profiles and pellet profiles simulated are discussed. A reference case was defined with the pellet pore structure parameters set to: $\varepsilon_M = \varepsilon_m = 0.25$, $d_M = 100$ nm, $d_m = 1$ nm. The operational parameters of the reactor are summarized in Table 9.3.

Figure 9.2 shows the typical velocity field and temperature profile inside the fixed-bed reactor simulated with the heterogeneous model. The flow field predicted by the extended Brinkmann equation together with the radial porosity profile and Ergun correlation shows maximum values in the near-wall region and zero value at the wall [78]. This is caused by the high porosity of the random packing in the vicinity of the wall and no-slip boundary condition applied at the wall. Detailed flow calculations, instead of using conventional plug-flow assumption, are important in this study due to the strong interconnection between the flow and the heat and mass transport. This coupling is described by the 'λ_r model' of Winterberg and Tsotsas [97] applied in this work. For a strong exothermic reaction in wall-cooled fixed-bed reactors with low D/d ratio, the accurate prediction of the hot spot temperature is of vital importance

Table 9.3: Operational parameters applied in a two-dimensional heterogeneous model to simulate n-butane oxidation in a fixed-bed reactor.

Parameter	Symbol	Value	Unit
Reactor length	l_R	0.5	m
Reactor diameter	d_R	21	mm
Inlet temperature	T_0	673.15	K
Reactor wall temperature	T_w	673.15	K
Inlet molar fraction of C_4H_{10}	$y_{C_4H_{10},0}$	0.02	-
Inlet molar fraction of O_2	$y_{O_2,0}$	0.2	-
Inlet molar fraction of H_2O	$y_{H_2O,0}$	0.03	-
Gas hourly space velocity	GHSV	2000	h^{-1}

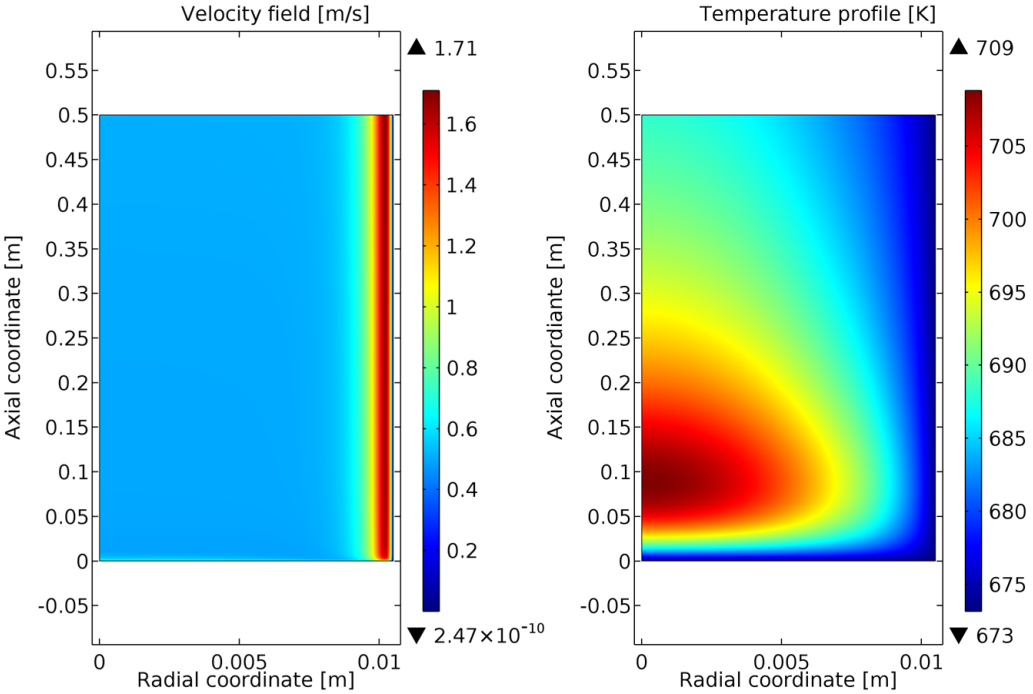

Figure 9.2: Example illustration of the predicted velocity field (left), temperature profile (right) of a 2-D heterogeneous model incorporated with radial porosity profile and exothermic reactions.

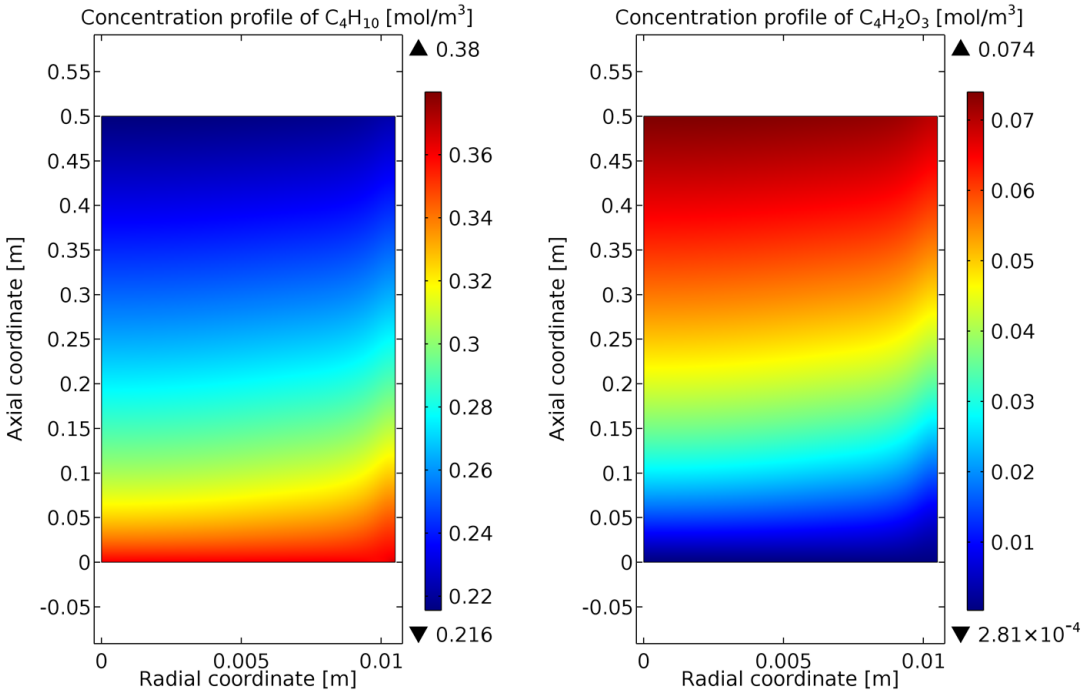

Figure 9.3: Predicted concentration profile for C_4H_{10} (left) and $C_4H_2O_3$ (right) of the reference case.

[208]. This is the reason why a two-dimensional model is necessary to follow the pronounced radial temperature profile and capture the exact location and magnitude of the hot spot. The accuracy of the 'pseudo-' family model is heavily dependent on the reliability of the effective transport parameters especially for the radial heat transport [98]. A wrongly calculated temperature profile affects the concentration profile via the exponential term in the reaction kinetics. Also, the hot spot temperature is a critical value to check while evaluating the results owing to varying pore structure parameters. A too high hot spot temperature is not only dangerous for the operation (run-away), but also has negative effect on the selectivity and life-time of the catalyst [234].

Figure 9.3 shows the simulated concentration profiles of C_4H_{10} and $C_4H_2O_3$ for the reference case. Concentration of C_4H_{10} decreases while $C_4H_2O_3$ increase along the axial direction with reactions proceed along the reactor. No large radial concentration gradients are observed for both species concentration profiles. The slightly higher concentrations of C_4H_{10} and $C_4H_2O_3$ near the wall compared to the center are caused by lower temperature and higher flow rate near the wall.

The heterogeneous model calculates the source term at each point of the reactor from the pellet mass balance. Therefore, one can plot the profiles inside the pellets at every point (r and z coordinate) in the reactor. For illustration purposes, five sampling points at position 1 ($r = 0$ m, $z = 0.1$ m), position 2 ($r = 0$ m, $z = 0.25$ m), position 3 ($r = 0$ m, $z = 0.4$ m), position 4 ($r = 5.25 \cdot 10^{-3}$ m, $z = 0.1$ m) and position 5 ($r = 10.5 \cdot 10^{-3}$ m, $z = 0.1$ m) were taken. Figure 9.4 shows the concentration profiles of selected species and temperature profile inside the pellet at the five sampling points in the reactor. All species participating in the reaction show intra-particle concentration gradients. The temperature gradients are negligible. This behaviour can also be found in literature [2]. The concentration gradient indicates the presence of diffusion-reaction interplay with the pore structure chosen for the reference case. By comparing the concentration plots in position 1,2,3 which are at

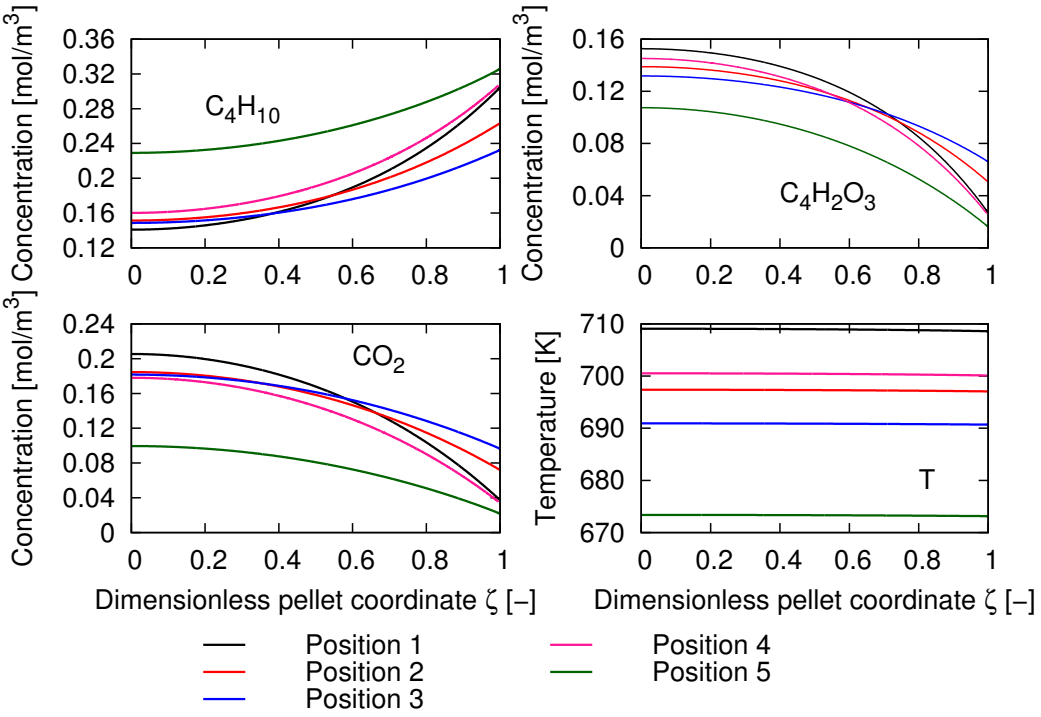

Figure 9.4: Concentration profiles of C_4H_{10} (left top), $C_4H_2O_3$ (right top), CO_2 (left bottom) and temperature profile (right bottom) inside the pellet at five sampling positions in the reactor. Position 1: $r = 0$ m, $z = 0.1$ m; Position 2: $r = 0$ m, $z = 0.25$ m; Position 3: $r = 0$ m, $z = 0.4$ m; Position 4: $r = 5.25 \cdot 10^{-3}$ m, $z = 0.1$ m; Position 5: $r = 10.5 \cdot 10^{-3}$ m, $z = 0.1$ m.

different axial positions but same radial position, one can see that the concentration profiles inside the pellet change considerably along the reactor. With the progress of reaction, the concentration gradient is flattened as expected. The flattened profiles along the reactor are a sign for the decreasing reaction rates along the bed due to lower concentration of the reactants and decreasing temperature along the bed.

If the entire reactor for n-butane oxidation is packed with the same catalyst material, one can image that the catalysts in the lower part of the bed are not used as efficiently as at the bed inlet [72]. From an economic point of view, a more structured catalyst packing where catalysts with different kinetics are packed at different sections of the reactor may be a good approach [233]. Position 1,4,5 are taken from the same axial coordinate but different radial coordinate. One can observe rather different concentration profiles inside the pellet. Position 1 is almost in the hot-spot region as one can see in the temperature plot and that may explain the higher concentration gradient with higher reaction rates. Figure 9.3 and Figure 9.4 show that the catalyst pellet located in different sections of the reactor may experience different conditions (concentration of the reactants and temperature). It is possible that these catalysts are chemically different from each other especially on the surface in accordance to the exposed conditions. In future work, incorporation of the surface dynamics in the model can be an insightful refinement of the model.

In total, there are four pore structure parameters in the model of Wakao and Smith [92] which can be varied or optimized. In the presented study, only three parameters were studied since the total porosity of the catalyst pellet was kept fixed to 0.5. By

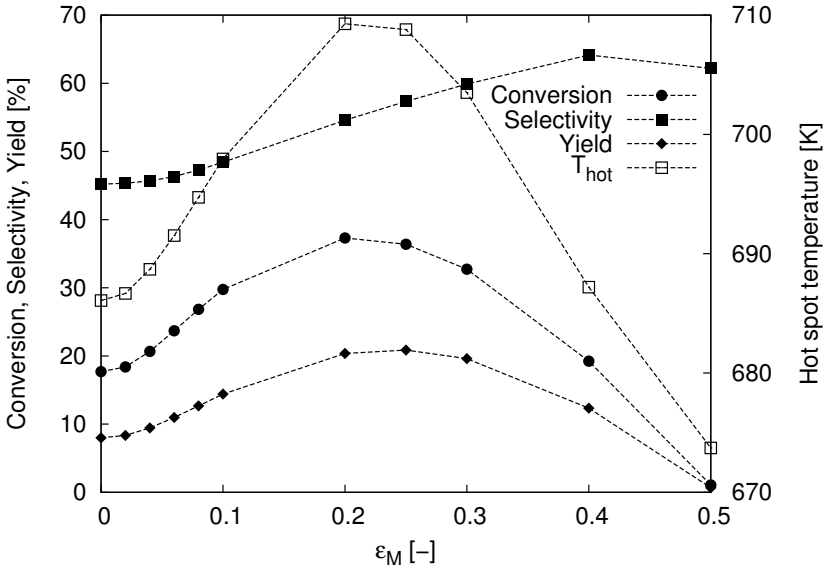

Figure 9.5: Effect of the macro-pore porosity ε_M on the simulated fixed-bed reactor performance for n-butane oxidation.

fixing the total porosity, the pellet density and bed density were kept unchanged with varying distribution of the macro and micro pores porosity in the pellets. The following question is addressed in this work: Which pore structure of the catalyst pellet is more efficient for a given mass of active catalyst and fixed pellet shape. All simulations were carried out at the same operational conditions as for the reference case.

Firstly, the macro-pore porosity ε_M was varied from 0 to 0.5 while the macro and micro-pore diameters were kept to the values of the reference case. Figure 9.5 shows the simulated reactor performance, i.e the overall conversion, selectivity and yield at the outlet of the fixed-bed. These were calculated as integral average at the outlet:

$$Conversion = \frac{N_{\mathrm{C_4H_{10}},in} - N_{\mathrm{C_4H_{10}}}}{N_{\mathrm{C_4H_{10}},in}}, \tag{9.8}$$

$$Selectivity = \frac{N_{\mathrm{C_4H_2O_3}}}{N_{\mathrm{C_4H_{10}},in} - N_{\mathrm{C_4H_{10}}}}, \tag{9.9}$$

$$Yield = Conversion \cdot Selectivity, \tag{9.10}$$

where the $N_{\mathrm{C_4H_{10}}}$ stands for the molar flux of $\mathrm{C_4H_{10}}$ in unit of mol $\cdot\mathrm{m}^{-2}\cdot\mathrm{s}^{-1}$. The hot spot temperature was evaluated as the maximum temperature in the calculation domain.

With increasing fraction of macro-pores in the catalyst pellet, conversion of n-butane first increases and experiences a maximum when $\varepsilon_M = 0.2$. Then, the conversion drops and reaches the lowest value at the upper limit when all the pores are macro-pores. The selectivity increases gradually with increasing ε_M except for the case when $\varepsilon_M = 0.5$. For industry, yield is important as n-butane is not recycled. As one can see in Figure 9.5, the yield has similar shape as the conversion with respect to ε_M but the maximum is slight shifted to $\varepsilon_M = 0.25$ which is also the reference case used in this work. The hot spot temperature follows the same trend as the conversion due to the reaction progress. The highest hot spot temperature for $\varepsilon_M = 0.2$ is 36 K

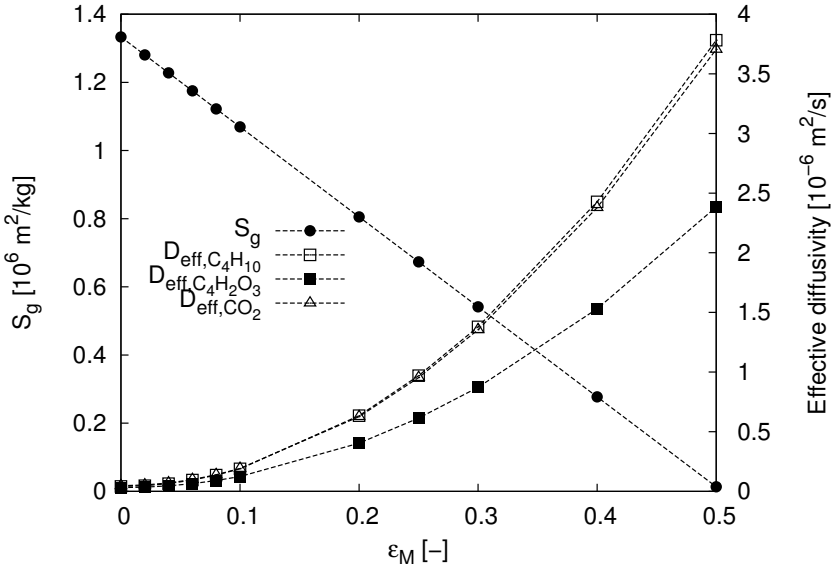

Figure 9.6: Effect of the macro-pore porosity ε_M on the specific surface area S_g and effective diffusivity $D_{eff,i}$.

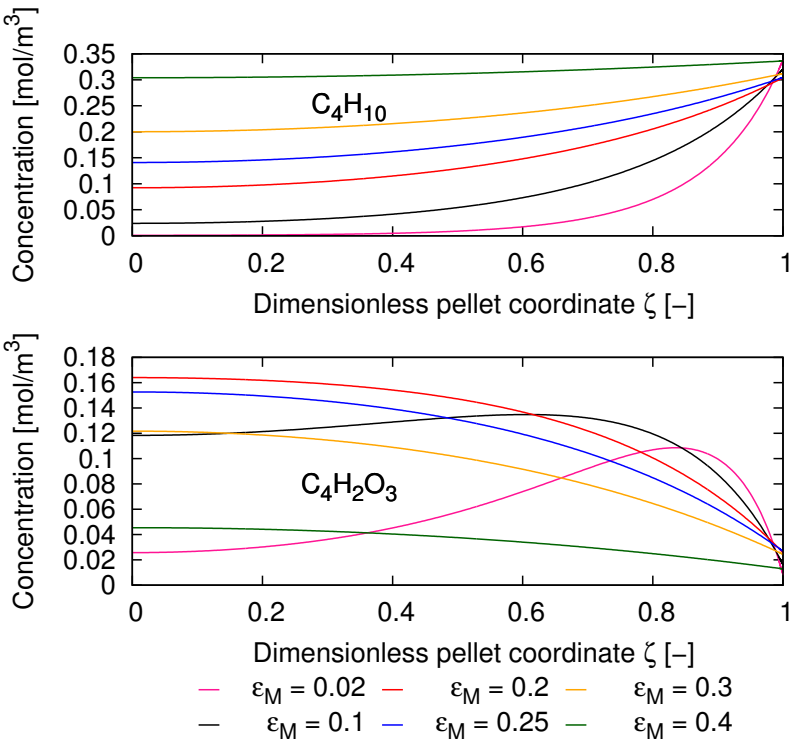

Figure 9.7: Effect of the macro-pore porosity ε_M on concentration profiles of C_4H_{10} and $C_4H_2O_3$ inside the pellet located at position 1.

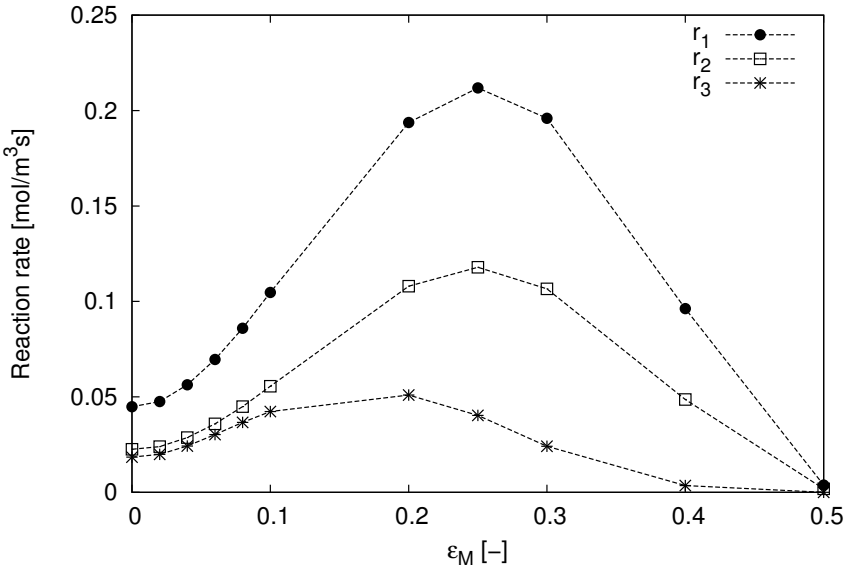

Figure 9.8: Effect of the macro-pore porosity ε_M on the integrated average reaction rates r_i of the pellet located at position 1.

higher than the inlet temperature. This temperature rise is still within the tolerance temperature rise (Max. 60 K in literature) [233]. The resulting reactor performance indicates that catalysts with bimodal pore structure can out-perform those with only micro-pores or only macro-pores being the two limiting cases. The optimal distribution of the macro- and micro- pores in the presented study is achieved when $\varepsilon_M = 0.25$ if the maximum yield is the concerned criteria. This optimum is a compromise between the high reactive surface mostly created by the micro-pores, and high diffusion rate facilitated by the macro-pores (transport pores).

Figure 9.6 illustrates the specific surface S_g and the effective diffusivity of selected species $D_{eff,i}$ as function of ε_M. The specific surface area decreases linear with ε_M and the diffusivity increases quadratically with ε_M. Both trends can be mathematically explained by Eq. 3.1 and Eq. 3.4. The interplay between diffusion and reaction was already found a few decades ago [130]. The question is how much the yield can be improved by tuning the pore-structure of the catalyst pellet. In the presented study, even with slight modification, from $\varepsilon_M = 0.3$ to $\varepsilon_M = 0.25$, 1% of yield improvement can be achieved which is of industrial interest [72] due to high production capacity of MA. These results clearly demonstrate that the role of the pore structure of the catalyst can be as important as the improvement of the catalyst. Eventhough the presented values are based on estimated values of pore structure, the trend observed from the calculations will be conserved in reality. Another message from Figure 9.5 is that a not optimised fraction of macro-pores from the pelleting process can make a poor-performance catalyst even though the active ingredients are not altered.

In order to better understand the influence of the pore structure parameter ε_M on the pellet scale, the concentration profiles of C_4H_{10} and $C_4H_2O_3$ inside the pellet located at position 1 are plotted in Figure 9.7. When ε_M is lower than 0.1, very steep concentration gradient of C_4H_{10} can be observed. This is a clear indication of the diffusion limitation that barely any reactant molecules can enter the interior active surface. After introducing the macro-pores, for example $\varepsilon_M = 0.1$, the inner parts of the catalyst pellet become accessible. When $\varepsilon_M < 0.1$, the concentration profile of

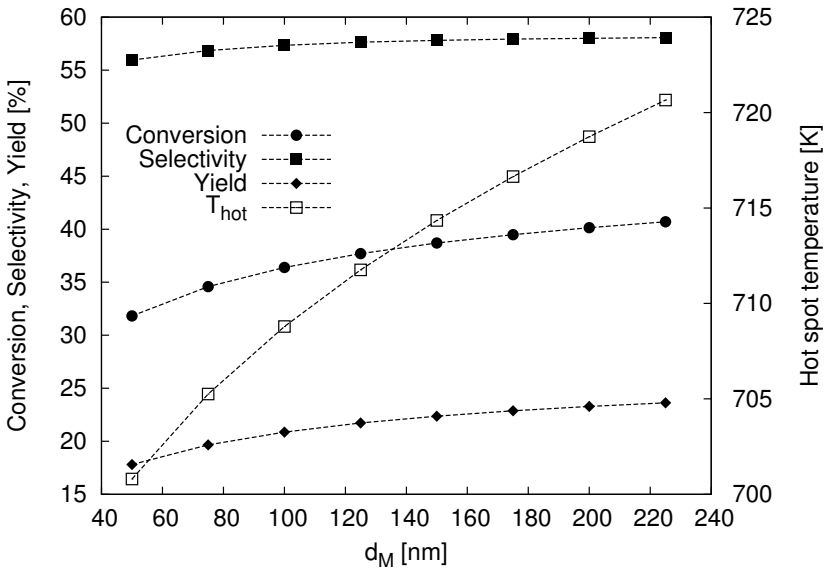

Figure 9.9: Effect of the macro-pore diameter d_M on the simulated fixed-bed reactor performance for n-butane oxidation.

$C_4H_2O_3$ first increases gradually due to the higher concentration of C_4H_{10} and thus higher reaction rates. The maximum found around $\zeta = 0.80$ is likely because of the accumulation of the $C_4H_2O_3$ molecules when the diffusion rate is still low compared to the reaction. With increasing fraction of the macro-pores inside the pellet, the concentration profiles for both species flatten out. It is not only because of the faster diffusion of the reactants inwards and products outwards of the pore, but also because of the loss of reaction sites due to the reduced specific surface. Above $\varepsilon_M = 0.3$, the catalyst performance is limited by the reduction of the active surfaces.

Integral averages of the reaction rates inside the pellet at position 1 were evaluated and depicted in Figure 9.8. Reaction rates r_1 and r_2 show the same trend with respect to ε_M. This is expected from the kinetic expressions in Eq. 9.5 and 9.6. The decomposition reaction rate r_3 shows a different behaviour as a function of ε_M. It seems that the influence of accelerated diffusion rate on r_3 is less pronounced than the reduction of the surface area as one can see from the slope of the increasing part (r_1, r_2) compared to the decreasing part (r_3). This means the diffusion-reaction balance has a different effect on each individual reaction. With that it is possible to not only promote conversion, but also the selectivity by changing the pore structure. From the presented results, the key is to find the 'right' pore structure where the main reaction rate r_1 is high enough and the undesired consecutive reaction rate r_3 is rather low. The optimal value for ε_M is 0.25, the same value as observed for the reactor scale. At this point, one can deduce that the fractions of macro- and micro-pores inside the catalyst pellet have effects on both the concentration profiles and reaction kinetics on the pellet scale and on the reactor scale. In addition to catalyst synthesis, optimizing the pellet pore structure offers the possibility to improve industrial maleic anhydride synthesis.

The other two parameters studied in this work were the macro-pore diameter d_M and micro-pore diameter d_m. Simulations with independent variation of d_M and d_m were carried out while the fraction of the macro- and micro-porosity ($\varepsilon_M = \varepsilon_m = 0.25$) were fixed. From the presented results above, $\varepsilon_M = 0.25$ is the optimal value for d_M

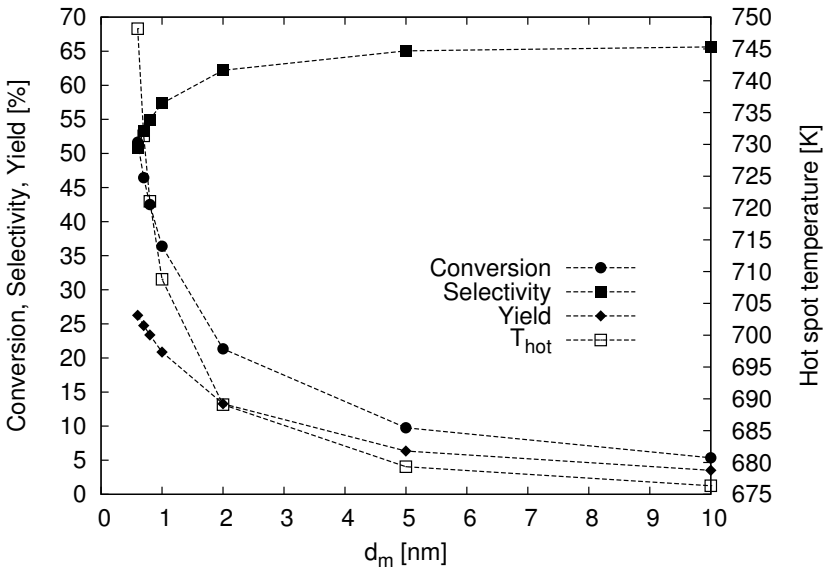

Figure 9.10: Effect of the micro-pore diameter d_m on the simulated fixed-bed reactor performance for n-butane oxidation.

= 100 nm and d_m = 1 nm. In the following section, the main goal is to investigate if further improvement is possible by tuning the pore size. Figure 9.9 shows the overall conversion, selectivity, yield and hot spot temperature with respect to the macro-pore diameter. Both conversion and selectivity increase with increasing macro-pore diameter slightly. The overall yield of the product is improved, e.g. by 3% by increasing d_M from 100 nm to 200 nm. The increase of the overall reactor performance can be explained by the acceleration of the diffusion rate since the Knudsen diffusivity increases linearly with the pore diameters. On the other hand, the specific area for reaction decreases with increasing d_M but to a less significant extent than the promotion of the diffusion. However, the hot spot temperature increases further with increasing conversion and eventually will lead to destruction of the catalyst. Therefore, a maximum of 200 nm of the macro-pore diameter can be suggested for this case.

The influence of micro-pore diameter d_m on the overall reactor performance is shown in Figure 9.10. The conversion of n-butane decreases rapidly with increasing d_m. Even though the selectivity increases slightly, the overall yield of the product decreases with increasing d_m. The decrease of conversion is a consequence of the decreasing specific area with decreasing d_m. Since the micro-pore diameter is in the denominator for calculating the specific area, a reduced value of d_m will lead to much higher surface area and thus an enhanced reaction rate. Whilst, the diffusivity decreases with decreasing d_m. The decrease of the selectivity is probably because the parallel and consecutive reactions are both enhanced with higher surface area and slower diffusion. Again, taking into account the hot-spot temperature, a minimum value of 0.8 nm can be suggested for the micro-pore diameter based on the presented results.

The results of the reactor performance in regard to the changing pore diameters reveal that the 'bi-modal' catalyst with larger transport pores (higher value of d_M) and higher surface area (lower values of d_m) are preferred for the given kinetics. Similar results can be found in the work of Hegedus [130] even though the reactions studied were totally different. In order to check the generality of the obtained results, the

kinetic parameters (a_i) are changed artificially to a 'better' catalyst and the simulations were repeated. Similar behaviour can be found for the reactor performance with respect to the pore structure parameters. In the case of the modified kinetics, the optimal value for ε_M is 0.2. The same values are found for d_M and d_m with highest yield within the limited values calculated. With this, it is possible to say that pore structure optimization can be a general strategy for improving the efficiency of the catalyst as well as the processes. The optimal structure can be different with different reaction kinetics or process parameters.

One may observe that the reactor performance is more sensitive to ε_M and d_m than d_M at the given conditions. Since the micro-pore diameter is formed during synthesis the active powder, tuning this parameter is rather difficult. The pore structure of the macro-pores may be manipulated by pore-templating e.g. by embedding of polymeric micro-spheres into the pellet as suggested by Hegedus [130]. For example, the macro-porosity and macro-pore diameter maybe tuned by the portion and size of the template added. Carreon and Guliants [238] have synthesized macroporous VPP catalyst by employing monodisperse polystyrene spheres arrays as a template. They reported better performance of the macroporous VPP catalyst compared to the conventional organic VPP catalyst. The authors attribute the better performance to the high surface area and active phase of the precursor [239].

9.3 Conclusions

N-butane oxidation to maleic anhydride in a fixed-bed reactor has been simulated with a detailed two-dimensional heterogeneous model. The diffusion-reaction balances inside the pellet were solved with the help of the micro- and macro pore model of Wakao and Smith [92, 131] considering both Knudsen and molecular diffusion in the micro and macro pore regions. Effects of the pore structure parameters ε_M, d_M and d_m on the performance of the reactor were highlighted. With the overall yield of maleic anhydride as target object, catalyst pellets with bi-modality, bigger macro-pore and smaller micro-pore are favoured from the simulation results. The optimal values of the pore structure parameters correspond to the given operation condition and kinetics used in this work. The model parameters could be adjusted according to experimental inputs when translated to other systems. Rational design and synthesis of VPP catalyst with desirable pore structure may offer a new strategy to improve this process.

Bibliography

[1] R. H. Wilhelm, Progress towards the a priori design of chemical reactors, Pure and Applied Chemistry 5 (3-4).

[2] G. F. Froment, Chemical reactor analysis and design, 3rd Edition, Wiley, Hoboken, N.J, 2011.

[3] R. Aris, Elementary chemical reactor analysis, Dover Publication, Mineola, N.Y, 1999.

[4] O. Levenspiel, Chemical reaction engineering, 3rd Edition, Wiley, New York, 1999.

[5] S. Ergun, Fluid flow through packed columns, Chemical Engineering Progress 48 (1952) 89–94.

[6] H. Freund, K. Sundmacher, Towards a methodology for the systematic analysis and design of efficient chemical processes, Chemical Engineering and Processing: Process Intensification 47 (12) (2008) 2051–2060.

[7] J. Joshi, K. Nandakumar, Computational Modeling of Multiphase Reactors, Annual Review of Chemical and Biomolecular Engineering 6 (1) (2015) 347–378.

[8] J. M. Thomas, W. J. Thomas, Principles and practice of heterogeneous catalysis, 2nd Edition, Wiley-VCH, Weinheim, 2015.

[9] F. J. Keil, Complexities in modeling of heterogeneous catalytic reactions, Computers & Mathematics with Applications 65 (10) (2013) 1674–1697.

[10] S. S. Elnashaie, Modelling, simulation and optimization of industrial fixed bed catalytic reactors, Vol. 7, CRC Press, 1994.

[11] F. J. Keil, Process intensification, Reviews in Chemical Engineering 0 (0).

[12] V. V. Ranade, Computational flow modeling for chemical reactor engineering, Elsevier, Amsterdam [u.a., 2002, oCLC: 874342924.

[13] S. Matera, M. Maestri, A. Cuoci, K. Reuter, Predictive-Quality Surface Reaction Chemistry in Real Reactor Models: Integrating First-Principles Kinetic Monte Carlo Simulations into Computational Fluid Dynamics, ACS Catalysis 4 (11) (2014) 4081–4092.

[14] D. Vlachos, A. Mhadeshwar, N. Kaisare, Hierarchical multiscale model-based design of experiments, catalysts, and reactors for fuel processing, Computers & Chemical Engineering 30 (10-12) (2006) 1712–1724.

[15] F. J. Keil, Modelling of phenomena within catalyst particles, Chemical Engineering Science 51 (10) (1996) 1543–1567.

[16] A. Kołodziej, J. Łojewska, Experimental and modelling study on flow resistance of wire gauzes, Chemical Engineering and Processing: Process Intensification 48 (3) (2009) 816–822.

[17] V. I. Vanchurin, E. V. Golovnya, A. V. Yashchenko, Oxidation of ammonia on woven and knitted platinoid gauzes, Catalysis in Industry 4 (2) (2012) 105–109.

[18] N. Waletzko, L. D. Schmidt, Modeling catalytic gauze reactors: HCN synthesis, AIChE Journal 34 (7) (1988) 1146–1156.

[19] M. Baker, P. Young, G. Tabor, Image based meshing of packed beds of cylinders at low aspect ratios using 3d MRI coupled with computational fluid dynamics, Computers & Chemical Engineering 35 (10) (2011) 1969–1977.

[20] E. Yuen, A. Sederman, F. Sani, P. Alexander, L. Gladden, Correlations between local conversion and hydrodynamics in a 3-D fixed-bed esterification process: An MRI and lattice-Boltzmann study, Chemical Engineering Science 58 (3-6) (2003) 613–619.

[21] X. Fan, X. Ou, F. Xing, G. A. Tdisableurley, P. Denissenko, M. A. Williams, N. Batail, C. Pham, A. A. Lapkin, Microtomography-based numerical simulations of heat transfer and fluid flow through β-SiC open-cell foams for catalysis, Catalysis Today.

[22] S. Meinicke, T. Wetzel, B. Dietrich, Scale-resolved CFD modelling of single-phase hydrodynamics and conjugate heat transfer in solid sponges, International Journal of Heat and Mass Transfer 108 (2017) 1207–1219.

[23] M. Twigg, J. Richardson, Theory and Applications of Ceramic Foam Catalysts, Chemical Engineering Research and Design 80 (2) (2002) 183–189.

[24] E. Tsotsas, M7 Heat and Mass Transfer in Packed Beds with Fluid Flow, in: VDI e. V. (Ed.), VDI Heat Atlas, Springer Berlin Heidelberg, Berlin, Heidelberg, 2010, pp. 1327–1342.

[25] G. D. Wehinger, Particle-resolved CFD simulations of catalytic flow reactors, Ph.D. thesis, Technische Universität Berlin (2016).

[26] T. Eppinger, K. Seidler, M. Kraume, DEM-CFD simulations of fixed bed reactors with small tube to particle diameter ratios, Chemical Engineering Journal 166 (1) (2011) 324–331.

[27] Y. Dong, B. Sosna, O. Korup, F. Rosowski, R. Horn, Investigation of radial heat transfer in a fixed-bed reactor: CFD simulations and profile measurements, Chemical Engineering Journal 317 (2017) 204–214.

[28] A. G. Dixon, M. Nijemeisland, CFD as a Design Tool for Fixed-Bed Reactors, Industrial & Engineering Chemistry Research 40 (23) (2001) 5246–5254.

[29] M. Nijemeisland, A. G. Dixon, Comparison of CFD simulations to experiment for convective heat transfer in a gassolid fixed bed, Chemical Engineering Journal 82 (1-3) (2001) 231–246.

[30] M. Nijemeisland, A. G. Dixon, E. Hugh Stitt, Catalyst design by CFD for heat transfer and reaction in steam reforming, Chemical Engineering Science 59 (22-23) (2004) 5185–5191.

[31] S. A. Logtenberg, A. G. Dixon, Computational fluid dynamics studies of fixed bed heat transfer, Chemical Engineering and Processing: Process Intensification 37 (1) (1998) 7–21.

[32] A. G. Dixon, M. Ertan Taskin, E. Hugh Stitt, M. Nijemeisland, 3d CFD simulations of steam reforming with resolved intraparticle reaction and gradients, Chemical Engineering Science 62 (18-20) (2007) 4963–4966.

[33] A. G. Dixon, M. Nijemeisland, E. H. Stitt, Packed Tubular Reactor Modeling and Catalyst Design using Computational Fluid Dynamics, in: Advances in Chemical Engineering, Vol. 31, Elsevier, 2006, pp. 307–389.

[34] A. Guardo, M. Coussirat, M. Larrayoz, F. Recasens, E. Egusquiza, Influence of the turbulence model in CFD modeling of wall-to-fluid heat transfer in packed beds, Chemical Engineering Science 60 (6) (2005) 1733–1742.

[35] H. Calis, J. Nijenhuis, B. Paikert, F. Dautzenberg, C. van den Bleek, CFD modelling and experimental validation of pressure drop and flow profile in a novel structured catalytic reactor packing, Chemical Engineering Science 56 (4) (2001) 1713–1720.

[36] M. Baker, S. Daniels, P. Young, G. Tabor, Investigation of flow through a computationally generated packed column using CFD and Additive Layer Manufacturing, Computers & Chemical Engineering 67 (2014) 159–165.

[37] M. Baker, G. Tabor, Computational analysis of transitional air flow through packed columns of spheres using the finite volume technique, Computers & Chemical Engineering 34 (6) (2010) 878–885.

[38] S. Romkes, F. Dautzenberg, C. van den Bleek, H. Calis, CFD modelling and experimental validation of particle-to-fluid mass and heat transfer in a packed bed at very low channel to particle diameter ratio, Chemical Engineering Journal 96 (1-3) (2003) 3–13.

[39] A. G. Dixon, CFD study of effect of inclination angle on transport and reaction in hollow cylinder catalysts, Chemical Engineering Research and Design 92 (7) (2014) 1279–1295.

[40] A. Singhal, S. Cloete, S. Radl, R. Quinta-Ferreira, S. Amini, Heat transfer to a gas from densely packed beds of monodisperse spherical particles, Chemical Engineering Journal 314 (2017) 27–37.

[41] M. Behnam, A. G. Dixon, M. Nijemeisland, E. H. Stitt, Catalyst Deactivation in 3d CFD Resolved Particle Simulations of Propane Dehydrogenation, Industrial & Engineering Chemistry Research 49 (21) (2010) 10641–10650.

[42] M. E. Taskin, A. G. Dixon, M. Nijemeisland, E. H. Stitt, CFD Study of the Influence of Catalyst Particle Design on Steam Reforming Reaction Heat Effects in Narrow Packed Tubes, Industrial & Engineering Chemistry Research 47 (16) (2008) 5966–5975.

[43] A. G. Dixon, J. Boudreau, A. Rocheleau, A. Troupel, M. E. Taskin, M. Nijemeisland, E. H. Stitt, Flow, Transport, and Reaction Interactions in Shaped Cylindrical Particles for Steam Methane Reforming, Industrial & Engineering Chemistry Research 51 (49) (2012) 15839–15854.

[44] T. Eppinger, G. D. Wehinger, N. Jurtz, R. Aglave, M. Kraume, A numerical optimization study on the catalytic dry reforming of methane in a spatially resolved fixed-bed reactor, Chemical Engineering Research and Design 115 (2016) 374–381.

[45] A. G. Dixon, Local transport and reaction rates in a fixed bed reactor tube: Endothermic steam methane reforming, Chemical Engineering Science 168 (2017) 156–177.

[46] A. Akolkar, J. Petrasch, Tomography-Based Characterization and Optimization Of Fluid Flow Through Porous Media, Transport in Porous Media 95 (3) (2012) 535–550.

[47] J. Theuerkauf, P. Witt, D. Schwesig, Analysis of particle porosity distribution in fixed beds using the discrete element method, Powder Technology 165 (2) (2006) 92–99.

[48] P. A. Cundall, O. D. Strack, A discrete numerical model for granular assemblies, geotechnique 29 (1) (1979) 47–65.

[49] S. Ookawara, M. Kuroki, D. Street, K. Ogawa, High-fidelity dem-cfd modeling of packed bed reactors for process intensification, in: Proceedings of European Congress of Chemical Engineering (ECCE-6), Copenhagen, 2007, pp. 16–20.

[50] M. V. Tabib, S. T. Johansen, S. Amini, A 3d CFD-DEM Methodology for Simulating Industrial Scale Packed Bed Chemical Looping Combustion Reactors, Industrial & Engineering Chemistry Research 52 (34) (2013) 12041–12058.

[51] H. Bai, J. Theuerkauf, P. A. Gillis, P. M. Witt, A Coupled DEM and CFD Simulation of Flow Field and Pressure Drop in Fixed Bed Reactor with Randomly Packed Catalyst Particles, Industrial & Engineering Chemistry Research 48 (8) (2009) 4060–4074.

[52] N. Zobel, T. Eppinger, F. Behrendt, M. Kraume, Influence of the wall structure on the void fraction distribution in packed beds, Chemical Engineering Science 71 (2012) 212–219.

[53] W. Soppe, Computer simulation of random packings of hard spheres, Powder Technology 62 (2) (1990) 189–197.

[54] H. Freund, T. Zeiser, F. Huber, E. Klemm, G. Brenner, F. Durst, G. Emig, Numerical simulations of single phase reacting flows in randomly packed fixed-bed reactors and experimental validation, Chemical Engineering Science 58 (3-6) (2003) 903–910.

[55] H. Freund, J. Bauer, T. Zeiser, G. Emig, Detailed Simulation of Transport Processes in Fixed-Beds, Industrial & Engineering Chemistry Research 44 (16) (2005) 6423–6434.

[56] R. Caulkin, M. Fairweather, X. Jia, A. Ahmad, R. A. Williams, Application of a digital packing algorithm to cylindrical pellet-packed beds, in: Computer Aided Chemical Engineering, Vol. 25, Elsevier, 2008, pp. 745–750.

[57] H. Stitt, M. Marigo, S. Wilkinson, How Good is Your Model?, Johnson Matthey Technology Review 59 (2) (2015) 74–89.

[58] M. Marigo, E. H. Stitt, Discrete Element Method (DEM) for Industrial Applications: Comments on Calibration and Validation for the Modelling of Cylindrical Pellets, KONA Powder and Particle Journal 32 (0) (2015) 236–252.

[59] M. Dosta, S. Dale, S. Antonyuk, C. Wassgren, S. Heinrich, J. D. Litster, Numerical and experimental analysis of influence of granule microstructure on its compression breakage, Powder Technology 299 (2016) 87–97.

[60] S. Eckhard, M. Fries, S. Antonyuk, S. Heinrich, Dependencies between internal structure and mechanical properties of spray dried granules Experimental study and DEM simulation, Advanced Powder Technology 28 (1) (2017) 185–196.

[61] Z. Yan, S. K. Wilkinson, E. H. Stitt, M. Marigo, Discrete element modelling (DEM) input parameters: understanding their impact on model predictions using statistical analysis, Computational Particle Mechanics 2 (3) (2015) 283–299.

[62] T. Atmakidis, E. Y. Kenig, CFD-based analysis of the wall effect on the pressure drop in packed beds with moderate tube/particle diameter ratios in the laminar flow regime, Chemical Engineering Journal 155 (1-2) (2009) 404–410.

[63] A. G. Dixon, M. Nijemeisland, E. H. Stitt, Systematic mesh development for 3d CFD simulation of fixed beds: Contact points study, Computers & Chemical Engineering 48 (2013) 135–153.

[64] G. D. Wehinger, C. Fütterer, M. Kraume, Contact Modifications for CFD Simulations of Fixed-Bed Reactors: Cylindrical Particles, Industrial & Engineering Chemistry Research 56 (1) (2017) 87–99.

[65] G. Boccardo, F. Augier, Y. Haroun, D. Ferré, D. L. Marchisio, Validation of a novel open-source work-flow for the simulation of packed-bed reactors, Chemical Engineering Journal 279 (2015) 809–820.

[66] S. Rebughini, A. Cuoci, M. Maestri, Handling contact points in reactive CFD simulations of heterogeneous catalytic fixed bed reactors, Chemical Engineering Science 141 (2016) 240–249.

[67] M. Maestri, A. Cuoci, Coupling CFD with detailed microkinetic modeling in heterogeneous catalysis, Chemical Engineering Science 96 (2013) 106–117.

[68] G. Mestl, D. Lesser, T. Turek, Optimum Performance of Vanadyl Pyrophosphate Catalysts, Topics in Catalysis 59 (17-18) (2016) 1533–1544.

[69] S. A. Schunk, Oxyfunctionalization of Alkanes, in: Handbook of Heterogeneous Catalysis, Wiley-VCH Verlag GmbH & Co. KGaA, Weinheim, Germany, 2008, pp. 3400–3425.

[70] V. Guliants, J. Benziger, S. Sundaresan, I. Wachs, Molecular structure-reactivity relationships in n-butane oxidation over bulk VPO and supported vanadia catalysts: Lessons for molecular engineering of new selective catalysts for alkane oxidation, in: Studies in Surface Science and Catalysis, Vol. 130, Elsevier, 2000, pp. 1721–1726.

[71] R. K. Sharma, D. L. Cresswell, E. J. Newson, Kinetics and fixed-bed reactor modeling of butane oxidation to maleic anhydride, AIChE Journal 37 (1) (1991) 39–47.

[72] F. Trifirò, R. K. Grasselli, How the Yield of Maleic Anhydride in n-Butane Oxidation, Using VPO Catalysts, was Improved Over the Years, Topics in Catalysis 57 (14) (2014) 1188–1195.

[73] J. C. Védrine, G. J. Hutchings, C. J. Kiely, Molybdenum oxide model catalysts and vanadium phosphates as actual catalysts for understanding heterogeneous catalytic partial oxidation reactions: A contribution by jean-claude volta, Catalysis Today 217 (2013) 57–64.

[74] C. Kiely, Characterisation of variations in vanadium phosphate catalyst microstructure with preparation route, Journal of Catalysis 162 (1) (1996) 31–47.

[75] G. J. Hutchings, Vanadium phosphate: a new look at the active components of catalysts for the oxidation of butane to maleic anhydride, Journal of Materials Chemistry 14 (23) (2004) 3385.

[76] D. Lesser, G. Mestl, T. Turek, Transient behavior of vanadyl pyrophosphate catalysts during the partial oxidation of n-butane in industrial-sized, fixed bed reactors, Applied Catalysis A: General 510 (2016) 1–10.

[77] S. Hofmann, T. Turek, Process intensification of n-butane oxidation to maleic anhydride in a milli-structured reactor, Chemical Engineering & Technology.

[78] P. Marín, C. Hamel, S. Ordóñez, F. Díez, E. Tsotsas, A. Seidel-Morgenstern, Analysis of a fluidized bed membrane reactor for butane partial oxidation to maleic anhydride: 2d modelling, Chemical Engineering Science 65 (11) (2010) 3538–3548.

[79] H. Lintz, A. Reitzmann, Alternative Reaction Engineering Concepts in Partial Oxidations on Oxidic Catalysts, Catalysis Reviews 49 (1) (2007) 1–32.

[80] B. Partopour, A. G. Dixon, Resolved-particle fixed bed CFD with microkinetics for ethylene oxidation, AIChE Journal 63 (1) (2017) 87–94.

[81] G. D. Wehinger, F. Klippel, M. Kraume, Modeling pore processes for particle-resolved CFD simulations of catalytic fixed-bed reactors, Computers & Chemical Engineering 101 (2017) 11–22.

[82] R. Horn, K. Williams, N. Degenstein, L. Schmidt, Syngas by catalytic partial oxidation of methane on rhodium: Mechanistic conclusions from spatially resolved measurements and numerical simulations, Journal of Catalysis 242 (1) (2006) 92–102.

[83] R. Horn, K. Williams, N. Degenstein, L. Schmidt, Mechanism of H2 and CO formation in the catalytic partial oxidation of CH4 on Rh probed by steady-state spatial profiles and spatially resolved transients, Chemical Engineering Science 62 (5) (2007) 1298–1307.

[84] J. Touitou, F. Aiouache, R. Burch, R. Douglas, C. Hardacre, K. Morgan, J. S, C. Stewart, J. Stewart, A. Goguet, Evaluation of an in situ spatial resolution instrument for fixed beds through the assessment of the invasiveness of probes and a comparison with a micro-kinetic model, Journal of Catalysis 319 (2014) 239–246.

[85] O. Korup, C. F. Goldsmith, G. Weinberg, M. Geske, T. Kandemir, R. Schlögl, R. Horn, Catalytic partial oxidation of methane on platinum investigated by spatial reactor profiles, spatially resolved spectroscopy, and microkinetic modeling, Journal of Catalysis 297 (2013) 1–16.

[86] H. Schwarz, Gas-phase methane oxidation investigated by laser-induced fluorescence, species profile measurements and kinetic reactor simulations, Ph.D. thesis, Technische Universität Berlin (Jan. 2014).

[87] H.-J. Freund, G. Meijer, M. Scheffler, R. Schlögl, M. Wolf, CO Oxidation as a Prototypical Reaction for Heterogeneous Processes, Angewandte Chemie International Edition 50 (43) (2011) 10064–10094.

[88] J. Gerdts, Foam catalyst for partial oxidation reactions studied by x-ray microtomography, reactor profile measurements and numerical simulations, Master's thesis, Hamburg University of Technology (2016).

[89] N. Ellenfeld, Investigation of porosity profiles, heat and mass transport in catalyst packings of hollow cylinders and split, Master's thesis, Hamburg University of Technology (Mar. 2016).

[90] B. Sosna, Determination of effective axial and radial heat transfer coefficients in a fixed catalyst bed by experiment and simulation, Master's thesis, Hamburg University of Technology (May 2015).

[91] F. Cavani, C. Cortelli, A. Frattini, G. Puccinotti, M. Ricotta, F. Rodeghiero, F. Trifir, C. Fumagalli, G. Mazzoni, The dilution of vanadyl pyrophosphate, catalyst for n-butane oxidation to maleic anhydride, with aluminum phosphate: unexpected reactivity due to the contribution of the diluting agent, Topics in Catalysis 38 (4) (2006) 295–301.

[92] N. Wakao, J. Smith, Diffusion in catalyst pellets, Chemical Engineering Science 17 (11) (1962) 825–834.

[93] S. Rebughini, A. Cuoci, A. G. Dixon, M. Maestri, Cell agglomeration algorithm for coupling microkinetic modeling and steady-state CFD simulations of catalytic reactors, Computers & Chemical Engineering 97 (2017) 175–182.

[94] T. Maffei, G. Gentile, S. Rebughini, M. Bracconi, F. Manelli, S. Lipp, A. Cuoci, M. Maestri, A multiregion operator-splitting CFD approach for coupling microkinetic modeling with internal porous transport in heterogeneous catalytic reactors, Chemical Engineering Journal 283 (2016) 1392–1404.

[95] N. Hansen, Multiscale modeling of reaction and diffusion in Zeolites, Ph.D. thesis, Hamburg University of Technology (2010).

[96] O. R. Derkx, A. G. Dixon, Effect of the wall Nusselt number on the simulation of catalytic fixed bed reactors, Catalysis Today 35 (4) (1997) 435–442.

[97] M. Winterberg, E. Tsotsas, A. Krischke, D. Vortmeyer, A simple and coherent set of coefficients for modelling of heat and mass transport with and without chemical reaction in tubes filled with spheres, Chemical Engineering Science 55 (5) (2000) 967–979.

[98] A. G. Dixon, Fixed bed catalytic reactor modelling-the radial heat transfer problem, The Canadian Journal of Chemical Engineering 90 (3) (2012) 507–527.

[99] M. Kleiber, R. Joh, D1 Calculation Methods for Thermophysical Properties, in: VDI e. V. (Ed.), VDI Heat Atlas, Springer Berlin Heidelberg, Berlin, Heidelberg, 2010, pp. 119–152.

[100] J. Papageorgiou, G. Froment, Simulation models accounting for radial voidage profiles in fixed-bed reactors, Chemical Engineering Science 50 (19) (1995) 3043–3056.

[101] J. M. P. Q. Delgado, A critical review of dispersion in packed beds, Heat and Mass Transfer 42 (4) (2006) 279–310.

[102] R. W. Fahien, J. M. Smith, Mass transfer in packed beds, AIChE Journal 1 (1) (1955) 28–37.

[103] O. Bey, G. Eigenberger, Fluid flow through catalyst filled tubes, Chemical Engineering Science 52 (8) (1997) 1365–1376.

[104] J. G. H. Borkink, K. R. Westerterp, Significance of axial heat dispersion for the description of heat transport in wall-cooled packed beds, Chemical Engineering & Technology 15 (6) (1992) 371–384.

[105] E. Tsotsas, E.-U. Schlünder, Heat transfer in packed beds with fluid flow: remarks on the meaning and the calculation of a heat transfer coefficient at the wall, Chemical Engineering Science 45 (4) (1990) 819–837.

[106] E. Tsotsas, H. Martin, Thermal conductivity of packed beds: A review, Chemical Engineering and Processing: Process Intensification 22 (1) (1987) 19–37.

[107] P. Magnico, Pore-scale simulations of unsteady flow and heat transfer in tubular fixed beds, AIChE Journal 55 (4) (2009) 849–867.

[108] B. Eisfeld, K. Schnitzlein, The influence of confining walls on the pressure drop in packed beds, Chemical Engineering Science 56 (14) (2001) 4321–4329.

[109] A. G. Dixon, An improved equation for the overall heat transfer coefficient in packed beds, Chemical Engineering and Processing: Process Intensification 35 (5) (1996) 323–331.

[110] M. Nijemeisland, A. G. Dixon, CFD study of fluid flow and wall heat transfer in a fixed bed of spheres, AIChE Journal 50 (5) (2004) 906–921.

[111] B. Sosna, Y. Dong, L. Chromow, O. Korup, R. Horn, Effective Axial Thermal Conductivity in Catalyst Packings from High Resolution Temperature Profiles, Chemie Ingenieur Technik 88 (11) (2016) 1676–1683.

[112] R. Wijngaarden, K. Westerterp, Do the effective heat conductivity and the heat transfer coefficient at the wall inside a packed bed depend on a chemical reaction? Weaknesses and applicability of current models, Chemical Engineering Science 44 (8) (1989) 1653–1663.

[113] K. Vollmari, T. Oschmann, S. Wirtz, H. Kruggel-Emden, Pressure drop investigations in packings of arbitrary shaped particles, Powder Technology 271 (2015) 109–124.

[114] A. G. Dixon, G. Walls, H. Stanness, M. Nijemeisland, E. H. Stitt, Experimental validation of high Reynolds number CFD simulations of heat transfer in a pilot-scale fixed bed tube, Chemical Engineering Journal 200-202 (2012) 344–356.

[115] M. Behnam, A. G. Dixon, M. Nijemeisland, E. H. Stitt, A New Approach to Fixed Bed Radial Heat Transfer Modeling Using Velocity Fields from Computational Fluid Dynamics Simulations, Industrial & Engineering Chemistry Research 52 (44) (2013) 15244–15261.

[116] M. T. Zambon, D. A. Asensio, G. F. Barreto, G. D. Mazza, Application of Computational Fluid Dynamics (CFD) for the Evaluation of Fluid Convective Radial Heat Transfer Parameters in Packed Beds, Industrial & Engineering Chemistry Research 53 (49) (2014) 19052–19061.

[117] G. D. Wehinger, T. Eppinger, M. Kraume, Detailed numerical simulations of catalytic fixed-bed reactors: Heterogeneous dry reforming of methane, Chemical Engineering Science 122 (2015) 197–209.

[118] G. D. Wehinger, T. Eppinger, M. Kraume, Evaluating Catalytic Fixed-Bed Reactors for Dry Reforming of Methane with Detailed CFD, Chemie Ingenieur Technik 87 (6) (2015) 734–745.

[119] M. Behnam, A. G. Dixon, P. M. Wright, M. Nijemeisland, E. H. Stitt, Comparison of CFD simulations to experiment under methane steam reforming reacting conditions, Chemical Engineering Journal 207-208 (2012) 690–700.

[120] A. G. Dixon, M. E. Taskin, M. Nijemeisland, E. H. Stitt, CFD Method To Couple Three-Dimensional Transport and Reaction inside Catalyst Particles to the Fixed Bed Flow Field, Industrial & Engineering Chemistry Research 49 (19) (2010) 9012–9025.

[121] B. Partopour, A. G. Dixon, Computationally efficient incorporation of microkinetics into resolved-particle CFD simulations of fixed-bed reactors, Computers & Chemical Engineering 88 (2016) 126–134.

[122] M. Salciccioli, M. Stamatakis, S. Caratzoulas, D. Vlachos, A review of multiscale modeling of metal-catalyzed reactions: Mechanism development for complexity and emergent behavior, Chemical Engineering Science 66 (19) (2011) 4319–4355.

[123] M. P. Dudukovic, F. Larachi, P. L. Mills, Multiphase reactors revisited, Chemical Engineering Science 54 (13-14) (1999) 1975–1995.

[124] H. A. Jakobsen, Chemical Reactor Modeling, Springer International Publishing, Cham, 2014.

[125] M. Johnson, Pore structure and gaseous diffusion in solid catalysts, Journal of Catalysis 4 (2) (1965) 248–252.

[126] J. Szekely, J. Evans, A structural model for gas-solid reactions with a moving boundary-II, Chemical Engineering Science 26 (11) (1971) 1901–1913.

[127] C. Rieckmann, F. J. Keil, Simulation and experiment of multicomponent diffusion and reaction in three-dimensional networks, Chemical Engineering Science 54 (15-16) (1999) 3485–3493.

[128] J. Solsvik, H. A. Jakobsen, Multicomponent mass diffusion in porous pellets: Effects of flux models on the pellet level and impacts on the reactor level. Application to methanol synthesis, The Canadian Journal of Chemical Engineering 91 (1) (2013) 66–76.

[129] J. Solsvik, H. A. Jakobsen, Impacts on the Reactor Performance of Intra-Particle Multicomponent Mass Diffusion Limitations: Knudsen Diffusion, Energy Procedia 26 (2012) 116–124.

[130] L. L. Hegedus, Catalyst Pore Structures by Constrained Nonlinear Optimization, Industrial & Engineering Chemistry Product Research and Development 19 (4) (1980) 533–537.

[131] N. Wakao, J. M. Smith, Diffusion and Reaction in Porous Catalysts, Industrial & Engineering Chemistry Fundamentals 3 (2) (1964) 123–127.

[132] J. Solsvik, H. A. Jakobsen, A Survey of Multicomponent Mass Diffusion Flux Closures for Porous Pellets: Mass and Molar Forms, Transport in Porous Media 93 (1) (2012) 99–126.

[133] D. Schlereth, O. Hinrichsen, A fixed-bed reactor modeling study on the methanation of CO2, Chemical Engineering Research and Design 92 (4) (2014) 702–712.

[134] M. Giese, K. Rottschäfer, D. Vortmeyer, Measured and modeled superficial flow profiles in packed beds with liquid flow, AIChE Journal 44 (2) (1998) 484–490.

[135] O. Bey, G. Eigenberger, Gas flow and heat transfer through catalyst filled tubes, International Journal of Thermal Sciences 40 (2) (2001) 152–164.

[136] P. Marín, F. V. Díez, S. Ordóñez, Fixed bed membrane reactors for WGSR-based hydrogen production: Optimisation of modelling approaches and reactor performance, International Journal of Hydrogen Energy 37 (6) (2012) 4997–5010.

[137] M. L. Hunt, C. L. Tien, Non-Darcian Convection in Cylindrical Packed Beds, Journal of Heat Transfer 110 (2) (1988) 378.

[138] Y. A. Zou R.P., Wall effect on the packing of cylindrical particles, Chemical Engineering Science 51 (7) (1996) 1177–1180.

[139] A. G. Dixon, A. K. Gurnon, M. Nijemeisland, E. H. Stitt, CFD testing of the pointwise use of the ZehnerSchlünder formulas for fixed-bed stagnant thermal conductivity, International Communications in Heat and Mass Transfer 42 (2013) 1–4.

[140] STAR-CCM+ User guide, CD-adapco (2017).

[141] G. D. Wehinger, M. Kraume, V. Berg, O. Korup, K. Mette, R. Schlögl, M. Behrens, R. Horn, Investigating dry reforming of methane with spatial reactor profiles and particle-resolved CFD simulations, AIChE Journal 62 (12) (2016) 4436–4452.

[142] M. Sakai, M. Abe, Y. Shigeto, S. Mizutani, H. Takahashi, A. Viré, J. R. Percival, J. Xiang, C. C. Pain, Verification and validation of a coarse grain model of the DEM in a bubbling fluidized bed, Chemical Engineering Journal 244 (2014) 33–43.

[143] A. Di Renzo, F. P. Di Maio, Comparison of contact-force models for the simulation of collisions in DEM-based granular flow codes, Chemical Engineering Science 59 (3) (2004) 525–541.

[144] K. L. Johnson, Contact mechanics, 9th Edition, Cambridge Univ. Press, Cambridge, 2003.

[145] J. H. Ferziger, M. Perić, Computational methods for fluid dynamics, 2nd Edition, Springer, Berlin ; New York, 1999.

[146] O. Deutschmann, Modeling of the Interactions Between Catalytic Surfaces and Gas-Phase, Catalysis Letters 145 (1) (2015) 272–289.

[147] V. M. Janardhanan, O. Deutschmann, Computational Fluid Dynamics of Catalytic Reactors, in: O. Deutschmann (Ed.), Modeling and Simulation of Heterogeneous Catalytic Reactions, Wiley-VCH Verlag GmbH & Co. KGaA, Weinheim, Germany, 2011, pp. 251–282.

[148] R. Quiceno, J. Pérez-Ramrez, J. Warnatz, O. Deutschmann, Modeling the high-temperature catalytic partial oxidation of methane over platinum gauze: Detailed gas-phase and surface chemistries coupled with 3d flow field simulations, Applied Catalysis A: General 303 (2) (2006) 166–176.

[149] B. E. Poling, The properties of gases and liquids, 5th Edition, McGraw-Hill, New York, 2001.

[150] O. Deutschmann, Computational Fluid Dynamics Simulation of Catalytic Reactors, in: Handbook of Heterogeneous Catalysis, Wiley-VCH Verlag GmbH & Co. KGaA, Weinheim, Germany, 2008, pp. 1811–1828.

[151] I. Chorkendorff, J. W. Niemantsverdriet, Concepts of modern catalysis and kinetics, Wiley-VCH, Weinheim [Germany], 2003, oCLC: ocm51862977.

[152] R. Prins, A. Wang, X. Li, Introduction to heterogeneous catalysis, no. volume 1 in Advanced textbooks in chemistry, World Scientific, Imperial College Press, Hackensack, NJ, 2016.

[153] C. T. Campbell, Future Directions and Industrial Perspectives Micro- and macro-kinetics: Their relationship in heterogeneous catalysis, Topics in Catalysis 1 (3-4) (1994) 353–366.

[154] J. A. Dumesic, The microkinetics of heterogeneous catalysis, An American Chemical Society Publication, 1993.

[155] M. Neurock, The microkinetics of heterogeneous catalysis. By J. A. Dumesic, D. F. Rudd, L. M. Aparicio, J. E. Rekoske, and A. A. Treviño, ACS Professional Reference Book, American Chemical Society, Washington, DC, 1993, 315 pp., AIChE Journal 40 (6) (1994) 1085–1087.

[156] A. A. Gokhale, S. Kandoi, J. P. Greeley, M. Mavrikakis, J. A. Dumesic, Molecular-level descriptions of surface chemistry in kinetic models using density functional theory, Chemical Engineering Science 59 (22-23) (2004) 4679–4691.

[157] C. F. Goldsmith, R. H. West, Automatic Generation of Microkinetic Mechanisms for Heterogeneous Catalysis, The Journal of Physical Chemistry C 121 (18) (2017) 9970–9981.

[158] P. Stoltze, Microkinetic simulation of catalytic reactions, Progress in Surface Science 65 (3-4) (2000) 65–150.

[159] K. Reuter, Ab Initio Thermodynamics and First-Principles Microkinetics for Surface Catalysis, Catalysis Letters 146 (3) (2016) 541–563.

[160] H. K. Versteeg, W. Malalasekera, An introduction to computational fluid dynamics: the finite volume method, nachdr. Edition, Pearson/Prentice Hall, Harlow, 2005, oCLC: 255001925.

[161] P. A. Davidson, Turbulence: an introduction for scientists and engineers, Oxford University Press, Oxford, UK ; New York, 2004.

[162] D. Seguin, A. Montillet, J. Comiti, Experimental characterisation of flow regimes in various porous mediaI: Limit of laminar flow regime, Chemical Engineering Science 53 (21) (1998) 3751–3761.

[163] B. Launder, D. Spalding, The numerical computation of turbulent flows, Computer Methods in Applied Mechanics and Engineering 3 (2) (1974) 269–289.

[164] T. L. Chambers, D. C. Wilcox, Critical examination of two-equation turbulence closure models for boundary layers, AIAA J 15 (6) (1977) 821–828.

[165] D. C. Wilcox, Formulation of the k-w Turbulence Model Revisited, AIAA Journal 46 (11) (2008) 2823–2838.

[166] W. Jones, B. Launder, The prediction of laminarization with a two-equation model of turbulence, International journal of heat and mass transfer 15 (2) (1972) 301–314.

[167] T.-H. Shih, W. W. Liou, A. Shabbir, Z. Yang, J. Zhu, A new k- eddy viscosity model for high reynolds number turbulent flows, Computers & Fluids 24 (3) (1995) 227–238.

[168] Wiley-VCH Verlag GmbH & Co. KGaA (Ed.), Ullmann's Encyclopedia of Industrial Chemistry, Wiley-VCH Verlag GmbH & Co. KGaA, Weinheim, Germany, 2000.

[169] V. Sadykov, L. Isupova, I. Zolotarskii, L. Bobrova, A. Noskov, V. Parmon, E. Brushtein, T. Telyatnikova, V. Chernyshev, V. Lunin, Oxide catalysts for ammonia oxidation in nitric acid production: properties and perspectives, Applied Catalysis A: General 204 (1) (2000) 59–87.

[170] C. H. Bartholomew, R. J. Farrauto, Fundamentals of Industrial Catalytic Processes: Bartholomew/Fundamentals, John Wiley & Sons, Inc., Hoboken, NJ, USA, 2005.

[171] A. Jess, U. Kragl, P. Wasserscheid, Chemical technology: an integral textbook, Wiley-VCH, Weinheim, 2009.

[172] H. Schwarz, Y. Dong, R. Horn, Catalytic Methane Combustion on a Pt Gauze: Laser-Induced Fluorescence Spectroscopy, Species Profiles, and Simulations, Chemical Engineering & Technology 39 (11) (2016) 2011–2019.

[173] C. de Smet, M. de Croon, R. Berger, G. Marin, J. Schouten, An experimental reactor to study the intrinsic kinetics of catalytic partial oxidation of methane in the presence of heat-transport limitations, Applied Catalysis A: General 187 (1) (1999) 33–48.

[174] G. P. Smith, D. M. Golden, M. Frenklach, N. W. Moriarty, B. Eiteneer, M. Goldenberg, C. T. Bowman, R. K. Hanson, S. Song, W. C. Gardiner Jr, et al., Gri-mech 3.0 (1999).

[175] O. Deutschmann, R. Schmidt, F. Behrendt, J. Warnat, Numerical modeling of catalytic ignition, Symposium (International) on Combustion 26 (1) (1996) 1747–1754.

[176] Z. Ren, S. B. Pope, Second-order splitting schemes for a class of reactive systems, Journal of Computational Physics 227 (17) (2008) 8165–8176.

[177] H. Schwarz, M. Geske, C. Franklin Goldsmith, R. Schlögl, R. Horn, Fuel-rich methane oxidation in a high-pressure flow reactor studied by optical-fiber laser-induced fluorescence, multi-species sampling profile measurements and detailed kinetic simulations, Combustion and Flame 161 (7) (2014) 1688–1700.

[178] L. Giani, G. Groppi, E. Tronconi, Heat Transfer Characterization of Metallic Foams, Industrial & Engineering Chemistry Research 44 (24) (2005) 9078–9085.

[179] L. Giani, G. Groppi, E. Tronconi, Mass-Transfer Characterization of Metallic Foams as Supports for Structured Catalysts, Industrial & Engineering Chemistry Research 44 (14) (2005) 4993–5002.

[180] G. Incera Garrido, F. Patcas, S. Lang, B. Kraushaar-Czarnetzki, Mass transfer and pressure drop in ceramic foams: A description for different pore sizes and porosities, Chemical Engineering Science 63 (21) (2008) 5202–5217.

[181] E. Bianchi, W. Schwieger, H. Freund, Assessment of Periodic Open Cellular Structures for Enhanced Heat Conduction in Catalytic Fixed-Bed Reactors: Heat Conduction in Periodic Open Cellular Structures, Advanced Engineering Materials 18 (4) (2016) 608–614.

[182] W. Peng, M. Xu, X. Li, X. Huai, Z. Liu, H. Wang, CFD study on thermal transport in open-cell metal foams with and without a washcoat: Effective thermal conductivity and gas-solid interfacial heat transfer, Chemical Engineering Science 161 (2017) 92–108.

[183] S. T. Kolaczkowski, S. Awdry, T. Smith, D. Thomas, L. Torkuhl, R. Kolvenbach, Potential for metal foams to act as structured catalyst supports in fixed-bed reactors, Catalysis Today 273 (2016) 221–233.

[184] A. Della Torre, G. Montenegro, G. Tabor, M. Wears, CFD characterization of flow regimes inside open cell foam substrates, International Journal of Heat and Fluid Flow 50 (2014) 72–82.

[185] P. Ranut, E. Nobile, L. Mancini, High resolution X-ray microtomography-based CFD simulation for the characterization of flow permeability and effective thermal conductivity of aluminum metal foams, Experimental Thermal and Fluid Science 67 (2015) 30–36.

[186] E. Bianchi, T. Heidig, C. G. Visconti, G. Groppi, H. Freund, E. Tronconi, Heat transfer properties of metal foam supports for structured catalysts: Wall heat transfer coefficient, Catalysis Today 216 (2013) 121–134.

[187] S. Razza, T. Heidig, E. Bianchi, G. Groppi, W. Schwieger, E. Tronconi, H. Freund, Heat transfer performance of structured catalytic reactors packed with metal foam supports: Influence of wall coupling, Catalysis Today 273 (2016) 187–195.

[188] P. Ranut, On the effective thermal conductivity of aluminum metal foams: Review and improvement of the available empirical and analytical models, Applied Thermal Engineering 101 (2016) 496–524.

[189] A. Inayat, M. Klumpp, M. Lämmermann, H. Freund, W. Schwieger, Development of a new pressure drop correlation for open-cell foams based completely on theoretical grounds: Taking into account strut shape and geometric tortuosity, Chemical Engineering Journal 287 (2016) 704–719.

[190] G. Groppi, L. Giani, E. Tronconi, Generalized Correlation for Gas/Solid Mass-Transfer Coefficients in Metallic and Ceramic Foams, Industrial & Engineering Chemistry Research 46 (12) (2007) 3955–3958.

[191] P. Habisreuther, N. Djordjevic, N. Zarzalis, Statistical distribution of residence time and tortuosity of flow through open-cell foams, Chemical Engineering Science 64 (23) (2009) 4943–4954.

[192] P. Parthasarathy, P. Habisreuther, N. Zarzalis, Evaluation of longitudinal dispersion coefficient in open-cell foams using transient direct pore level simulation, Chemical Engineering Science 90 (2013) 242–249.

[193] G. D. Wehinger, H. Heitmann, M. Kraume, An artificial structure modeler for 3d CFD simulations of catalytic foams, Chemical Engineering Journal 284 (2016) 543–556.

[194] A. Della Torre, F. Lucci, G. Montenegro, A. Onorati, P. Dimopoulos Eggenschwiler, E. Tronconi, G. Groppi, CFD modeling of catalytic reactions in open-cell foam substrates, Computers & Chemical Engineering 92 (2016) 55–63.

[195] R. Horn, O. Korup, M. Geske, U. Zavyalova, I. Oprea, R. Schlögl, Reactor for in situ measurements of spatially resolved kinetic data in heterogeneous catalysis, Review of Scientific Instruments 81 (6) (2010) 064102.

[196] `http://www.panalytical.com/Empyrean.htm`, accessed: 2017.

[197] `http://imagej.net`, accessed: 2017.

[198] O. Korup, S. Mavlyankariev, M. Geske, C. F. Goldsmith, R. Horn, Measurement and analysis of spatial reactor profiles in high temperature catalysis research, Chemical Engineering and Processing: Process Intensification 50 (10) (2011) 998–1009.

[199] S. Kabelac, D. Vortmeyer, K1 Radiation of Surfaces, in: VDI e. V. (Ed.), VDI Heat Atlas, Springer Berlin Heidelberg, Berlin, Heidelberg, 2010, pp. 945–960.

[200] R. Siegel, J. R. Howell, Thermal radiation heat transfer, 2nd Edition, Series in thermal and fluids engineering, Hemisphere Pub. Corp, Washington, 1981.

[201] `http://www.detchem.com`, accessed: 2016.

[202] O. Deutschmann, L. Maier, U. Riedel, A. Stroemman, R. Dibble, Hydrogen assisted catalytic combustion of methane on platinum, Catalysis Today 59 (1-2) (2000) 141–150.

[203] H. Schwarz, M. Geske, C. F. Goldsmith, R. Schlögl, R. Horn, Fuel-rich methane oxidation in a high-pressure flow reactor studied by optical-fiber laser-induced fluorescence, multi-species sampling profile measurements and detailed kinetic simulations., Combust. Flame 161 (7) (2014) 1688–1700.

[204] M. A. Vannice, Kinetics of catalytic reactions, Springer, New York, 2005.

[205] G. E. Mueller, Numerically packing spheres in cylinders, Powder Technology 159 (2) (2005) 105–110.

[206] A. de Klerk, Voidage variation in packed beds at small column to particle diameter ratio, AIChE Journal 49 (8) (2003) 2022–2029.

[207] GNU Image Manipulation Program, http://gimp.org (2016).

[208] A. I. Anastasov, A study of the influence of the operating parameters on the temperature of the hot spot in a fixed bed reactor, Chemical Engineering Journal 86 (3) (2002) 287–297.

[209] A. de Wasch, G. Froment, Heat transfer in packed beds, Chemical Engineering Science 27 (3) (1972) 567–576.

[210] M. Freiwald, W. Paterson, Accuracy of model predictions and reliability of experimental data for heat transfer in packed beds, Chemical Engineering Science 47 (7) (1992) 1545–1560.

[211] R. Horn, N. J. Degenstein, K. A. Williams, L. D. Schmidt, Spatial and temporal profiles in millisecond partial oxidation processes, Catalysis Letters 110 (3-4) (2006) 169–178.

[212] O. Korup, R. Schlögl, R. Horn, Carbon formation in catalytic partial oxidation of methane on platinum: Model studies on a polycrystalline Pt foil, Catalysis Today 181 (1) (2012) 177–183.

[213] A. Sederman, M. Johns, P. Alexander, L. Gladden, Structure-flow correlations in packed beds, Chemical Engineering Science 53 (12) (1998) 2117–2128.

[214] M. Geske, O. Korup, R. Horn, Resolving kinetics and dynamics of a catalytic reaction inside a fixed bed reactor by combined kinetic and spectroscopic profiling, Catal. Sci. Technol. 3 (1) (2013) 169–175.

[215] M. Geske, K. Pelzer, R. Horn, F. Jentoft, R. Schlögl, In-situ investigation of gas phase radical chemistry in the catalytic partial oxidation of methane on Pt, Catalysis Today 142 (1-2) (2009) 61–69.

[216] J. Gascón, R. Valenciano, C. Téllez, J. Herguido, M. Menéndez, A generalized kinetic model for the partial oxidation of n-butane to maleic anhydride under aerobic and anaerobic conditions, Chemical Engineering Science 61 (19) (2006) 6385–6394.

[217] S. Böcklein, G. Mestl, S. V. Auras, J. Wintterlin, On the Correlation of Structure and Catalytic Performance of VPO Catalysts, Topics in Catalysis 60 (19-20) (2017) 1682–1697.

[218] C. Dobner, M. Duda, S. Storck, J. Weiguny, Catalyst and method for producing maleic anhydride, european Patent EP1487576A1, BASF SE, 2002.
URL `https://patents.google.com/patent/EP1487576A1/en`

[219] P. J. Linstrom, W. G. Mallard, NIST Chemistry WebBook; NIST Standard Reference Database No. 69, Gaithersburg MD, 2001.

[220] C. Schulz, Ph.D. thesis, Technische Universität Berlin (2018).

[221] C. Schulz, F. Pohl, F. Rosowski, B. Frank, to be submitted.

[222] W. M. Brandstädter, B. Kraushaar-Czarnetzki, Maleic Anhydride from Mixtures of n -Butenes and n -Butane: Simulation of a Production-Scale Nonisothermal Fixed-Bed Reactor, Industrial & Engineering Chemistry Research 46 (5) (2007) 1475–1484.

[223] J. B. Benziger, V. Guliants, S. Sundaresan, New precursors to vanadium phosphorus oxide catalysts, Catalysis Today 33 (1-3) (1997) 49–56.

[224] G. Centi, Some prospects and priorities for future research on vanadyl pyrophosphate, Catalysis Today 16 (1) (1993) 147–153.

[225] R. Glaum, C. Welker-Nieuwoudt, C.-K. Dobner, M. Eichelbaum, F. Gruchow, C. Heine, A. Karpov, R. Kniep, F. Rosowski, R. Schlögl, S. A. Schunk, S. Titlbach, A. Trunschke, Resource-Efficient Alkane Selective Oxidation on New Crystalline Solids: Searching for Novel Catalyst Materials, Chemie Ingenieur Technik 84 (10) (2012) 1766–1779.

[226] F. Keil, Diffusion and reaction in porous networks, Catalysis Today 53 (2) (1999) 245–258.

[227] J. Wei, Catalyst designs to enhance diffusivity and performanceI: Concepts and analysis, Chemical Engineering Science 66 (19) (2011) 4382–4388.

[228] M.-O. Coppens, J. Sun, T. Maschmeyer, Synthesis of hierarchical porous silicas with a controlled pore size distribution at various length scales, Catalysis Today 69 (1-4) (2001) 331–335.

[229] Y. Liu, J. Goebl, Y. Yin, Templated synthesis of nanostructured materials, Chem. Soc. Rev. 42 (7) (2013) 2610–2653.

[230] D. Luss, Reaction engineering of advanced ceramic materials, Chemical Engineering Science 45 (8) (1990) 1979–1999.

[231] M. A.-H. Ali, K. Al-Humaizi, Maleic anhydride production in a cross-flow reactor: A comparative study, The Canadian Journal of Chemical Engineering 92 (5) (2014) 876–883.

[232] J. Diedenhoven, A. Reitzmann, G. Mestl, T. Turek, A model for the phosphorus dynamics of VPO catalysts during the selective oxidation of n -butane to maleic anhydride in a tubular reactor, Chemie Ingenieur Technik 84 (4) (2012) 517–523.

[233] R. Guettel, T. Turek, Assessment of micro-structured fixed-bed reactors for highly exothermic gas-phase reactions, Chemical Engineering Science 65 (5) (2010) 1644–1654.

[234] M. Alonso, M. Lorences, M. Pina, G. Patience, Butane partial oxidation in an externally fluidized bed-membrane reactor, Catalysis Today 67 (1-3) (2001) 151–157.

[235] B. M. Cruz, J. D. da Silva, A two-dimensional mathematical model for the catalytic steam reforming of methane in both conventional fixed-bed and fixed-bed membrane reactors for the Production of hydrogen, International Journal of Hydrogen Energy 42 (37) (2017) 23670–23690.

[236] COMSOL Multiphysics Reference Manual, version 5.0, www.comsol.com (2016).

[237] T. Wellauer, D. Cresswell, E. Newson, Optimal policies in maleic anhydride production through detailed reactor modelling, Chemical Engineering Science 41 (4) (1986) 765–772.

[238] M. A. Carreon, V. V. Guliants, Macroporous Vanadium Phosphorus Oxide Phases Displaying Three-Dimensional Arrays of Spherical Voids, Chemistry of Materials 14 (6) (2002) 2670–2675.

[239] M. A. Carreon, V. V. Guliants, Synthesis of catalytic materials on multiple length scales: from mesoporous to macroporous bulk mixed metal oxides for selective oxidation of hydrocarbons, Catalysis Today 99 (1-2) (2005) 137–142.

Nomenclature

Abbreviations

μ-CT	computed microtomography
BHS	back heat shield
CFD	computational fluid dynamics
D/d	ratio of reactor diameter D to pellet diameter d
DEM	discrete element method
DNS	direct numerical simulation
FHS	front heat shield
LIF	laser-induced fluorescence
MA	maleic anhydride
MRI	magnetic resonance imaging
PPI	pore per inch
RANS	Reynolds-averaged Navier-Stokes
VPP	vanadyl pyrophosphate

Greek letters

$\bar{\phi}'$	fluctuating value of variable [various]
$\bar{\phi}$	mean value of variable [various]
β	temperature exponent [-]
δv	diffusion volume [-]
δ_{ij}	Kronecker delta [-]
δ_{max}	maximum overlap [m]
η	effectiveness factor [-]
Γ	surface site density [mol/m^2]
κ	bulk viscosity [Pa·s]
λ	thermal conductivity [W/(m·K)]
λ_{bed}	effective stagnant bed thermal conductivity [W/(m·K)]
μ	dynamic viscosity [Pa·s]
μ_t	turbulent energy [J]
$\nu\prime_{jk}$	stoichiometric coefficient of species j in reaction k when it is reactant [-]
ν_{ik}	stoichiometric coefficient of species i in reaction k [-]
$\Omega(T^*)$	collision integral
ρ	density [kg/m^3]
σ	Lennard-Jones characteristic length [Å]
σ	coordinate number [-]
σ_k	turbulence Prandtl number [-]
τ	sum of all stoichiometric coefficient of the surface reactants [-]
τ	tortuosity [-]
τ_{ij}	stress tensor [N]
θ	surface coverage [-]
ε	Lennard-Jones energy [J]
ε	turbulent energy dissipation rate [J/(kg·s)]
ε	void fraction [-]
ε_0	infinite bed porosity [-]
ε_M	macro-pore porosity [-]
ε_m	micro-pore porosity [-]
ε_{bed}	bed porosity [-]
ε_{total}	total pore porosity [-]
ζ	dimensionless radial cylindrical coordinate of the pellet [-]

Latin letters

$\Delta H^{\circ}_{R,298K}$	reaction enthalpy at standard condition [J/mol]
$\dot{s}_i$	molar net production rate of species i [mol/m$^2\cdot$ s]
$\mathbf{u}$	velocity field [m/s]
ν	Poisson's ratios [-]
$\vec{F}$	force [N]
A	pre-exponential factor (variable]
a_v	specific surface area [1/m]
A_{cat}/A_{geo}	ratio of catalytically active area to geometric area [-]
C_E	Ergun parameter [-]
c_i	species concentration [mol/m^3 or mol/m^2]
c_p	specific heat capacity [J/(kg·K)]

C_μ,C_1,C_2,σ_ε empirical coefficient in the standard $k-\varepsilon$ model [-]
C_{fs} static friction coefficient [-]
C_{rest} coefficient of restitution [-]
D reactor diameter ([m]
d diameter of the cylinder [m]
d overlap [m]
d particle diameter [m]
d_M macro-pore diameter [m]
d_m micro-pore diameter [m]
D_r radial dispersion coefficient [m^2/s]
D_{AB} binary diffusivity [m^2/s]
D_{ax} axial dispersion coefficient [m^2/s]
D_{eff} effective diffusivity [m^2/s]
$D_{i,j}$ binary diffusion coefficient [m^2/s]
$D_{i,m}$ diffusion coefficient of species i in the mixture [m^2/s]
D_K Knudsen diffusivity [m^2/s]
$D_{M,m}$ diffusivity in macro and micro pores [m^2/s]
E Young's modulus [N/m^2]
E_a activation energy [J/mol]
G shear modulus [N·s/m]
h height of the cylindrical pellet [m]
h specific enthalpy [J/kg]
j_i diffusion mass flux [kg/(m^2· s)]
K kinetic parameter [1/Pa]
K spring stiffness [N/m]
k reaction rate constant (variable]
k turbulent kinetic energy [J]
K_1 slope parameter [-]
K_2 damping parameter [-]
k_B Boltzmann constant [m^2kg/(s^2· K)]
K_D darcy hydraulic permeability [m^2]
K_E Ergun hydraulic permeability [m^2]
K_s number of elementary surface reactions [-]
l_R Reactor length [m]
M_i molar mass of species i [kg/mol]
M_A,M_B mass of sphere A and B [kg]
N damping [N·s/m]
n exponent of damping function [-]
N_g number of gas phase species [-]
N_i molar flux [mol/(m^2·s)]
N_s number of adsorbed species [-]
N_{damp} damping coefficient [-]
p pressure [Pa]
Pe_h Péclet numbe for heat transfer $ud_pCp_f\rho_f/\lambda_f$ [-]
Pe_m molecular Péclet number ud_p/D_{AB} [-]
q'_{rad} radiant flux [W/m^2]
R ideal gas constant [J/(K·mol)]
R radius [m]
R reactor radius [m]
R_i^{het} heterogeneous surface reaction rate [kg/(m^2·s)]
R_i^{hom} homogeneous reactions rate [kg/(m^3·s)]
r_j reaction rate [mol/(kg_{cat}·s)]
r_s reaction rate [mol/(m^2·s)]
Re Reynolds number $\rho_f u d_p/\mu$ [-]
S_g specific area per catalyst mass [m^2/kg]
s_h heat source [W/m^3]
S_i initial sticking coefficient [-]
T absolute temperature [K]
T^* reduced temperature [-]
u superficial velocity [m/s]
v velocity components of the relative sphere surface velocity at the contact point [m/s]
V_M macro-pore volume [m^3/kg]
V_m micro-pore volume [m^3/kg]
X_i molar fraction of species i [-]
x_i Cartesian coordinate [m]
Y_i mass fraction of species i [-]
y_i molar fraction [-]

Subscript

ax axial direction, cylindrical coordinate
$bulk$ bulk gas phase
eff effective
eq equivalent
f fluid
i gas species
M macro-pore
m micro-pore
n normal component
p particle
r radial direction, cylindrical coordinate
t tangential component

List of Figures

List of Tables